

Total Pressure Loss Mechanism in a Diesel Engine Turbocharger

A Thesis Submitted for the Degree of Doctor of Philosophy

By

Xiaoyang Gong

Department of Aeronautical and Automotive Engineering

Loughborough University

Loughborough

UK

November 2016

Abstract

Simulation tools are intensively used in the design stage of diesel engines due to their contributions to significant savings in cost and time for the engine development. Since most of DI diesel engines are turbocharged, it is of vital importance to hold a good understanding of turbine and compressor characteristic to predict the engine performance accurately. However, this data is often not available from turbocharger manufacturers, particularly for turbines. On available turbine maps the operating range of the turbine is constrained due to limitations of conventional turbocharger test benches. Operations with a wider range of turbocharger pressure ratios can be achieved by employing complex turbocharger test benches, which will also lead to higher costs including hardware and labour.

An alternative solution is to develop numerical models for the turbocharger based on thermodynamics. In this thesis numerical models has been developed for predicting the performance of both the centrifugal compressors and turbines and they have been also validated using test cases, particularly for variable geometry turbines.

Following detailed parametric studies, the turbocharger model has been validated against experimental data of a turbocharger with a variable geometry turbine. Results showed that the model was capable of predicting the characteristics maps of the turbocharger accurately, requiring a minimal amount of turbocharger geometric properties, experimental data and calibration parameters. Thus, by combining with the engine performance simulation software there is a highly potential for the numerical model developed in this work to become a useful tool for predicting engine performance and turbo matching calculations or diagnostic applications.

Acknowledgements

Many people have supported this thesis rather than the cover suggests. I would like to thank several special people for their support of my PhD study and the writing of this thesis.

Firstly, to my supervisor Professor Rui Chen for his invaluable guidance, encouragement throughout this study. This thesis would be impossible without his invaluable supervision.

Thanks also should be given to Loughborough University who provides the world-class research environment and to the colleges working together.

Special thanks to my beloved wife, Miaomiao Hu, for her never-ending love, patience, and encouragement. Without these, I would not be where I am today.

Last but not the least, lots of thanks to my parents for their financial and emotional support during these years. I can never fully express my gratitude using words. This thesis could be the best gift to them.

List of Publications

1. X. Gong and R. Chen, "Turbocharger performance simulation with optimized 1D model," *Advanced Materials Research*, vol. 516-517, pp. 692-708, 2012
2. X. Gong and R. Chen, "Total pressure loss mechanism of centrifugal compressors," *Journal of Mechanical Engineering Research*, vol. 4, pp. 45 - 59, 2014

Table of Content

Abstract.....	ii
Acknowledgements.....	iii
List of Publications	iv
List of Figures	xi
List of Tables	xv
Abbreviations.....	xvi
Nomenclature.....	xviii
Chapter 1 Introduction	22
1.1 Turbocharging	22
1.2 Background	24
1.3 Aim and Objectives.....	26
1.4 Thesis Organisation.....	26
Chapter 2 Literature Review.....	29
2.1 Current Turbocharger Technologies	29
2.1.1 Positive Displacement Compressors and Other Superchargers	31
2.1.2 Waste-gated Turbocharger	33
2.1.3 Variable Geometry/Nozzle Turbocharger (VGT/VNT).....	34
2.1.4 Multi-stage Turbochargers	36
2.1.5 Electric Turbochargers	38
2.1.6 Twin Entry Turbines.....	40
2.1.7 Variable Flow Turbocharger (VFT)	41
2.2 Methodologies for Turbocharger Total Performance Optimization	42
2.2.1 Experimental Investigation.....	42
2.2.2 Modelling of Total Turbocharger Performance	45

2.2.3 Computational Fluid Dynamics (CFD)	46
2.2.4 Turbocharger Control Modelling	48
2.2.5 One Dimensional (1D) Simulation	49
2.3 Compressor Loss Models	50
2.3.1 Introduction	50
2.3.2 Inlet Suction Losses.....	51
2.3.3 Incidence Losses.....	51
2.3.4 Frictional Losses.....	53
2.3.5 Volute Loss.....	54
2.3.6 Clearance Loss.....	55
2.3.7 Backflow Loss	55
2.3.8 Heat Transfer Losses	55
2.3.9 Inter-stage Losses	56
2.4 Turbine Models	57
2.4.1 Volute Losses	57
2.4.2 Turbine Incidence Losses	58
2.4.3 Variable Geometry Turbine Model	58
2.5 Summary	58
Chapter 3 The Compressor Model.....	60
3.1 Basic Theories for Compressor Model Construction.....	60
3.1.1 The Inlet Casing	60
3.1.2 The Impeller	61
3.1.3 The Vaneless Diffuser	62
3.1.4 The Vaned Diffuser	63
3.1.5 The Volute	64
3.2 Compressor Model Structure	64

3.2.1 Mathematic Description for the Centrifugal Compressor	64
3.2.2 Flow Chart for the Centrifugal Compressor Performance Prediction	65
3.3 Centrifugal Compressor Model.....	67
3.3.1 The Impeller Inlet.....	67
3.3.2 The Impeller Throat.....	69
3.3.3 The Impeller Exit.....	71
3.3.4 Losses in the Impeller.....	72
3.3.4.1 Calculation of Incidence Loss.....	74
3.3.4.2 Calculation of Clearance Loss	74
3.3.4.3 Calculation of Entrance Diffusion Loss.....	74
3.3.4.4 Calculation of Skin Friction Loss	75
3.3.4.5 Calculation of Choking Loss	76
3.3.4.6 Calculation of Blade Loading Loss	76
3.3.4.7 Calculation of Hub to Shroud Loading Loss	77
3.3.4.8 Calculation of Blockage Loss	78
3.3.4.9 Calculation of Mixing Loss	79
3.3.5 The Vaneless Diffuser	80
3.3.6 Losses in Vaneless Diffuser	81
3.3.6.1 Calculation of Skin Friction Loss	81
3.3.6.2 Calculation of Diffusion Loss.....	81
3.3.7 Calculation of Vaned Diffuser.....	82
3.3.8 Losses in Vaned Diffuser	84
3.3.8.1 Calculation of Skin Friction Loss	84
3.3.8.2 Calculation of Incidence Loss.....	84
3.3.8.3 Calculation of Choking Loss	84
3.3.8.4 Calculation of Mixing Loss	85

3.3.9 The Volute	86
3.3.10 Losses in the Volute	87
3.3.10.1 Calculation of Skin Friction Loss	87
3.3.10.2 Calculation of Kinetic Energy Loss	87
3.3.10.3 Calculation of Skin Friction Loss	87
3.4 Calculation of Centrifugal Compressor Performance Map	88
3.4.1 Calculation of Centrifugal Compressor Pressure Ratio	88
3.4.2 Calculation of Centrifugal Compressor Isentropic Efficiency	88
3.5 Summary	89
Chapter 4 Compressor Model Validation	91
4.1 Model Validation with Experimental Work	91
4.1.1 Experimental Test Rig	91
4.1.2 Validation Results and Discussion	91
4.2 Effect of Loss Mechanism on Compressor Performance	95
4.3 Pressure Build-up in Each Compressor Component	96
4.4 Individual Loss Investigation	97
4.4.1 Effects of Mass Flow Rate and Rotational Speed on Individual Loss	97
4.4.2 Correlations between Individual Loss and Flow Velocity and Its Angle	104
4.4.3 Effect of Geometry Change on Individual Loss	106
4.5 Flow Analysis in the Centrifugal compressor	109
4.5.1 Effects of Mass Flow Rate and Rotational Speed on Velocity Triangles	110
4.5.2 Dependency of Flow Angles on Mass Flow Rate and Rotational Speed	111
4.6 Summary	112
Chapter 5. Turbocharger Losses Model and Validation	114
5.1 Introduction	114
5.2 Turbine Model	114

5.2.1 Basic Theories for Turbine Model	115
5.2.2 The Volute Model.....	116
5.2.3 Losses in Volute	117
5.2.3.1 Calculation of Circumferential Distortion Losses	117
5.2.3.2 Calculation of Skin Friction Loss	118
5.2.4 The Nozzles Model.....	118
5.2.5 The Variable Nozzle Turbocharger (VNT) Model.....	120
5.2.6 The Rotor Model	121
5.2.7 The Exhaust Diffuser Model	122
5.3 Calculation of Radial Turbine Power Output.....	123
5.4 Calculation of Radial Turbine Isentropic Efficiency	123
5.5 Validation of Turbocharger Model	124
5.5.1 Validation of Turbine Expansion Ratio at Different VNT Opening	125
5.5.2 Validation of Turbine Isentropic Efficiency.....	128
5.6 Summary	130
Chapter 6 Optimisation of the Performance of Variable Nozzle Turbochargers (VNT).....	132
6.1 Introduction	132
6.2 The Effects of VNT on Turbine Performance.....	132
6.3 The Effects of VNT on Turbine Isentropic Efficiency	133
6.4 Investigation of Losses in Turbine under Different VNT Opening	134
6.4.1 Rotor Skin Friction Loss	134
6.4.2 Mixing Loss.....	135
6.4.3 Impeller Blade Loading Loss	136
6.4.4 Nozzle Skin Friction Loss	137
6.4.4 Rotor Incidence Loss.....	138
6.5 Investigation of Rotor Inlet Velocity under Different VNT Opening.....	139

6.6 Investigation of Flow Angle at Rotor Inlet under different VNT opening	141
6.7 Summary	141
Chapter 7 Implementation of Developed Turbocharger Model Coupled with AVL-BOOST Engine Model.....	143
7.1 AVL-BOOST Engine Model	143
7.1.1 Model Description	143
7.1.2 Model Validation.....	148
7.2 Simulation Results	149
7.2.1 Cyclic Simulation at 3000rpm.....	149
7.2.2 Steady-State Simulation Results.....	152
7.3 Summary	154
Chapter 8 Conclusions and Recommendations for Future Work	155
8.1 Conclusions	155
8.2 Future work	156
References.....	158

List of Figures

Figure 1.1 Turbocharger works with engine	3
Figure 1.2 Organization of the thesis	7
Figure 2.1 Statistical mean compressor pressure ratio of ABB turbochargers over the last 45 years.....	8
Figure 2.2 Two-screw supercharger	9
Figure 2.3 Waste-gate Turbocharger	10
Figure 2.4 Variable Geometry Turbocharger (VGT)	11
Figure 2.5 Improvement of low speed torque by VGT	12
Figure 2.6 A two-stage turbocharger	14
Figure 2.7 A multi-stage turbocharger and an e-turbo	15
Figure 2.8 An electrically assisted turbocharger	17
Figure 2.9 Cross section of the twin-entry radial inflow turbine	18
Figure 2.10 A Variable Flow Turbocharger (VFT).....	19
Figure 2.11 A steady flow turbocharger test rig.....	20
Figure 2.12 Unsteady turbocharger test rig	22
Figure 2.13 (a) Pulse generator system with VVA cylinder head, (b) Pulse generator system with rotating valves	24
Figure 2.14 Computational grid of the Mixed Flow Turbine	29
Figure 3.1 A typical centrifugal compressor	60
Figure 3.2 Velocity triangle at inducer. (Section through inducer at radius r_1)	61
Figure 3.3 Velocity triangle at impeller tip. (Section through impeller tip at radius r_2)	62
Figure 3.4 Flow inside the Vaneless diffuser	63
Figure 3.5 Compressor Component Division.....	64
Figure 3.6 Variables used to describe each compressor component	65

Figure 3.7 Flow Chart for the Compressor Performance Prediction.....	67
Figure 4.1 Validation of compressor pressure ratio with experimental data.....	93
Figure 4.2 Validation of compressor efficiency with experimental data	94
Figure 4.3 Effects of different losses on compressor performance (N=170K rpm).....	98
Figure 4.4 The pressure build up in each compressor component (N=170K rpm)	99
Figure 4.5 Dependency of impeller incidence loss on mass flow rate	98
Figure 4.6 Dependency of impeller blade loading loss on mass flow rate.....	99
Figure 4.7 Dependency of impeller skin friction loss on mass flow rate	103
Figure 4.8 Dependency of impeller clearance loss on mass flow rate	104
Figure 4.9 Dependency of impeller mixing loss on mass flow rate	105
Figure 4.10 Dependency of vaned diffuser skin friction loss on the velocity	106
Figure 4.11 Dependency of impeller incidence loss on inlet flow angle	107
Figure 4.12 Dependency of impeller skin friction loss on the velocity.....	108
Figure 4.13 Dependency of impeller skin friction loss on exit diameter	109
Figure 4.14 Dependency of impeller clearance loss on clearance gap.....	110
Figure 4.15 Dependency of impeller incidence loss on blade angle	111
Figure 4.16 Dependency of impeller exit velocity on mass flow rate.....	111
Figure 4.17 Dependency of impeller flow angle on mass flow rate.....	111
Figure 5.1 Radial turbine structure	115
Figure 5.2 Radial Turbine Component Division	116
Figure 5.3 Schematic representation of a volute	117
Figure 5.4 Schematic representation of the nozzles	119
Figure 5.5 Nozzle exit velocity triangles.....	119
Figure 5.6 Variable nozzle turbine (VNT)	119
Figure 5.7 Schematic representation of turbine rotor	122
Figure 5.8 Schematic representation of exhaust diffuser	122

Figure 5.9 Validation of turbine expansion ratio with experimental data (20% opening)	126
Figure 5.10 Validation of turbine expansion ratio with experimental data (50% opening)	127
Figure 5.11 Validation of turbine expansion ratio with experimental data (80% opening)	127
Figure 5.12 Validation of turbine isentropic efficiency with experimental data (20% opening)	128
Figure 5.13 Validation of turbine isentropic efficiency with experimental data (50% opening)	129
Figure 5.14 Validation of turbine isentropic efficiency with experimental data (80% opening)	130
Figure 6.1 The dependency of Nozzle incidence loss on the mass flow rate	133
Figure 6.2 The dependency of Nozzle skin friction loss on the mass flow rate	134
Figure 6.3 Rotor Skin Friction Loss at Different VNT Opening	135
Figure 6.4 Rotor Mixing Loss at Different VNT Opening	136
Figure 6.5 Rotor Blade Loading Loss at Different VNT Opening	137
Figure 6.6 Nozzle Skin Friction Loss at Different VNT Opening	138
Figure 6.7 Rotor Incidence Loss at Different VNT Opening	139
Figure 6.8 Rotor Inlet Velocity at different VNT openings.	140
Figure 6.9 Rotor Inlet Flow Angle at different VNT openings	141
Figure 7.1 AVL-BOOST 1D engine model built based on a Ford 4-cylinder DI diesel engine.	144
Figure 7.2 Valve lifts for intake valve and exhaust valve.	146
Figure 7.3 Compressor map visualization	147
Figure 7.4 Turbine mass flow at different turbine speed.....	147
Figure 7.5 Turbine efficiency at different turbine speed.	148
Figure 7.6 Boost pressure validation with experimental data.	148
Figure 7.7 Intake air flow validation with experimental data	149

Figure 7.8 Turbocharger performance simulation results during one complete engine cycle at 3000 rpm. (a) Compressor power, (b) compressor efficiency, (c) turbine power, and (d) turbine efficiency.	150
Figure 7.9 Steady-state simulation results at several engine speeds range from 1000 rpm to 3600 rpm. (a) Total injected fuel mass per cycle, (b) total aspirated air mass during one cycle, (c) air/fuel ratio, and (d) brake specific fuel consumption.....	151
Figure 7.10 Steady-state simulation results of the compressor at different engine speeds range from 1000 rpm to 3600 rpm. (a) Compressor rotational speed, (b) compressor work, (c) compressor efficiency, and (d) compressor boost pressure to the engine.	152
Figure 7.11 Steady-state simulation results of the turbine at different engine speeds range from 1000 rpm to 3600 rpm. (a) Turbine work, (b) turbine efficiency, and (c) turbine ratio.	153

List of Tables

Table 3.1 Operating conditions and compressor geometry data	77
Table 5.1 Operating conditions and turbine geometry data	110
Table 7.1 Main engine specifications.....	129
Table 7.2 Combustion parameters settings for different engine speeds.....	131

Abbreviations

ANN	Artificial Neural Networks
BMEP	Brake Mean Effective Pressure
BOV	Blow-off Valve
CFD	Computational Fluid Dynamics
CO	Carbon Monoxide
CO ₂	Carbon Dioxide
DI	Direct injection
ECU	Engine Control Unit
EGR	Exhaust Gas Recirculation
GDI	Gasoline Direct Injection
HC	Hydrocarbon
HCCI	Homogeneous Charge Compression Ignition
HP	High Pressure
ICE	Internal Combustion Engine
LES	Large Eddy Simulation
LP	Low Pressure
NO _x	Nitrogen Oxide
NO	Nitric Oxide
NO ₂	Nitrogen Dioxide
PM	Particulate Matte

PR	Pressure Ratio
RPM	Revolutions Per Minute
SI	Spark Ignition
VAT	Variable Area Turbine
VFT	Variable Flow Turbocharger
VGS	Variable Geometry System
VGT	Variable Geometry Turbocharger
VNT	Variable Nozzle Turbocharger
WGT	Waste-Gate Turbocharger
1D	One Dimensional
2D	Two Dimensional
3D	Three Dimensional

Nomenclature

A	Reference Flow Area (m^2)
B	Fractional Area Blockage
b	Blade Height (m)
bl	Blade Loading
block	Blockage
C	Absolute Fluid Velocity (m/s)
C_f	Surface Friction Loss Coefficient
C_p	Specific Heat Capacity at Constant Pressure $\text{J}/(\text{kg}\cdot\text{K})$
C_v	Specific Heat Capacity at Constant Volume $\text{J}/(\text{kg}\cdot\text{K})$
ch	Chocking
D	Diameter
Diff	Diffusion
D_i	The Mean Hydraulic Channel Diameter of Impeller (m)
D_d	The Mean Hydraulic Channel Diameter of Diffuser (m)
d	Passage Width (m)
E	Diffusion Coefficient
f	Friction Coefficient
h	Specific Enthalpy (J/kg)

hs	Hub-to-Shroud
hyd	Hydraulic
I	Blade Work Coefficient
K	Loss Coefficient
l_i	The Mean Channel Length of Impeller (m)
l_d	The Mean Channel Length of Diffuser (m)
M	Mach Number
Nu	Nusselt number
Pr	Prandtl Number
Re	Reynolds Number
Sep	Separation
sf	Skin Friction
T	Temperature (K)
Th	Throat
U	Tangential Speed (m/s)
W	Fluid Velocity Relative to Moving Impeller Blades (m/s)
W_C	Compressor Power (KW)
W_T	Turbine Power (KW)
Z_c	The Impeller Blade Number

Greek Symbols

α_{2b}	Fixed Diffuser Inlet Angle
α_2	The Direction of Gas Stream at Diffuser Inlet
β_{1b}	Fixed Blade Angle of Impeller
β_1	Direction of the Gas Stream at Impeller Inlet
α_2	The Direction of Gas Stream at Diffuser Inlet
γ	Ratio of Specific Heats
σ	Slip Factor
ω	Rotational Speed
η	Isentropic Efficiency
θ	Blade Angle
λ	tip distortion factor

Subscripts

f	Friction
h	Impeller Hub
i	Incidence
r	Radial Coordinate Direction
t	Impeller Tip
u	Tangential Coordinate Direction
0	Stagnation State
1	Impeller Inlet
2	Impeller Exit

3	Vaneless Diffuser Exit
4	Vaned Diffuser Exit
5	Volute Exit

Superscripts

*	Sonic Flow Conditions
---	-----------------------

Chapter 1 Introduction

1.1 Turbocharging

A turbocharger is commonly used to increase the air pressure at the inlet of the engine, leading to the increase of the airflow and correspondingly the fuel flow. Consequently an increase in power output can be achieved by increasing the efficiency without much mechanical loss in the engine. Meanwhile, emissions such as soot and NO_x (representing mono-nitrogen oxides NO and nitrogen dioxide NO_2) are reduced with increased air flow, improved air-fuel mixing and decreased combustion temperature. Engine manufacturers are facing high pressure to conform to stringent emission regulations, particularly strict on carbon dioxide (CO_2) and NO_x emission norms. Turbochargers can be beneficial from coping with those regulations and they became very popular in recent years not just for expanding diesel passenger car market share, but also for enhancing gasoline car downsizing and particularly with the recent development in Gasoline Direct Injection (GDI). According to a report from Honeywell, one of the main turbocharger suppliers in the world, passenger vehicles with turbocharged engines have taken 72% of market share, and it has a tendency to increase to 86% by 2017 [1].

Many research results have shown that turbochargers can help reducing the fuel consumption and CO_2 emissions of diesel engines by 20%, while achieving a similar level of power density as gasoline engines [2]. For gasoline engines turbochargers can also increase the peak torque by 60% and the peak power by 30% [3], which provides more space for downsizing. By using turbocharging and downsizing, current turbocharged GDI engines, the fuel consumption gap between the gasoline engines and diesel engines have been shortened from 25-30% to 5-10% [4]. Based on a report published on Honeywell Turbo Technologies Ltd Company website in 2005, the NO_x and Soot emissions for diesel engines with turbochargers are 50% less than that from conventional engines.

Air flow is normally drawn into cylinder using the downward stroke of a piston through intake valves in naturally aspirated automotive engines. Air pressure at inlet of the engine is ambient and it will be increased when it reaches the intake manifold. The air flow was continuously drawn in due to the pressure difference and could provide a high Brake Mean Effective Pressure (BMEP). In the case that the power output is uniformly distributed from the top to the bottom for every power stroke, BMEP is an average pressure value which can be used to evaluate the power output. In other words, it is also a useful tool to measure engine performance with a fixed piston displacement.

Another popular method to improve the volumetric efficiency is supercharging. Different from turbocharging, a supercharged compressor is commonly driven by engine crankshaft. Therefore, supercharging is mainly limited by the engine's crankshaft speed, i.e. the driven power. In situations where the main requirement is the engine's response and fuel efficiency is of secondary importance, supercharging is the ideal option.

Compared with naturally aspirated engines, a well-known drawback of turbocharged engine is turbo lag. The exhaust system first drives the turbine to a high pressure, and then the turbine rotor reaches the required speed to supply the boost pressure. The time taken for this process is called turbo lag. Due to the weight and size of modern turbines, they cannot start spinning until their crank speed reaches about 3500 rpm. Therefore, the power output at low-speeds is generally weak. So for these turbines, techniques such as Variable Geometry Turbocharger (VGT) and two-stage turbocharging are used to reduce turbo lag. As shown in Figure 1.1, a turbocharger consists of a turbine and a compressor which are connected by the same shaft, as shown in Figure 1.1. Turbine is the device which extracts power from the air flow converting the exhaust heat and pressure to momentum. Part of the work output is used to drive the compressor upstream. The choice of the turbocharger depends on the air flow rate through the engine. That is affected by the boost pressure, the cylinders' volume, and the speed.

An intercooler can be applied to improve volumetric efficiency. The working mechanism is to increase the air charge density due to constant pressure cooling which consumes part of the heat generated by the compression process. Reduced air charge temperature also eliminates the danger of knocking combustion for spark ignition (SI) engines. As a result, intercooler can increase induction system efficiency and whole engine energy efficiency [6].

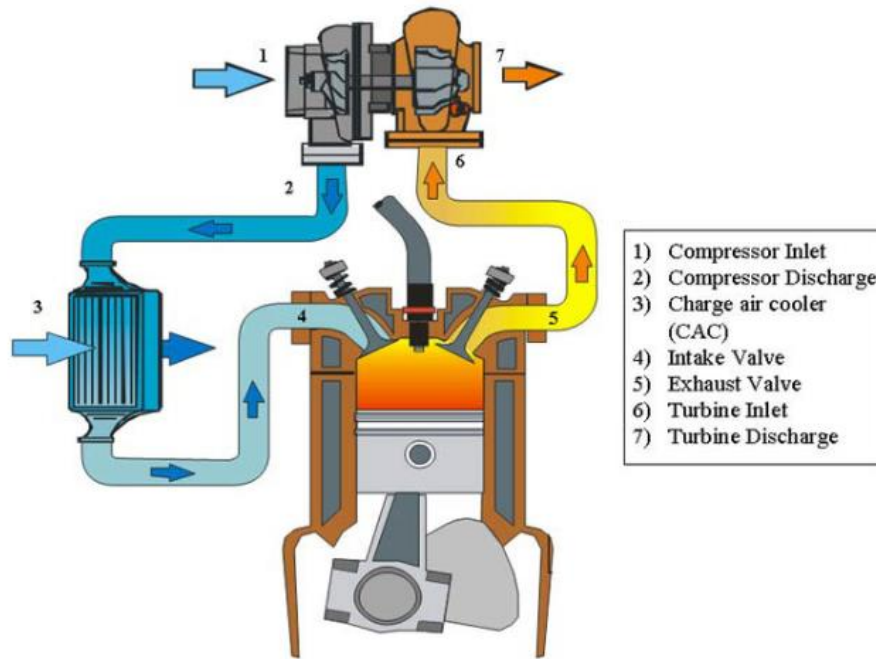


Figure 1.1 Turbocharger for automotive engine [5]

To avoid knocking combustion in turbocharged SI engines, turbocharger is generally controlled by a wastegate. The wastegate can bypass some exhaust flow from turbine. The working mechanism of a wastegate is to bypass part of the exhaust gas through the turbine when the required intake pressure is met. For diesel engines, there is no problem for high intake pressure. The main concern of diesel engine is the inadequate boost pressure under low engine speed or low engine load. Achieving higher boost pressure under those operating conditions is always desirable. To achieve the requirement, VGT (Variable Geometry Turbocharger) technology was developed and applied in diesel engines in recent years [7]. With VGT, diesel engines' full load performance under low engine speed has been improved significantly.

When using turbochargers in SI engines, a high air flow is required under the condition of wide open throttle and high engine speed. With the throttle closed, the compressed air passing through the throttle might cause a surge, leading to the increase of air pressure and possibly damage turbocharger. To avoid this problem, a valve can be fitted between the turbocharger and the throttle to reduce the air pressure which is also known as an anti-surge or blow-off valve (BOV).

1.2 Background

There are a few influence factors for turbocharger performance, such as various geometrical

parameters of the compressor impeller entry, compressor diffuser and turbine impeller. Although blade angle can be designed to match intake gas flow angle, optimised turbocharger performance is normally limited to the situation when mass flow rate is matched with a specific impeller rotational speed. If the operating condition is away from the design condition, it could result in non-optimised flow incidence. Then the consequent loss which is the so called incidence loss would take place caused by flow separation and mixing of high and low velocity flow. As the loss is correlated to the incidence angle, this means the turbocharger is not ideally matched to the optimised operating condition over the most of mass flow range.

Ideal turbocharger design matching is to achieve optimised flow characteristics in both compressor and turbine, for applying exhaust energy to gain optimum overall performance. For applications in diesel engines, the operating range covers a wide speed and load range. There would always be some operating conditions where turbocharger is working other than optimum conditions. Then applications of turbochargers with wastegate over free-floating types in SI engines and Variable Geometry Turbochargers (VGT) in diesel engines can provide more flexibility. During matching processes, a computer-based tool will be very helpful for assessing possible problems, if the tool has following features:

- A robust tool to predict engine performance;
- A useful tool which is capable of predicting the turbocharger performance accurately;
- A reliable tool which is able to couple the turbocharger and engine models efficiently; and
- A reliable tool which is capable of carrying out the optimisation for the whole system.

Coupling all the components in different stages of the turbocharger correctly is an efficient way to maximise the overall efficiency of the turbocharger. That could ensure the required air flow going through the engine providing the lowest soot and NO_x emissions. The main purpose of the turbocharger model is to assist in turbocharger design and matching. To develop a robust turbocharger tool, it must include the capability of predicting the performance of both compressors and turbines separately and the coupling aerodynamically and thermodynamically [8].

Although various turbocharger models have been reported in the literature, centrifugal compressor models have been overlooked which can provide detailed calculations of centrifugal compressors. In most of the work reported in the literature, losses across most compression components are normally treated using a slip factor or loss coefficient [9,10]. Such a treatment could result in effects

of individual loss cannot be clearly characterised. The lack of understanding of those losses makes it difficult to achieve ideal turbocharger optimisation and matching.

In this thesis, assessment of all losses developed for a compressor model will be demonstrated. Detailed parametric study on effect of each loss mechanism on compressor performance was implemented. The model was then combined with a turbine model for formatting a turbocharger model, which was then tested in a 1D engine model for turbocharger performance assessment. It was shown that the developed models of compressor and turbocharger was capable of minimising magnitudes of various losses and provided support for overall turbocharger performance optimisation.

1.3 Aim and Objectives

The research carried out in this thesis is aiming to investigate and develop a turbocharger model, which consists of radial compressor and radial turbine models, which are based on detailed evaluation of energy flow and various losses through compressors and turbines. Then these models can be used to analyse performance of various turbochargers, including VGT (Variable Geometry Turbocharger) and multi-stage turbocharger.

The specific objectives of this research are listed in the following:

- Develop a centrifugal compressor model employing thermodynamics principles to analyse and predict components performance using geometrical and experimental parameters.
- Evaluate some loss sub-models in the compressor model with the possibility to investigate its flow characteristics.
- Develop a radial turbine model by applying various thermodynamic laws and dynamic balance equations to calculate components performance and losses based geometry data.
- Validate the developed compressor model and turbine model against experimental data collected from a turbocharged diesel engine for further improvement to meet requirements for assessing practical turbocharger compressor and turbine designs.
- Couple compressor and turbine models to assess some actual turbocharger performance for model valuations.
- Couple the developed turbocharger model with a dynamic model of a diesel engine, and examine the performances and its compatibility for practical engine performance analysis.

1.4 Thesis Organisation

This chapter demonstrates the background of the research problem. The following chapters explain the process employed to develop a model for analysing turbocharger component losses, performance optimisation and stage matching with an engine. A literature review for relevant turbocharger technologies, various researches on performance analyses and loss assessments in compressors and turbines, and relevant applications of various study methodologies of turbocharger performance characteristics is presented in Chapter 2. Chapter 3 describes a compressor model which consists of basic analysis of flow characteristics and energy losses through compressor components. Chapter 4 consists of compressor model validation against experimental data, simulation results and discussion. Chapter 5 describes a turbocharger model which is the coupling of the compressor model and the turbine model. Chapter 6 shows validation of the turbocharger model, by comparing simulation results against experimental data of a turbocharged diesel engine. The investigation of Variable Nozzle Turbine performance is also included this chapter. Chapter 7 describes an application of the developed turbocharger model into a 1D engine model to check the adaptability of proposed model. Chapter 8 provides conclusions and recommendations for future work. Figure 1.2 shows the structure and layout of this thesis in a chart flow format.

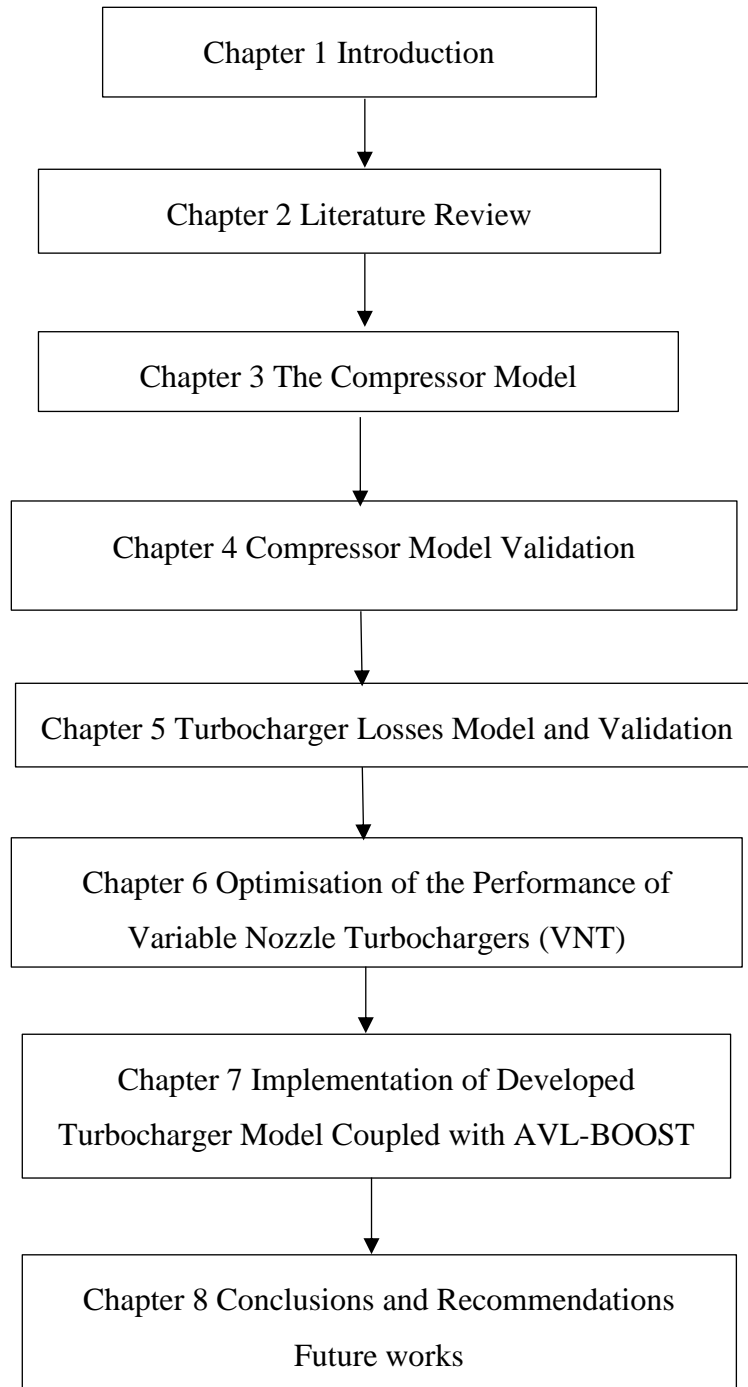


Figure 1.2 Thesis organization

Chapter 2 Literature Review

2.1 Current Turbocharger Technologies

Emission regulations have been more tightened globally for Internal Combustion (IC) engines with time to achieve a greener environment. Generally speaking, emissions from IC engines are commonly referred to Hydrocarbon (HC), Carbon Monoxide (HC), Carbon Monoxide (CO), Nitrogen Oxide (NO_x) and Particulate Matter (PM). All of them are regulated to a limited amount according to relevant emission regulations. Among all, the balance of achieving better fuel economy and reducing NO_x and PM emissions (especially for diesel engines) is the most challenging task. To solve the problem, engine-boosting systems have become popular in the last few decades. For example, the common approach used to improve the engine performance and reduce the emission is to apply turbochargers in diesel engines. As shown in figure 2.1, it is vital for manufacturers to provide more efficient engines with turbochargers if necessary as the emission regulation will be stricter with time and fuel is also more precious as the nature of being non-renewable energy [11].

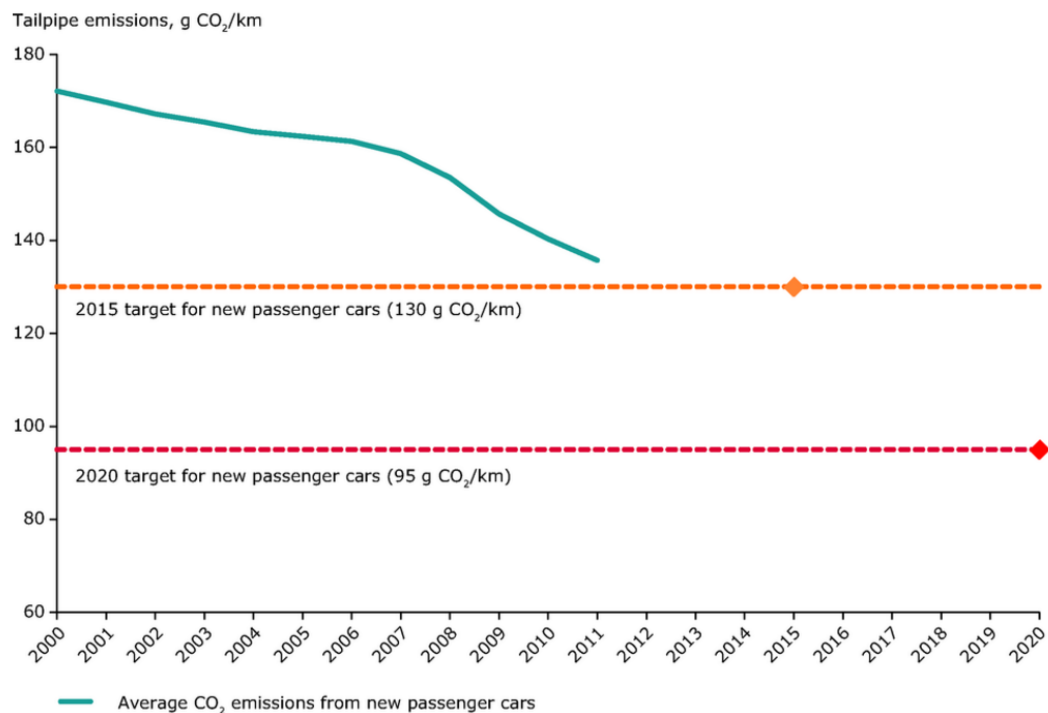


Figure 2.1 Average emissions for new cars (g CO₂/km) [12]

In terms of increasing engine energy efficiency with reduced CO₂ emissions, downsizing is one solution to this problem. Engine downsizing is commonly implemented by using an engine with smaller displacement which can still deliver the same power and torque. To achieve that, an exhaust turbocharger is commonly used. Currently turbocharging is an efficient method to improve fuel consumption in automotive engines. It is normally employed together with direct fuel injection, variable valve actuation and other downsizing techniques [12, 13]. As shown in figure 2.2, those techniques can efficiently reduce CO₂ emissions, therefore makes it competitive with diesel engines in terms of fuel consumption, while keeps exhaust pollutant emissions very low by using the three-way catalyst technique [14, 15].

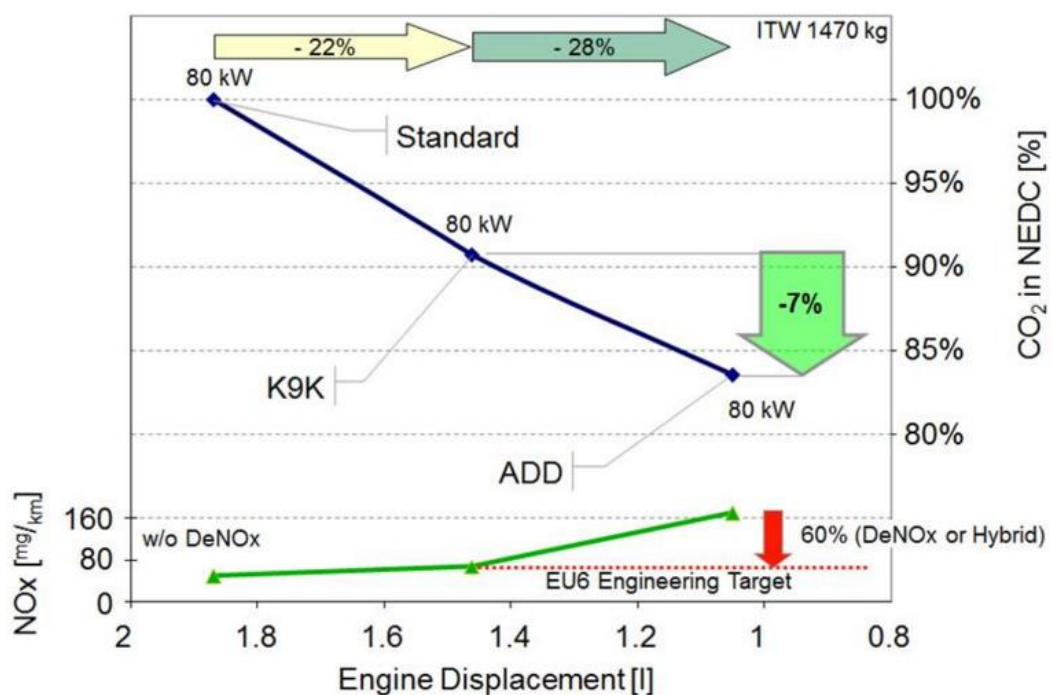


Figure 2.2 CO₂ reductions by downsizing for 1470kg class [16]

Engine turbocharging employed in all diesel applications, have been extensively applied to Spark Ignition (SI) automotive units as a way to reach the required performance level with downsizing engine [3]. It is challenging to have a robust turbocharging system which is capable of achieving good engine torque performance and great vehicle drive ability, particularly in the case for small SI engines with fewer cylinders (often lower than four in recent units). That was caused by the wide load and speed range experienced in road applications and the magnitude of unsteady flow effects in intake and exhaust circuit [5].

Turbocharger has remained almost unchanged in its basic shape over the last few decades.

Manufacturers have been seeking ways to improve its performance and efficiency. Considerable and steady progresses such as improved sealing techniques and reduced component vibration have led to significant improvement in performance [10]. For manufacturing, it is stated that turbocharger efficiency has been pushed from approximately 40% to 60% by improved material and design techniques, with pressure ratios increased at the same level [17]. Figure 2.3 shows the average increase in pressure ratio of ABB manufacturing turbochargers during the last 40 years, clearly illustrating how demanding improved power and manufacturing have affected the turbocharger market.

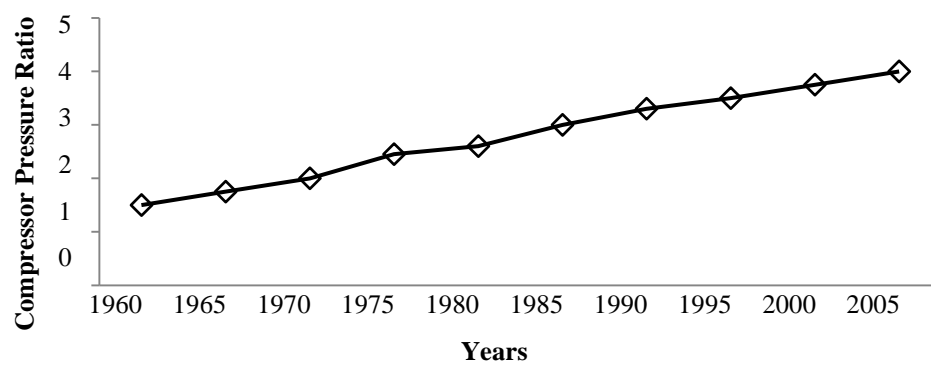


Figure 2.3 Statistical mean compressor pressure ratio of ABB turbochargers over the last 45years.[18]

2.1.1 Positive Displacement Compressors and Other Superchargers

The basic working mechanism for positive displacement compressors is that air is sucked in and compressed. The commonly seen positive displacement compressors are reciprocating piston compressors, rotary screw compressors, rotary vane compressors and scroll compressor. For twin-screw superchargers, air is drawn into a pair of meshing lobes as seen in Figure 2.4. Then it is held in the pockets of the rotor lobes. Later the air is compressed inside the rotor housing by changing the size of the air pocket and then discharged to the next stage.

Superchargers are commonly used to increase engine power in the low and middle speed range while turbochargers are better to achieve ultimate horsepower at high engine speeds. The advantage of employing superchargers is that their low speed boost response which could provide duplication of power characteristics of a large naturally aspirated engine. On the other hand, the disadvantage of turbochargers is that the turbochargers lag which requires the turbine system to be accelerated to high speed before it generating any boost. This problem becomes especially noticeable with the use of a high boost and small displacement engine [16].

A screw charging system as shown in Figure 2.4 has been used by Ford Motor Company to develop a 1.0L supercharger Zetec RoCam engine [17]. It was reported that superchargers could provide better peak pressure ratio and isentropic efficiency. Due to its capability of achieving higher isentropic efficiency and a faster boost response, roots concept has been applied to provide more spontaneous engine response behaviour. Matsubara [17] also suggested that mechanically driven positive displacement superchargers are preferred than the conventional ones because their low speed characteristics, transient response time and etc.

Shadi [18] used a similar two-screw supercharger for developing a Homogeneous Charge Compression Ignition (HCCI) combustion passenger car engine: The supercharger used in the experiment is the M90 supercharger. It has a displacement of 90 cubic inches of air per revolution with a volumetric efficiency of 100%, which could not be true in reality. In Silvia's research [19], three electrical screw compressors were employed for delivering airflow up to 0.6 kg/s with a maximum pressure of 8 bar for a turbocharger test rig.

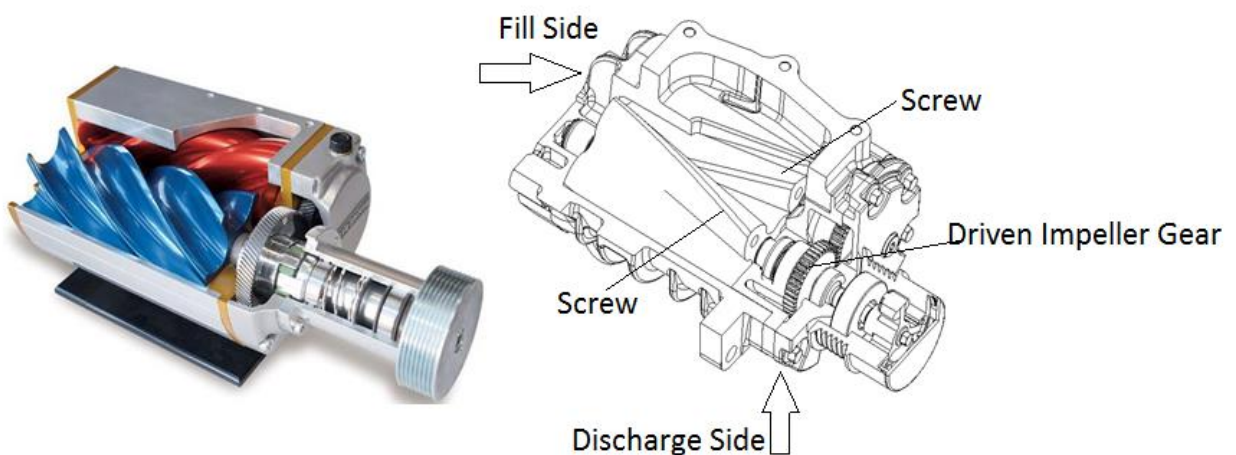


Figure 2.4 Twin-screw supercharger [17]

2.1.2 Waste-gated Turbocharger

As shown in Figure 2.5, a Waste-Gate Turbocharger (WGT) uses a by-pass valve to release some exhaust gas in order to reduce the work produced by the turbine. This is normally applied in turbocharged gasoline engines for avoiding knocking combustion under high engine load condition.

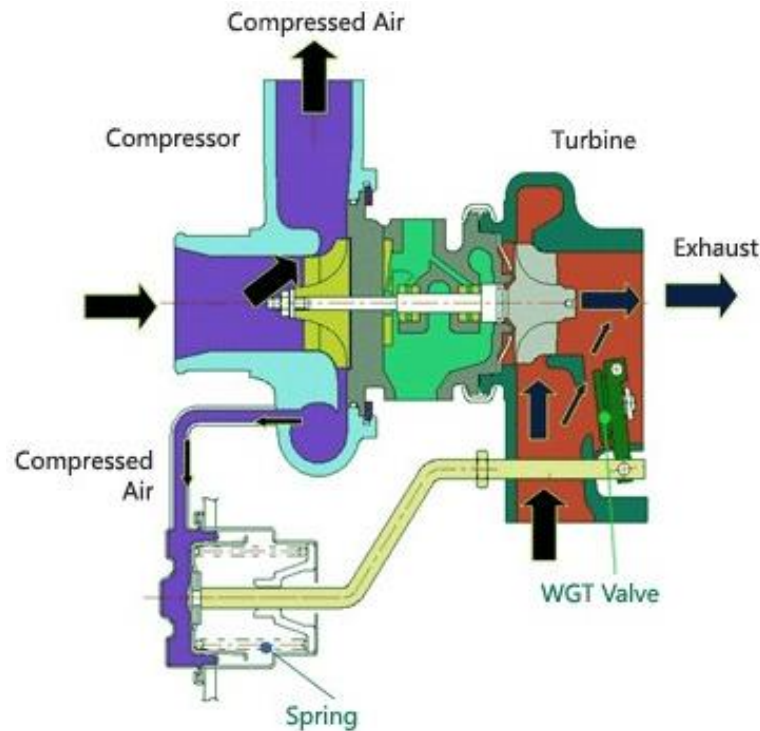


Figure 2.5 Waste-gate Turbocharger [18]

Shadi [18] analysed the efficiency of a small WGT turbocharger turbine with both steady and pulsating flow and the effect of the waste-gate valve regulating device has also been investigated. Results from the steady flow analysis showed that large deviation in efficiency was observed. The actual power of the compressor of the turbocharger was determined by using an external loading device. The deviation was caused by the error in the gas temperature at the exit of the radial turbine. The turbine efficiency was significantly reduced by opening the waste-gate valve and the total mass through the system was applied for the calculation.

In Silvia's research [19], a Waste-Gate Turbocharger was used on an eight-cylinder, heavy-duty diesel automotive engine with direct injection which is part of an urban city bus. The matched compressors and turbines in the engine have improved characteristics for the compressor. The main purpose of matching procedure was to develop and fit a turbocharging system with most optimised performance characteristics for the engine, which could provide better thermal operating conditions and improved overall vehicle performance. Results showed that the output and

performance of the engine were improved and emissions were also reduced.

2.1.3 Variable Geometry/Nozzle Turbocharger (VGT/VNT)

Variable Geometry Turbocharger (VGT) was developed in recent years for improving turbocharger efficiency and responding time. Owing to its superior performance, it has been widely employed in modern diesel passenger cars. When flow volume of exhaust gas and moment energy is low at low engine speed, vanes were closed to increase flow speed. At the same time, the flow is impinged on the tip of turbine wheel and its moment energy increases, as shown in Figure 2.6. With middle and high engine speeds, the vanes are opened up and turbine wheel works in the similar way as fixed vane turbochargers. Although VGT doesn't affect compressor efficiency map, it increases the moment energy of flow to turbine wheel. As a result, compressor can work at a wide range of engine speeds with variable geometry turbines. Turbo lag is normally unavoidable in turbochargers due to the fact that flow at low engine rotational speeds could not make turbine rotates without delay. A Variable Geometry Turbocharger (VGT) is capable of optimising turbine response by changing the flow direction [14, 15]. Variable vanes can be employed in turbine housing to direct the flow in the correct direction into the turbine. In that case, those vanes are commonly controlled by an actuator which can change the angle of the vanes and the variable vanes at different working conditions can be seen clearly in Figure 2.6.

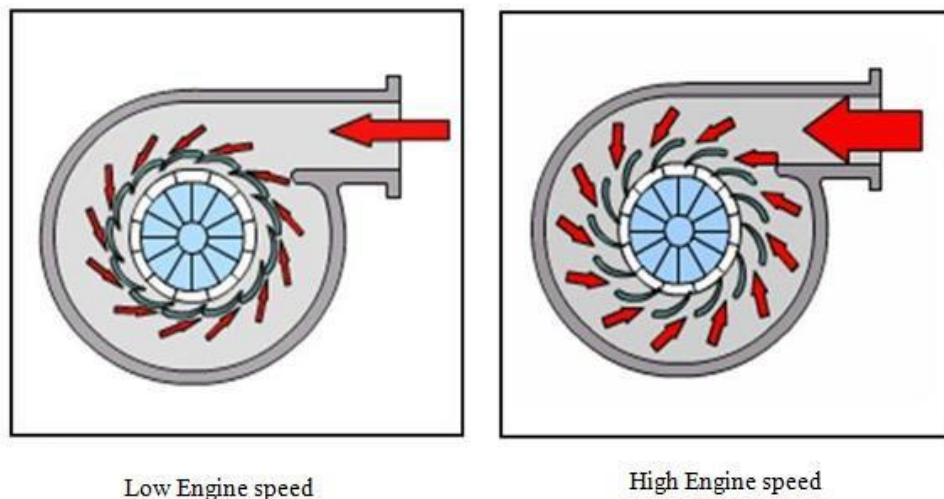


Figure 2.6 Working principles of Variable Geometry Turbocharger (VGT) [14]

Garrett Company is one of the early developers of VGT system. At the end of 20th century, they started to design VGT system integrated with electro-hydraulic actuation system, which includes precise control of vane positions to improve its robustness and stability [15].

In Capobianco's research [14], a passenger car diesel engine has been equipped with a Variable Geometry Turbocharger system which was named Variable Geometry System (VGS) turbocharger. Figure 2.7 shows the experiment results from the engine test bed. It suggested that the engine torque at 1500 rpm can be increased up to 43%, compared with conventional turbochargers.

Compared with the performance of variable geometry turbines and conventional ones with waste-gates, it proved that Variable Geometry Turbocharger could be very efficient to reduce the transient response time of engine and exhaust emissions at the same time [17]. A VGT has been investigated experimentally in the Department of Energetic Engineering of the University of Genoa. Two variable geometry turbines has been investigated: a variable area turbine (VAT) and a variable nozzle turbine (VNT). The characteristics of the VGT were compared with the one for a turbine with fixed geometry waste-gate operating at both steady and unsteady flow conditions. Results showed significant improvement on low speed torque and transient performance by employing VGT.

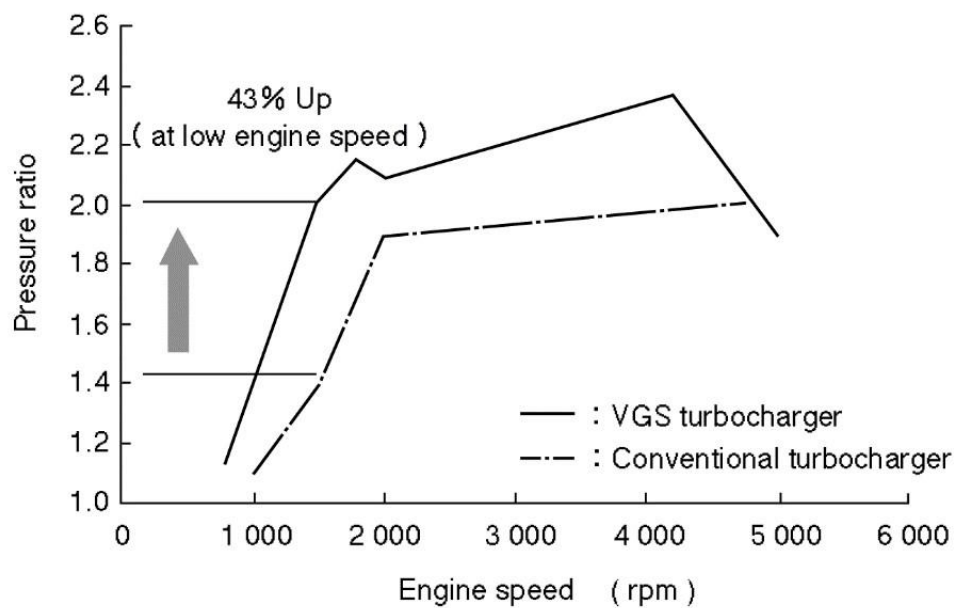


Figure 2.7 Improvement of low speed torque by VGT [16]

With the development of Gasoline Direct Injection (GDI) engines and their applications on passenger cars, it has been explored to use Variable Geometry Turbocharger on small gasoline engines. In Srinivasan's research [7], it showed that Variable Geometry Turbocharger can make automotive engines achieve high and flat torque at low engine speeds. The peak torque was increased by 27% and the engine speed with peak torque was reduced by 1550rpm. The torque curve with engine speeds from 5450rpm to 8000rpm was observed to be constant.

In order to optimise VGT matching, Leduc employed an existing Excel based analytical model to facilitate comparative performance predictions of a Variable Nozzle turbine [11]. No direct comparison of variable geometry turbine predictive accuracy has been made due to lack of supportive data. The effect of nozzle angle and turbine effective flow area on compressor boost pressure ratio (termed arbitrarily as $P2/P1$) was produced. The ability of variable geometry to provide low boost at high engine speeds and high boost at low speeds is clearly evidential.

In Hojin's research [20], the control problem between VGT and EGR with control modelling was examined. A model based control structure for diesel engine with a turbocharger and EGR was designed. The model-based control structure was employed to cope with highly nonlinear control of EGR and VGT, and a robust controller was designed by using a sliding mode control method.

2.1.4 Multi-stage Turbochargers

Over years, two-stage and multi-stage turbocharging have been used in automotive engines to achieve higher specific power output, lower fuel consumption and lower pollutant emissions within regulation. In Shahed's research [13], a two-stage turbocharger has been investigated which consisted of a low pressure (LP) and a high pressure (HP) section. Since air was pressurised through two stages, higher boost pressures was provided which increased the mass flow of the charged air into cylinders. At the meantime, without degradation in the efficiency, a higher EGR rate was achieved. The use of two-stage turbocharger was significantly beneficial for performance and transient response. Several typical issues of multi-stage turbocharger have been investigated, including the serial coupling of two compressors. Results showed degradations of surge margin and choking limits, therefore the operating range has been reduced.

Hyundai Motor Company presented a two-stage turbocharger with serial configuration as one of their best candidates. The turbocharger can provide high power with high rotational speed and higher low-end torque [12]. The performance of the turbocharger with a two-stage VGT has been investigated and methods to improve the fuel efficiency have also been explored. Results showed transient response of two-stage turbocharger was faster than the one of VGT with a rotational speed in the range of 1000~2500 rpm.

In Marcello's research [5], a two-stage turbocharged heavy-duty diesel engine has been investigated experimentally and numerically by focusing on its transient performance. The turbocharger system (as shown in Figure 2.8) consists of a high-pressure stage and a low-pressure

stage. The HP section has a twin-entry turbine while the LP section has a VGT. Results showed that the turbocharger model has to be modified to provide a good correlation for the experimental data. The configuration of the turbocharged investigated was potentially capable of providing higher transient EGR.

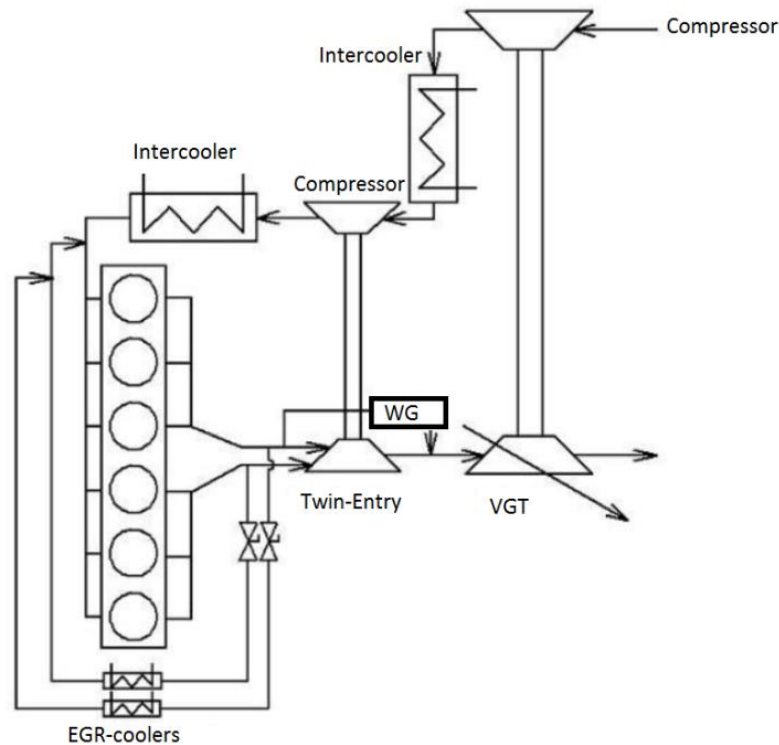


Figure 2.8 A two-stage turbocharger [5]

In Winkler's research [15], a two-stage turbocharger in serial has been investigated. Good performance can be achieved with two-stage turbocharging at high altitude with reduced air density, i.e. lower pressure ratio. At the meantime, the specific power output could be increased to 100HP except for extreme operating conditions.

Muzaffar [21] developed a control model for two-stage turbocharger. Results showed that the model has high accuracy, easy to calibrate and requires reasonable time to run. The model was developed and validated using a diesel engine with a two-stage turbocharger. The simulation of the turbocharger was characterised using the principle of modularity with a high pressure EGR loop.

In terms of multi-stage turbocharger integrated with supercharger, Infineon Technologies AG demonstrated a system that included a WGT and an electrically operated supercharger (e-turbo), as shown in Figure 2.9 [20]. Test bench evaluation showed that the speed of the e-turbo can achieve 70,000 rpm within 0.5 second. To achieve that, the electrical load needed for that will be 3kW.

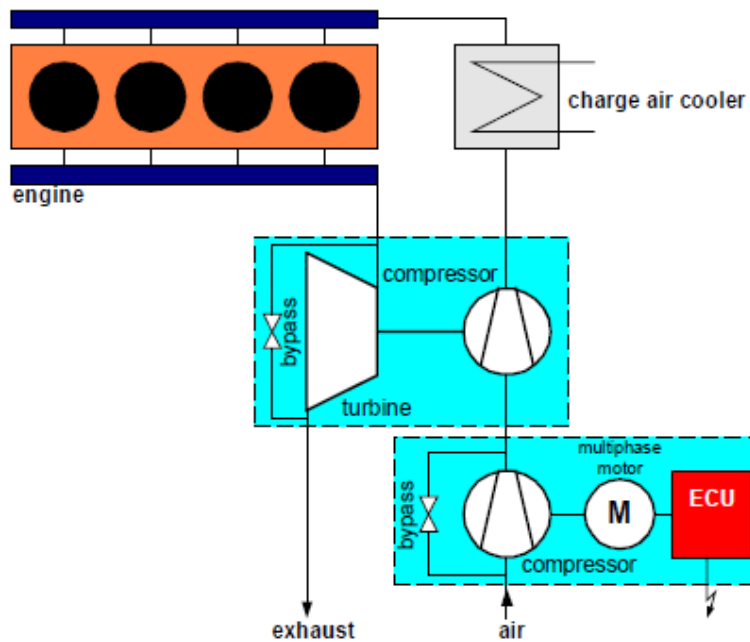


Figure 2.9 A multi-stage turbocharger and an e-turbo [20]

The stage loss of multi-stage turbochargers has been investigated experimentally by Winkler [15]. On the contrary, Leonard [22] has numerically investigated the performance of multistage compressors and turbines using CFD when they are working with steady and transient condition.

2.1.5 Electric Turbochargers

Electric motor/generator can be added to the bearing housing of standard turbocharger systems to improve the transient response time and low-end torque. At the meantime, the power input into the compressors will also be increased. Thus, better fuel efficiency can be achieved with better downsizing, down speeding and higher efficacy for the turbocharger. Furthermore, higher power output can be obtained by employing electric motors at steady state operating condition. Thus turbocharging system with electric motors is another very useful method to improve fuel consumption and reduce CO₂ emission.

In Nicola's research [23], and turbocharger with electric motors has been designed for medium

duty diesel engines which are not suitable for on-road vehicles. The efficiency characteristics of the motors and the turbine have been obtained. The experimental data of the electric motors were obtained by modifying an electric motor assisted turbocharger. In that case, the compressor was removed and the bearing housing was added on gimbal bearings as shown in Figure 2.10. The efficiency of the electrical motor was used to determine the reaction torque of the bearing housing, power output and thus the speed. Experimental data showed that the peak efficiency of turbine which has a value of 69% was achieved with a velocity ratio of 0.65 with the vane opening at 60% its fully opened position. The peak efficiency of the electric motor of more than 90% was achieved with a rotational speed of 120,000 rpm with a peak shaft power of 3.5 kW operating at motoring mode and 5.4kW operating at generation mode.

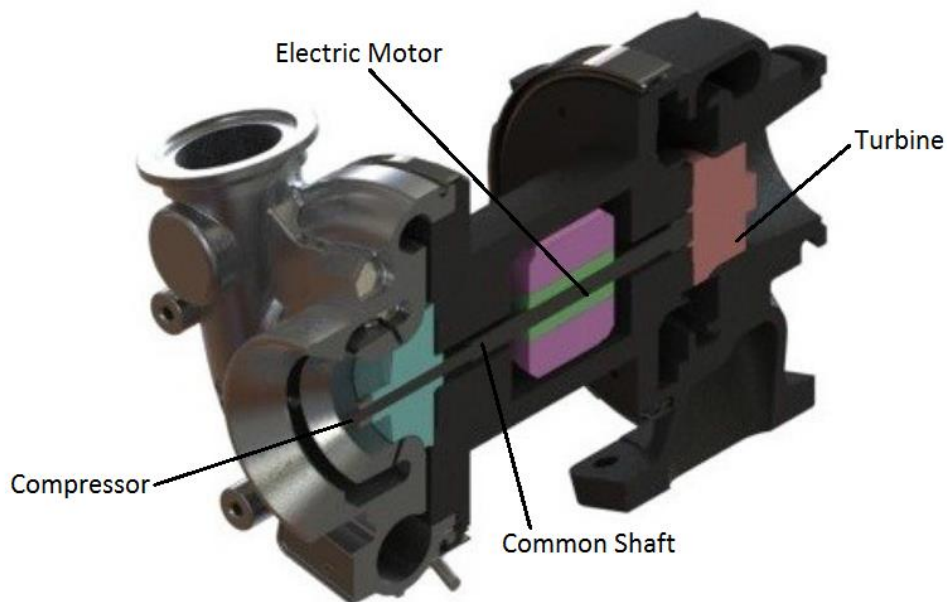


Figure 2.10 An electrically assisted turbocharger [23]

In Thomas's research [24], Infineon Technologies AG used an e-turbo with a turbocharger as a system solution for overcoming the drawback of turbo lag for turbocharged engines. Bandel [25] has investigated the response behaviour of VGT, E-booster and P-booster: It was instrumented and coupled with a "p-Booster" to introduce a burst of compressed air to compressor inlet. The dynamic response of three turbocharged SI-engines has been investigated with different dynamic boosting. A numerical model has been developed for turbocharged downsized engines with variable turbine geometry. It was believed that it would provide much better load response. Results showed that exhaust temperature could be properly controlled with significant penalties in efficiency. To make most out of the e-Booster, its response time should be

less than the one the turbocharger used.

2.1.6 Twin Entry Turbines

Before reaching the turbine wheel, the air flow coming out from different engine cylinders is separated by a twin entry turbine housing to maintain pulse energy. Typically, a six-cylinder engine is separated into two even groups and the consequence firing sequences are separated by a crank angle of 240 degrees. Each of the twin entry housing was fed with air flow coming out from those two groups of cylinders respectively.

Minimising periods of windage (instantaneous mass flow falls to zero) can provide the best possible situation within one engine cycle for the superposition of three evenly-spaced pulses, producing a better mean turbine efficiency. Many modern four-cylinder engines have used this approach. Even though the average turbine efficiency per entry case of this approach will be lower than the three cylinders, it is better than the one for a single entry turbine since it decreases the interaction between pulses and exhaust process of other cylinders. Nowadays, twin entry turbines are becoming more and more popular with the automotive engine manufactures, while it was set as a standard for larger industrial diesel engines [30].

At engine operating condition, partial admission conditions have been applied to a twin entry radial turbine. In that case, flow at inlets is changing with time. At partial admission conditions, when the twin-entry turbine has the maximum air flow, the turbine experience extreme conditions. The performance and detailed flow features of twin-entry radial turbines have been investigated numerically and experimentally at both full and extreme partial admission conditions [31]. It was concluded that the lowest entropy gain factor was predicated at extreme conditions with the shroud side entry completely closed. While at equal admission conditions, optimised incidence angle has been achieved at the inlet of the rotor.

The unsteady performance of a twin-entry variable geometry turbine has been investigated experimentally by Hamel et.al [32]. In that study, the test has been done on a single-entry and twin-entry variable geometry unit by modifying a commercial unit without nozzle. For comparison purpose, the key features of the turbines have been kept the same. Results from full admission tests showed that the air intake capacity of the twin-entry turbine was different for two entries at different pressure ratios. In most cases, pressure ratio was found to be 13% higher at the shroud end entry than the hub end entry. However, the swallowing capacity is similar between both turbine entries during out-of-phase testing. Compared with the single-entry turbine without nozzle, the average

efficiency of each cycle for both the single and twin entry turbine with nozzle had a deviation of up to 32% at quasi-steady condition.

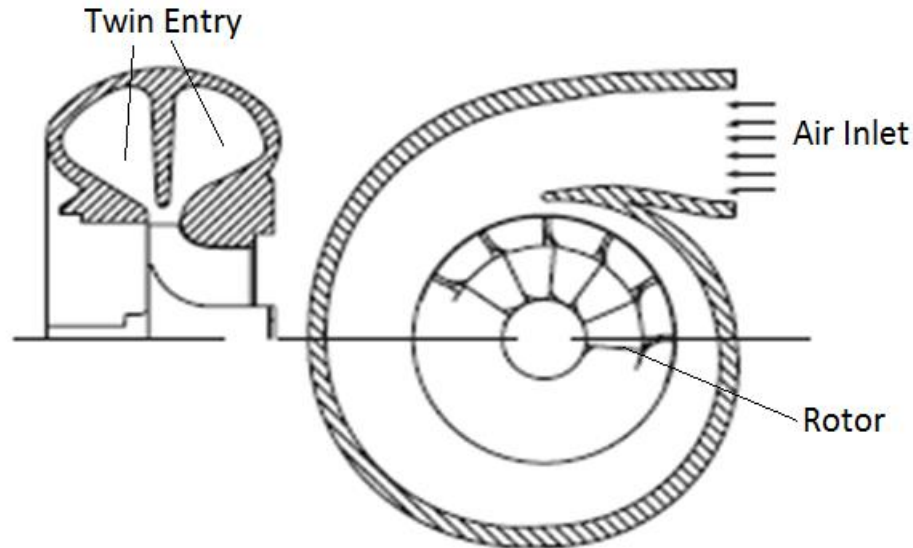


Figure 2.11 Cross section of the twin-entry radial inflow turbine [32]

In Ubanwa's work, steady flow turbine performance was obtained at several different speeds at both full and partial admission conditions [35]. The mass flow and efficiency characteristics of the two entries were significantly different. The mass parameter reached minimum with the shroud side fully closed and reached maximum at full admission conditions. Compared with the ones at hub side at partial admission conditions, the swallowing capacity and mass parameter of a twin-entry turbine at shroud side was always higher, due to fewer losses including the housing geometry and twin-entry turbine losses and blade loading loss.

Results showed lower efficiencies were predicted at partial admission than full admission conditions. That was caused by the non-uniformity at inlet of the rotor at partial admission. However, higher efficiency and more flow have been predicted in shroud side than the hub side that was caused by the secondary flow near the rotor inlet. Lower efficiency at full admission conditions was predicted with high mass flow ratio between the shroud and hub side. Partial admission was found to be the extreme condition with windage, higher blade loading loss and minimum efficiency with shroud side fully closed. It is a common phenomenon in turbochargers with pulse flow.

2.1.7 Variable Flow Turbocharger (VFT)

Figure 2.12 shows a variable flow turbine turbocharger from Honda R&D Co Ltd [36]. A fixed vane separates the two scrolls of this turbine (inner and outer circumferences). The gas was directed into inner or both scrolls by a flow control valve located at turbine inlet port. Within its range, the turbine capacity can be changed arbitrarily to provide the characteristics of both small and large capacity turbines emphasising low-speed torque and high power respectively.

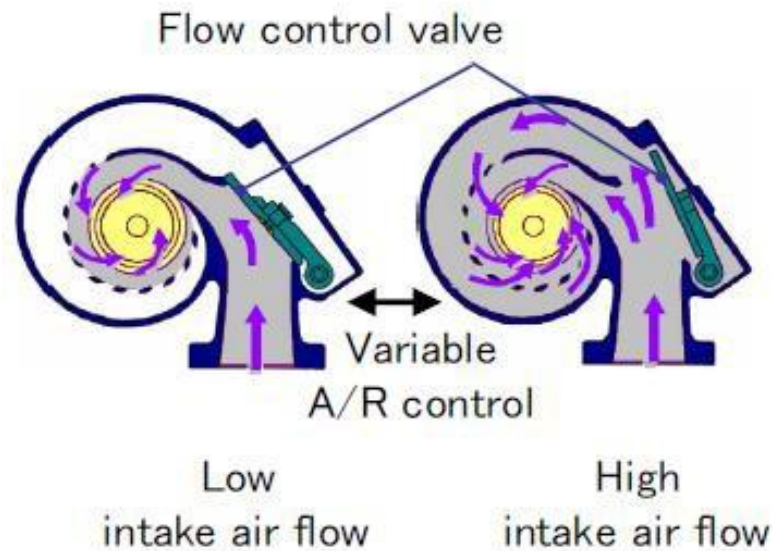


Figure 2.12 Variable Flow Turbocharger (VFT) [36]

Compared to large displacement naturally aspirated engines, turbocharged engines are more efficient. However, conventional turbo engines suffer from insufficient torque at low engine speed with little exhaust energy, and also suffer from the significant delayed response time when it shifts from low to high load range. VFT has been shown to provide a larger range of torque characteristics that includes the low and high speed characteristics of small and large turbocharger respectively.

2.2 Methodologies for Turbocharger Total Performance Optimization

2.2.1 Experimental Investigation

Although computer modelling has played more and more important role for turbocharger R&D, experimental methods are still contributing to the main function of developments. In addition to those tests integrated with engines on engine testbed [17, 36], initial analysis of compressor and turbine dynamics is also required on gas flow testbed, without the involvement of the engine [37, 38, 39].

Generally steady flow test rig is widely used for turbocharger performance optimisation. As shown

in Figure 2.13, a compressor of a twin-entry turbine has been used in the test to quantify the steady state performance of the turbine at both full and partial admission conditions [40]. The test rig has two inlets and three screw compressors. A pressure of 13-bar gage and a mass flow rate of 0.4 kg/s can be achieved. In this line, using electro-pneumatic valves controls mass flow rate. With the help of an electrical heater unit, the temperature of the compressor air can be achieved up to 200°C to avoid condensation around turbine blades due to a high temperature drop caused by air expansion. Three orifice plates were installed in the turbine and one in the compressor to measure the mass flow at steady state and they were calibrated to BS 104211. Two separate pipes were installed at the inlets of the turbine with mass flow and other instrumentations and control valves in each pipe. With regard to unsteady test as shown in Figure 2.14, a test rig was used for turbocharger [41] characterisation using transient and steady flow conditions by simulating intake and exhaust flows of small passenger vehicles. The test rig was composed with a blower, a centrifugal fan capable of providing 600 m³/h of air with a maximum gauge pressure of 70 kPa (0.7 bar).

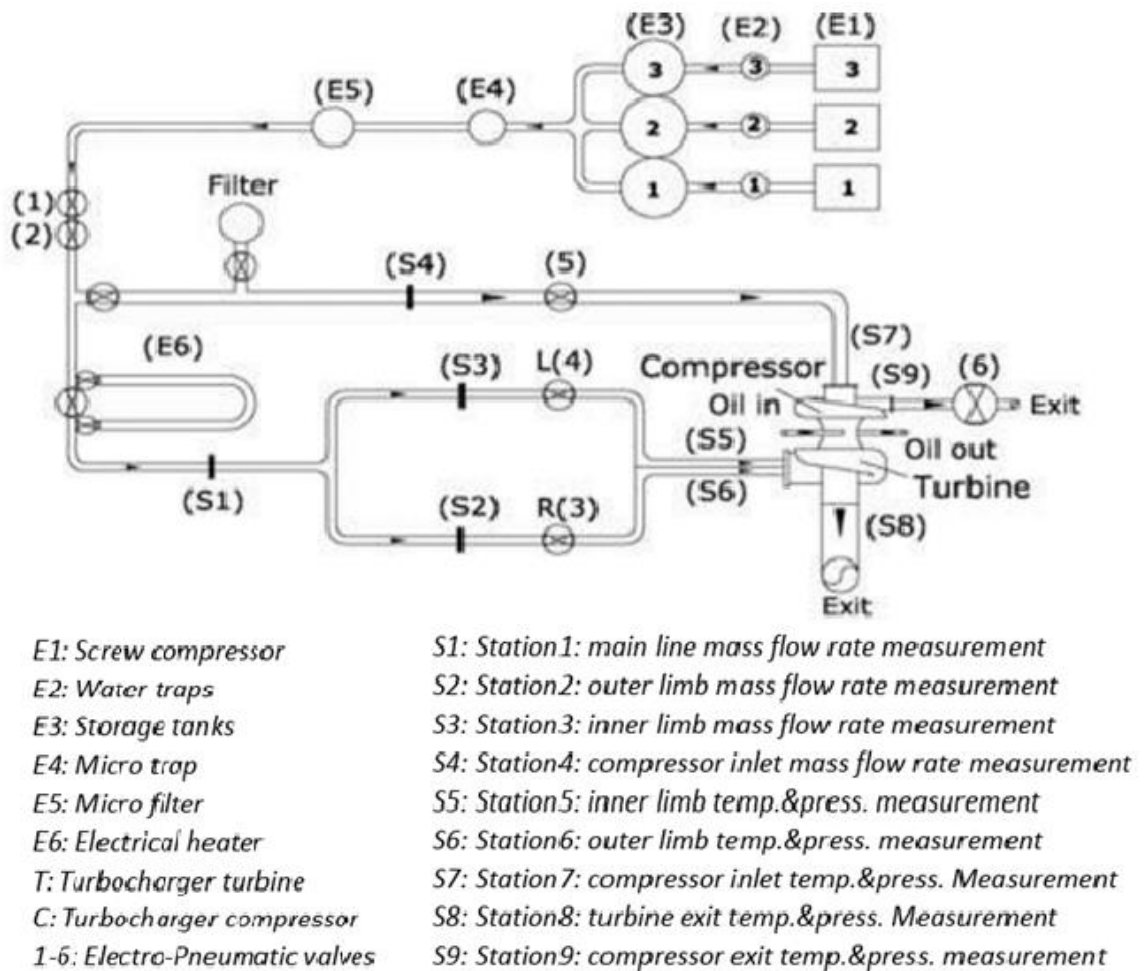


Figure 2.13 A steady flow turbocharger test rig [41]

In Moraal's research [42], two unsteady test rigs with different flow pulse generation methods for turbocharger performance experiment were demonstrated. As shown in Figure 2.15, the test rig has been investigated with both steady and pulsating flow on both single and two entry components. The first test rig used a Variable Valve Actuation cylinder head to generate the pulsating flow to control the valve opening profile. The arrangement is also possible to extend experimental investigations to subsystem level. For instance, exhaust circuit geometry could be changed by installing different manifolds. Furthermore, engine transients can be simulated by using throttle valves integrated in the flow distributor. A second pulse generator system is provided with two diametric slot rotating valves, trailed by a variable rotational speed electrical motor.

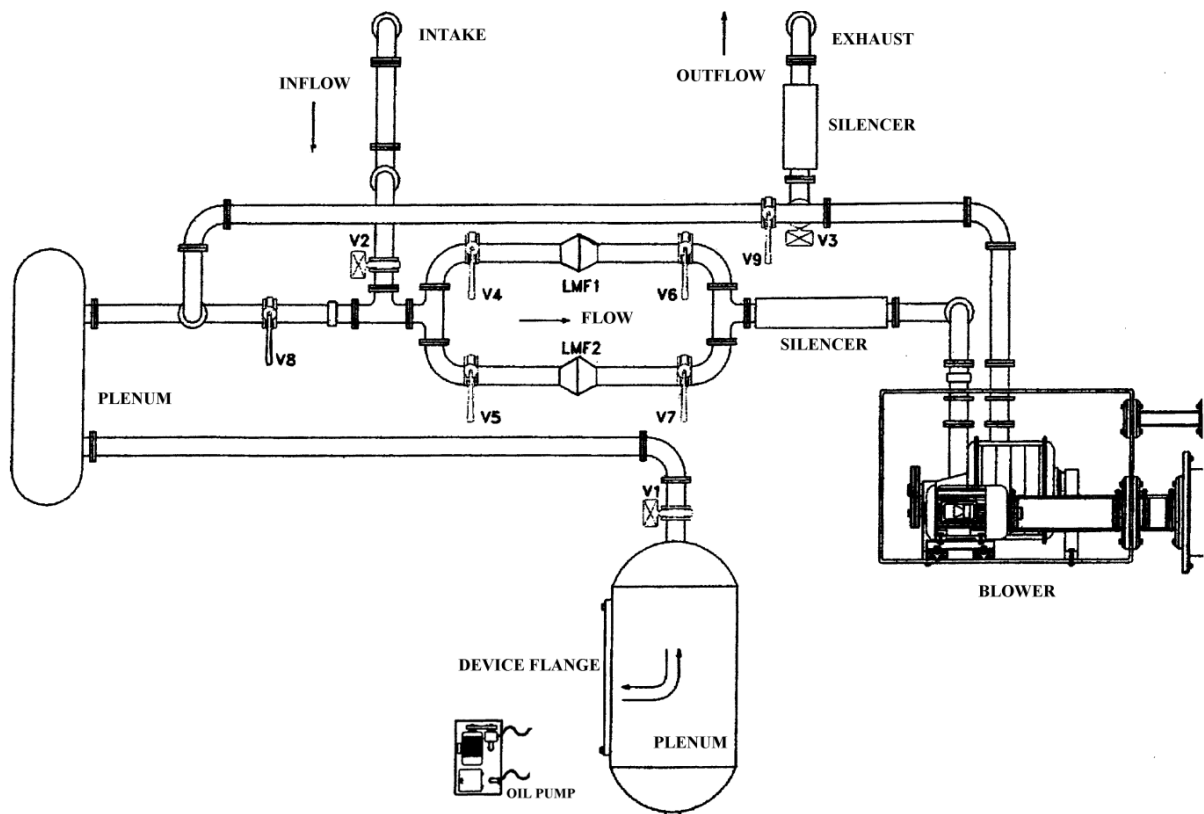


Figure 2.14 Unsteady turbocharger test rig [41]

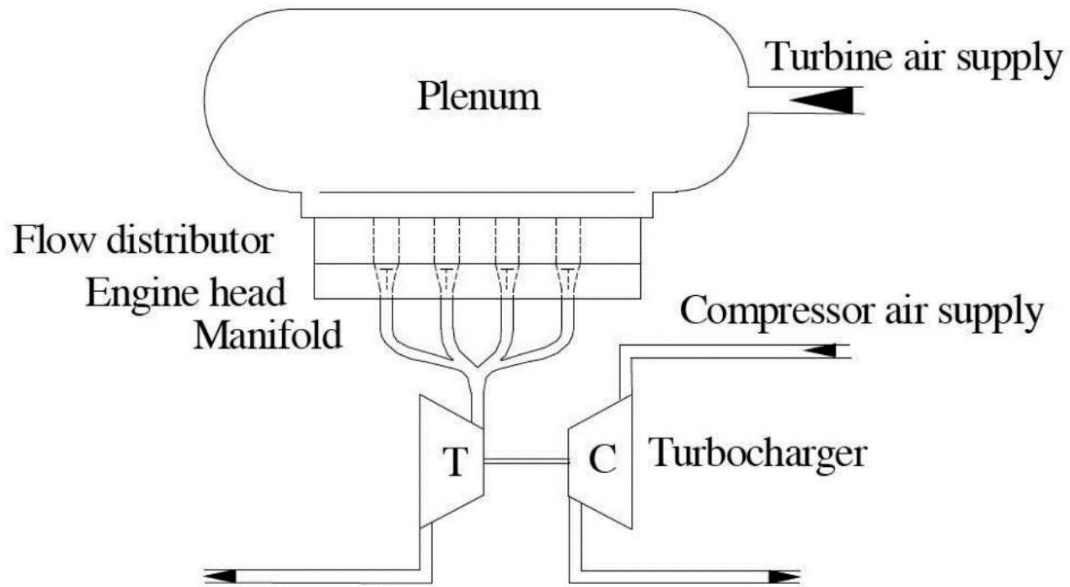


Figure 2.15 Pulse generator system with VVA cylinder head [42]

In Piscaglia's research [41], a special flow test rig was employed for investigating compressor intake swirl effect. The test rig consisted of a single stage centrifugal blower which delivered air flow with a rate of $1.5 \text{ m}^3/\text{s}$ with 1m water gauge pressure. A very fine mesh filter was applied at the inlet of the system and followed by a conical diverged duct and a settling chamber.

Muzaffar [42] tested a turbocharger turbine on a cold flow gas stand which has been loaded by a dynamometer specifically designed for turbocharger turbine performance test. The dynamometer has a magnetic rotor revolves between two steel plates (stators) generating eddy currents which are dissipated as heat. The load was adjusted by changing the gap between the stator and rotor. The maximum testing speed was 63,000 rpm which corresponds to around 110,000 rpm for typical diesel engine turbocharger operating conditions. The maximum operating power was 50kW.

In Zhang's research [43], inter-stage loss of a two-stage turbocharger has been tested on steady flow hot gas turbocharger test rigs.

2.2.2 Modelling of Total Turbocharger Performance

It is critical to predict the performance of a compressor when designing a turbocharger. It will be beneficial to make sure the compressor is working in the correct range according its characteristic map and also helps with the optimized coupling with other components in the system, such as

volute, impeller, and diffuser. The turbocharger manufacturers normally provide performance characteristics with limited rotational speeds, pressure ratios, and mass flow rate. A tool to well predict the compressor performance can produce a device with optimum specification and that will be useful for designers at the design stage. Several numerical methods have been developed to predict the performance of automotive turbocharged engine at both steady and unsteady flow conditions. Canova et al. [5] developed such a tool for a two-stage heavy-duty diesel engine with turbochargers including EGR especially with transient condition to optimise the performance of turbocharger and engine, and emissions.

The performance of three different compressors has been numerically simulated by Moraal and Kolmanovsky [44] using four different methods with neural networks. The tool was capable of predicting their curve fitting accuracy, model complexity, generality and extrapolation capabilities. Curve fitting methods were used to predict the characteristic of the turbine when it is with wastegate and has variable geometry. That study was focused on compressor performance improvement. In Galindo's research [45], 1D turbocharger model for engine performance modelling was demonstrated. The performance of the turbocharger has been determined through various heat transfer conditions and measurements.

The major issue preventing the applications of turbocharger is the modelling of the compressor map. Generally, the compressor map is inserted directly into the Engine Control Unit. However, this method occupies large memory spaces and on-line interpolation requiring a significant amount of CPU time. An applicable radial compressor model to all turbochargers with either Spark Ignition (SI) or diesel engines was proposed by Sorenson et. al [46], which is a more compact, accurate, and rapid method.

2.2.3 Computational Fluid Dynamics (CFD)

CFD plays a very important role in predicting compressor and turbine characteristics due to its capability of analysing flow details across the whole flow domain. Those information can then be used to inform the designers and also very useful for optimisation purpose if necessary. Many researchers' work could prove that CFD is a very useful tool for that purpose. Hamel et al. [18] has numerically investigated the performance of a mixed flow turbine with pulse flow at the inlet using a commercial code ANSYS-CFX. The mesh was dominated with tetrahedral and prism elements and boundary layers were employed near the wall using ICEM CFD as shown in Figure 2.16. For boundary conditions, total temperature was applied at the inlet with pulse signal and rotational speed. A one-dimensional simulation was validated with experimental data having the same pulse

frequency. As shown in Figure 2.17 a good agreement against experiment suggesting that the commercial code is capable to capture the key flow feature with pulsing flow.

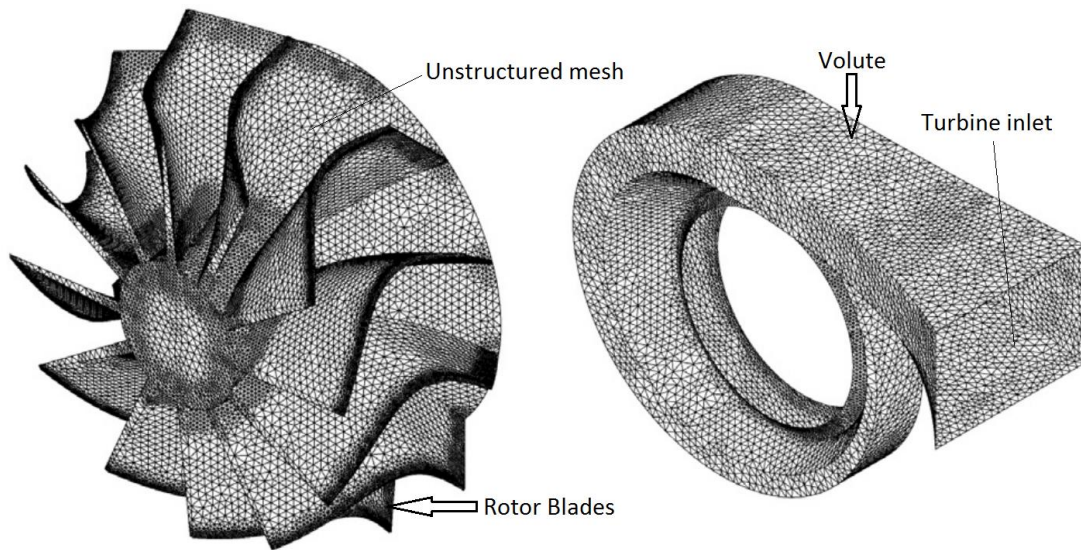


Figure 2.16 Computational grid of a Mixed Flow Turbine [32]

Lenoard and Adam [18] have performed numerical simulations on multistage turbomachines using a quasi-one dimensional CFD model. The objective of that study was to provide a reliable CFD model which is capable of evaluating the performance of compressors and turbines within a reasonable time. The core of the CFD model was to solve Euler equations using a time marching, finite-volume method. The interactions between blade rows were evaluated by adding source terms into the Euler equations. Those source terms were derived from analysis of row-to-row velocity triangles, losses and deviations at the mid-span of the blades. The input for the CFD model was geometrical data from the turbomachine and the model was capable of predicting the entire characteristic map of compressors and turbines. Based on that the model is fast regarding to CPU time consumption, it has the potential to be coupled with other tools for optimisation purpose and predicting gas turbine performance.

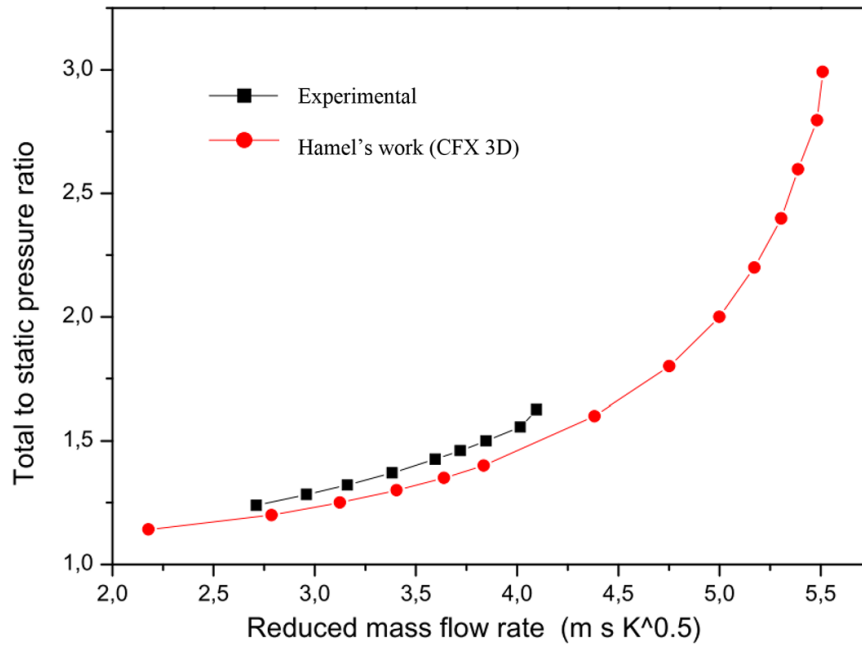


Figure 2.17 Turbine total to static pressure ratio versus the reduced mass flow [32]

Hellstrom and Fuchs [47] performed a Large Eddy Simulation (LES) on a turbocharger to study effect of secondary flow at the inlet of the turbine. Souza and Filho [48] have also performed CFD simulations on a radial turbine. Good results were predicted with different turbine geometrical parameters. For instance, volutes with different geometrical parameters would affect both the mass flow characteristics and the characteristics of efficiency against the expansion ratio.

2.2.4 Turbocharger Control Modelling

With the development of various electronic controlled turbocharger technologies, such as Variable Geometry Turbocharger (VGT), Variable Flow Turbocharger (VFT) and E-turbo, control strategy has played a very important role for predicting turbocharger performance. A turbocharged diesel engine model with Exhaust Gas Recirculation (EGR) based on control structure was investigated by Jung et al. [18]. Guidelines of control strategies have been proposed. The predicted engine performance came with uncertainties hand in hand. A sliding model control method then was proposed to solve that problem. In Bozza's research [46], an active control technical named 'Drive Itself' is used for surge control of a centrifugal compressor driven by an electrical motor. Results showed that stable operating conditions which were away from the surge line have been achieved by controlling the rotational speed.

Canova et al. [13] has developed a control-oriented model for a two stage turbocharged Diesel

engine and that method was believed to be an efficient tool which can be used for optimisation, calibration and dealing with control issues with high accuracy at the mean time. A bottom-up modelling approach was adopted to characterise engine system. Each component in the system has been treated as dynamic using conservation of mass flow and energy.

Qi et al. [49] investigated performances of a centrifugal turbocharger compressor with artificial neural networks (ANN) using CFD. The key inputs required are impeller geometries, end-wall, and blade sectional camber curves while the main output of the system are the total adiabatic efficiency and total pressure ratio for each optimisation cycle and results showed that compressor performance has been greatly improved.

2.2.5 One Dimensional (1D) Simulation

1D simulation for turbochargers is necessary at design stage to achieve optimised designs for different components in the system. Therefore, a robust tool could save time significantly in the design cycle and reduce costs with better design of radial compressors. Although CFD methods has been improved with time, 1D models still play important roles for predicting turbocharger performance due to its accuracy and required computational time.

The coupling of turbocharge inside an engine is usually achieved using 1D code [50] and the results can be used for further CFD analyses [51]. The characteristics of turbine and compressor are commonly needed from the manufacturer. Then the 1D code can be used for data extrapolation to obtained turbine and compressor characteristics [52, 53, 54]. This will introduce inaccuracies in the calculation procedure. Besides, performance maps are generally derived from test benches with turbocharged internal combustion engine at steady state, typically operating under unsteady flow conditions.

Bozza and Bellis [55] have numerically investigated a one-dimensional model for a centrifugal compressor with complex 3D shaped impeller wheel. The model used measured geometrical data of a 3 backswept vane compressor as input. Correlations for various flow losses and slip effect have also been investigated.

Nasser and Playfoot [11] have developed a turbocharger selection model using variable turbine angles as input. The model was also based on a single entry fixed vane angle turbocharger matching model. Like most other 1D models, conservation of mass, energy and momentum has been solved in a 1D manner. The exhaust manifold loss without undesirable turbine inlet temperature profile was predicted with a heat transfer sub-model. The flow through the compressor was assumed to be

non-isentropic and the accuracy of the model for predicting flow at the compressor exit was enhanced by using a one-dimensional, semi-empirical loss calculation.

Chiong et al. [30] investigated the geometrical effects of a twin entry turbocharged turbine with full pulsating flow using a 1D numerical model. Several turbine volute models with different levels of complexity have also been investigated. There are other various 1D models, such as the work reported by Vavra et al. [36] which was a method using average pressure data at the inlet and outlet of the turbine and turbocharger speed as input. Japikse et al. [37] has developed a 1D model for design and manufacture. In Gimelli's and Fontana's work [56, 57], The optimisation of performance and coupling of the turbocharger has been investigated using a GT-Power 1D model and results showed that a better turbine design with realistic unsteady conditions can be achieved in the design cycle.

With one dimensional simulation, the model building and simulation can be completed in a relatively short time since one dimensional (1D) model can be simpler than two dimensional (2D) or three dimensional (3D) models. However, as 1D simulation can't take all details of effects of geometry and flow structure into account providing poorer accuracy 1D simulation, compared with 3D simulation.

2.3 Compressor Loss Models

2.3.1 Introduction

Previous work showed that Zero- and one-dimensional models are able to predict global turbocharger and engine behaviour with reasonable computational costs [58, 59, 60, 61]. Therefore, proper modelling of compressor and turbine provides very useful information for the good design of turbochargers and engines with good coupling and control strategies. At the meantime, proper boundary conditions at exhaust manifold end have to be considered for predict the performance of compressor and turbine to make sure the correct coupling between the engine and turbocharger. The energy transformation and the nature of irreversible processes has also to be considered [62].

The turbocharger matching process may take a number of cycles which generally involve matching simulation, matching test and repeated design. To have optimal matching performance and minimum matching time and cost, appropriate and accurate compressor model and turbine model must be established and exact sub-models for various losses must be developed [63].

To develop a proper numerical model, losses encountered in compressors must be appropriately dealt with. The origin and effects of loss mechanism were discussed in details in references [64, 65]. Losses in centrifugal compressors are commonly classified as incidence loss, friction loss, clearance loss, backward loss and volute loss [66, 67, 68]. The capability and limitation of the exist models for predicting incidence loss was reported by Whitfield and Wallace's [69]. The two commonly used models are constant pressure incidence model and NASA shock loss model [70, 71, 72]. Results showed that those two models were very similar for predictions of incidence loss of radial compressors [70]. Westin [71] has investigated pipe flow using the energy and momentum equations and friction loss was predicted using the proposed approach reported in [70, 73].

Watson and Janota [75], Ferguson [76], and Nisenfeld [77] etc. investigated two major losses; the incidence losses and the fluid friction losses in both impeller and diffuser. It was reported that the stable operating range of the compressor could be determined by analysing incidence loss and friction loss. To obtain the compressor efficiency, back flow loss, clearance loss and other losses in the volute have also been considered. Inlet casing loss, mixing loss and leakage loss are negligible for some specific conditions.

2.3.2 Inlet Suction Losses

The flow characteristics at the inlet of channel flow have been investigated by Lakshim [78]. The uniformity of the velocity was very good with the initial degree of taper for the channel and increased with the increase of the degree of taper for the channel. The change of the channel will change the direction of the flow going into the impeller since it was located upstream. The uniformity of the velocity will also be affected to deviate from the original status. Separation can be caused corner flow [55]. To overcome that problem, the blockage can be determined by the following equation which is correlated with inlet suction loss:

$$\Delta h_{Suc} = f_{Suc} \frac{C_0^2}{2g} \quad (2.1)$$

where f_{Suc} refers to the inlet suction loss coefficient. Results showed that f_{Suc} was affected by different types of the inlet. C_0 is the absolute velocity at the inlet.

2.3.3 Incidence Losses

Geometrical parameters of the compressors are affected by the losses caused by the rotor incidence and vaned diffusers. A parametric study of predicting that kind of loss was investigated by Whitfield and Wallace [79]. Two commonly used methods are “NASA shock loss theory” which was reported by Watson and Janota [74] and an incidence model with constant pressure which was reported by Whitfield and Wallace [79].

As reported by Watson and Janota [74] those methods can predict very similar results for radial compressors. However, the incidence angle at predicted zero loss was different from different methods [79]. For the constant pressure incidence model, zero loss was predicted with zero incidence which is different for the results predicted from NASA shock loss model.

Different incidence will occur due to different mass flow in the characteristic range. The predicted loss from the second model was reported to be correlated with the mass flow rate. It was reported by Ferguson [81] that incidence loss increases with the reduction in mass flow when it is below the design value. Therefore, the compressor characteristic is steeper when the mass flow is lower than the design point and it was reported to be right skew by Sepulchre and Kokotović [82] and Wang and Krstić [83].

Impeller: As shown in Figure 2.18, W_1 is the relative velocity of the inlet flow. At off-design condition, a mismatch between fixed blade angle β_{1b} and direction of main stream $\beta_1 = \beta_1(U_1, C_1)$ will normally occur.

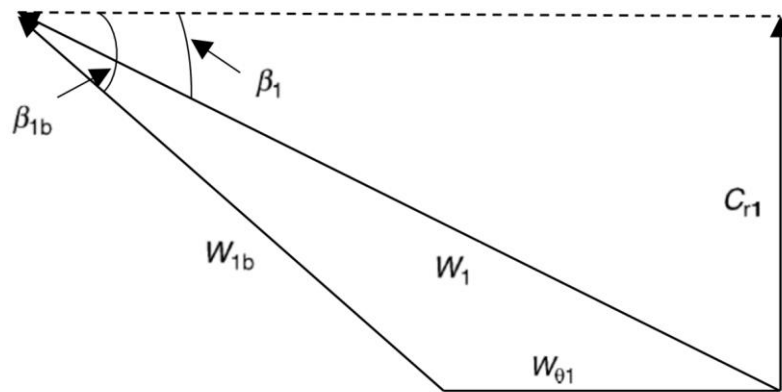


Figure 2.18 Incidence loss at the impeller inlet [83]

Diffuser: As reported by Watson and Janota [74], losses in vaned diffuser can be defined in the same fashion as incidence loss in impellers. To define that, the assumption has been made that the velocity of the flow at the inlet of the diffuser is changed with time to accommodate with fixed diffuser inlet angle α_{2b} as shown in the velocity triangles in Figure 2.19 where C represents the

absolute velocity. All details can be seen in Figure 2.19.

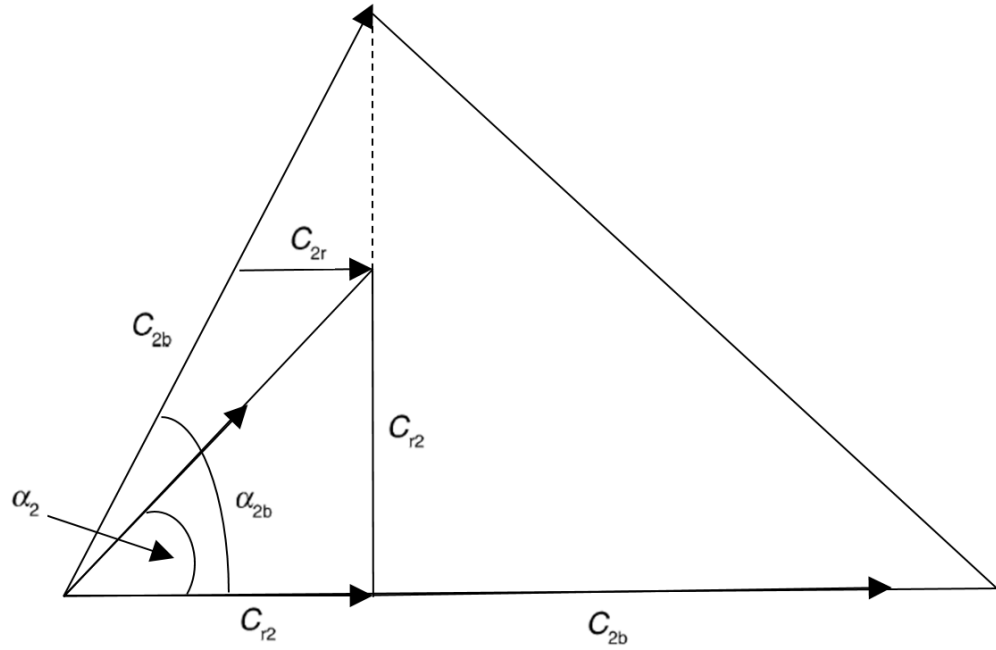


Figure 2.19 Incidence loss at the diffuser inlet [74]

Meese [85] suggested impeller loss coefficient had a significant rise at incidence angle below 3 degree, when flow was pushed to work close to the choke condition. When the diffuser is operating at low mass flow condition (normally positive incidence will occur), loss coefficient of the incidence loss is not significantly affected by rotational speed of the impeller resulting in a high work output from the impeller. On the other hand, the loss coefficient will be greatly affected by the rotational speed in high mass flow condition with negative incidence, therefore it will lead to more loss and minimum work output.

2.3.4 Frictional Losses

Impeller: Friction loss is commonly defined as reported by Ferguson [83]:

$$\Delta h_{fi} = C_f \frac{l_i}{D_i} \frac{W_{1b}^2}{2} \quad (2.2)$$

where C_f refers to surface friction loss coefficient, l_i refers to mean channel length of impeller and D_i refers to mean hydraulic channel diameter of the impeller. To calculate the friction loss, constant area of cross section of the pipe was used. Friction loss coefficient C_f can be defined in the following [74]:

$$C_f = 4f \quad (2.3)$$

where f refers to the friction factor which is significantly affected by Reynolds number which can be determined by Ferguson [83] or White [77]. Blasius' formula shown as below is used:

$$f = 0.3164(Re)^{-0.25} \quad (2.4)$$

It was reported by [77], Equation 2.4 can be used for turbulent pipe flow with low roughness and with Reynolds number Re below 10^5 which is typical value for the one in radial compressor stage according to Strub et al. [85]. The mean hydraulic diameter D for channels can be obtained as:

$$D = \frac{4A}{a} \quad (2.5)$$

where A is the cross section and a is the perimeter as the same geometry corresponding to the hydraulic diameter. It was reported by Baljé [86] that good agreement has achieved between theoretical and experimental data for compressor blade passages using Equation 2.5.

Nasser and Playfoot [87] reported surface friction loss coefficient (C_f) had a considerable effect on channel friction loss. Unfortunately, no material in literature has been found that suggests suitable values for this coefficient. Bozza and Gimelli [88] suggested the effect of friction forces along tangential direction cannot be ignored, because tangential velocity is usually much higher than radial component. As known, in fact, the conservation of tangential momentum is really valid for a frictionless flow.

2.3.5 Volute Loss

For volutes, there is one type of loss referred to volute loss, which commonly exists due to their inability of extracting the radial kinetic energy out of the diffuser. It was reported by Cumpsty [89] that it lays within 2-5 percent of the efficiency:

$$0.02 \leq \Delta\eta_v \leq 0.05 \quad (2.6)$$

It was also reported that the volute loss in compressors is higher with vaned diffusers than annular diffusers since in the radial direction the component carries more weights for the total kinetic energy.

2.3.6 Clearance Loss

There is commonly a gap between the impeller and its casing referred to tip clearance which allows the impeller to rotate without touching the casing. For unshrouded impellers, there is leakage flow in the tip clearance flowing from the pressure side to the suction side of the impeller blade. Then the flow mixes with the passage flow. The tip clearance loss is caused by the mixing of the leakage flow and the main stream.

As reported by Jansen [90], the leakage flow goes in the tip clearance with contraction of the geometry and comes out from the tip gap and expands to the passage. The converging and diverging of the geometry will affect both the leakage flow and the mixing with the passage flow by introducing loss. The blade loading characteristics was used to evaluate the pressure drop across the tip gap. The total pressure loss was calculated by applying standard loss factors to the processes of the converging and diverging of the geometry leading to the clearance loss model reported by Jansen [90]:

$$\Delta h_{cl} = 0.6 \frac{\varepsilon_c}{b_2} C_{\theta 2} \left\{ \frac{4\pi}{b_2 Z} \left[\frac{r_{t1}^2 - r_{h1}^2}{(r_2 - r_1)(1 + \frac{\rho_2}{\rho_1})} \right] C_{\theta 2} C_{m1} \right\}^{1/2} \quad (2.7)$$

where ε_c is tip clearance. C_{m1} is the inlet velocity of the impeller at meridional direction, and b_2 is the width of the outlet of the impeller.

2.3.7 Backflow Loss

At certain conditions, flow coming out of the impeller reverses to the blade passage due to the negative pressure drop near the tip. There is a higher chance for this to happen when the flow has a high absolute angle at the exit of the impeller in the meridional direction. In other words, the larger the flow exit angle α_2 , the higher change for the recirculation to occur.

Another recirculation loss model was developed by Oh et al. [70] and flow angle distribution has been focused on. A hyperbolic functional form of the correlations has been used to link the loss distribution.

2.3.8 Heat Transfer Losses

Heat transfer loss of a compressor has been analysed and validated using experimental data by Cormerais et al. [91]. It was suggested that heat transfer from turbines to compressors had significant effect on compressor performance and therefore it is not eligible. Then the compression

process has to be considered as non-adiabatic. It was also suggested that calculating compressor mechanical power directly from temperature measurements is not recommended. To get the power on the shaft, heat flux can be used which can be derived from those temperature measurements. Therefore modifications are also needed for the calculation of isentropic efficiency. Furthermore, most of the turbocharger maps provided by manufacturers have high turbine inlet temperatures. And that is why heat transfer has to be considered before applying turbocharger maps to the relevant engine models. To achieve that, a method has been proposed to account for heat transfer when turbocharger performance maps are used. The convective turbine and compressor heat transfer coefficients are estimated with the Nusselt number correlation:

$$Nu = 0.024 \cdot Re^{\frac{4}{5}} \cdot Pr^{\frac{2}{5}} \quad (2.8)$$

where Re is Reynolds number and Pr is the Prandtl number. Pr is a dimensionless number which can be regarded as the ratio of kinematic viscosity to thermal diffusivity, and it can be calculated as

$$Pr = \mu C_p / y \quad (2.9)$$

where μ is the dynamic viscosity, C_p is the specific heat and y is the thermal conductivity.

2.3.9 Inter-stage Losses

The inter-stage loss of a two-stage turbocharger has been investigated by Westin and Burenius [92]. The performance maps constructed from the measured data were then used to calculate a composed TST-map with the assumption that there is no loss between the two stages. Then the composed TST-map was compared with the one constructed from measured data. The difference between these two maps was believed to be caused by the inter-stage loss when the assembling of the stages with restricted space such as fitting into a car. However, it was suggested by the breakdown that the inter-stage loss was not all the loss, which contributed to the difference of those two TST-maps. The efficiency and pressure ratio were also affected by the structure of the secondary flow from upstream to the downstream of the turbocharger such as eddies, vortices, turbulence and etc. However, the influence is not purely negative. Sometimes it can also lead to positive effects such as increased surge margin for HP compressor since LP compressor generates a co-swirl at HP-compressor inlet. It was reported that the efficiency was decreased by approximately 8% and pressure ratio was changed by 4%.

2.4 Turbine Models

For losses inside turbines, the majority of the models can be applied with compressor loss models with adjustment to boundary conditions for turbine flows. In this section, some models for turbine losses will not be discussed since the theories behind are similar to the compressor loss models discussed previously. Those models for turbine losses, which are different from the ones for compressors, will be discussed in detail.

2.4.1 Volute Losses

Generally speaking, performance data are commonly referred to engine performance of turbochargers under steady state conditions. However, engines are normally working at unsteady conditions in real life due to pressure pulsations. It is very common with small SI engines, which have fewer cylinders. In those cases, a wide range of mass flow and pressure ratio occurs in each engine cycle. Furthermore, engine efficiency could also be affected by heat transfer in the turbine section of the engine. To consider the effect of pulsating flow, it is commonly to use a “virtual pipe” which has the equivalent length and volume as the actual engine. The actual characteristic map has also to be applied [93]. It was reported that the turbine performance can be considered as steady state even with pulsating flow and the storage effect is only localised within the volute.

As reported by Spence [94], a method used to predict the turbine performance with both steady and unsteady inlet conditions has been discussed. The performance under unsteady state was simulated using unsteady one-dimensional flow representations. The exit condition of the volute for the unsteady simulation at a specific time was extracted from steady state simulation of the rotor. To generate pulse flow in the turbine, flow was solved using unsteady one-dimensional conservation equations together with assuming quasi-steady state of the rotor on the mean streamline direction. A curved pipe is used to represent the volute which has the equivalent length of the volute obtained from the mean radius with the mean azimuth angle.

Performance of vaned casing turbines has been investigated by Serrano [95] and they are not commonly used in modern turbochargers anymore. The performance was predicted using one-dimensional treatment for the turbine casing. However, the casing model used by Baines and his co-authors is different which is a “filling and emptying” method commonly used in thermodynamic analysis of cylinders in internal combustion engines. That method has been shown with positive results and was possibly improved to accommodate twin-entry casings.

The major difficulty of unsteady flow simulations is due to the flow complexity in nature with three-dimensional effects. However, a full scale three-dimensional simulation of rotor and the casing assembly is intensively computational expensive when the computer resource is limited to a small workstation. Therefore, appropriate simplifications together with empirical data are necessary for this kind of simulations. For instance, tangential variations of the flow at the inlet of the rotor were often eliminated with the help of experimental data [96]. And the difference for performance of turbines with steady, pulsating flow and heat transfer has not been fully understood which is still popular for debate in this research area [97].

2.4.2 Turbine Incidence Losses

Generally speaking, the model for turbine incidence loss is very similar to the one for compressors. However, it should be noted that the flow at the turbine inlet is not the same as the flow condition coming from the outlet of the compressor. Thus compressor slip angle was commonly used in the model which was obtained from experiments [98].

2.4.3 Variable Geometry Turbine Model

Simulations of a Variable Geometry Turbine (VGT) have been investigated by Kessel et al. [99]. The model used took the thermodynamic transition process inside the radial turbine into account. Special treatments have been applied to the nozzle, vaneless space and rotor inlet to employ the relevant experimental data. Pressure drop across any two points in the turbine was defined by using the local efficiency. The same method has also been used for predicting temperature drop, the change in enthalpy and entropy and etc.

A model for predicting the performance of a radial turbine with moving blades was discussed by Nasser and Playfoot [89]. The cross sectional area of the throat was used to calculate the mass flow rate for the VGT. There is no obvious difference between the actual geometrical and the relevant effective section. And that model is similar to the one for fixed geometry turbines reported by Macek et al. [100].

2.5 Summary

In this chapter, firstly literature reviews of turbocharger technologies have been presented together with their advantages and constraints, particularly related to CO₂ reduction. Secondly, previous researches for methodologies used in turbochargers have been discussed. It has been

shown that variable geometry turbocharger and two stage turbocharging have outstanding benefits than others. For variable geometry turbocharger, changing the nozzle angle and turbine effective flow area are very good ways to boost the pressure ratio of the compressor and controlling the boost at engine speeds using the variable geometry is another attractive benefit.

Computational Fluid Dynamics (CFD) is a very useful tool to predict the characteristics of compressors and turbines and could provide very useful information for their optimisation if necessary. However, one-dimensional methodologies were considered to be the most practical method of predicting performance of turbochargers. At the meantime, coupling of compressor and turbine model can be very useful to accurately predict characteristics for turbochargers.

Various losses in compressors and turbines have also been reviewed. There are a few losses which could degrade the compressor performance significantly such as skin friction loss, incidence loss, mixing loss and blade loading loss. On the other hand, other losses have no noticeable effect on the degradation of the compressor characteristics including entry diffusion loss, clearance loss, hub to shroud loading loss and blockage loss. However, both of those two sets of losses have contributions on the formation of the compressor performance map. To improve the accuracy in predicting the turbocharger characteristics and optimise turbocharger with new designs and matching into the engine, those models have to be improved from with time if possible.

Chapter 3 The Compressor Model

This chapter aims to demonstrate a compressor model that applies thermodynamic principles to simulate compressor presentation by calculating individual component performances based on various measurable parameters. During the process of compressor performance prediction, various loss models mentioned in chapter 2 will be employed in this one dimensional compressor model.

3.1 Basic Theories for Compressor Model Construction

As shown in Figure 3.1, a typical centrifugal compressor consists of an impeller and a diffuser. The inlet of the impeller which draws flow in is the inducer or the impeller eye. There are two main types of diffusers: vaned diffuser and vaneless diffusers. A vaneless diffuser or annular diffuser normally diverges. The application of vaned diffuser or vaneless diffuser is dependent on the choice of the compressor. And there is normally a volute followed by the diffuser.

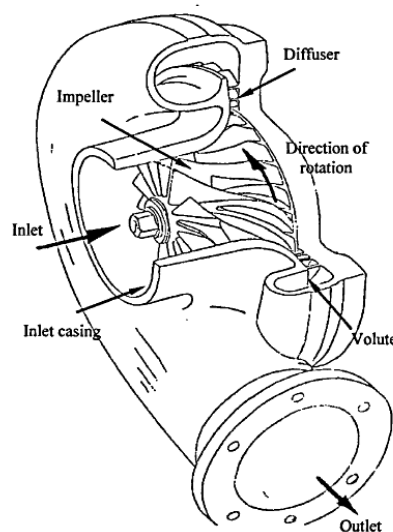


Figure 3.1 A typical centrifugal compressor [62]

3.1.1 The Inlet Casing

The inlet casing is usually a converging nozzle cast as part of the volute casing and is generally made long enough to assume axial delivery and uniform velocity to the impeller. As the inlet casing is stationary, no energy transfer takes place between the casing and the air and the stagnation enthalpy remains constant. Losses incurred in the inlet casing are generally neglected in automotive turbocharger compressors since they are usually caused by up-stream components such as air filters,

a theoretical prediction of the loss is not always possible.

3.1.2 The Impeller

Impeller is very complicated in geometry and also a very important part for the compressor. Energy is transferred through blade rotating and so does the pressure, velocity and enthalpy.

The front section of the blades is known as the inducer. The inducer is generally curved so that the air is directed as smoothly as possible into the impeller to avoid flow separation from the impeller blades. The magnitude and direction of the airflow in the impeller is described by the use of velocity triangles. As shown in Figure 3.2 of the flow velocity triangles, the impeller eye extracts the air in with a velocity of C_1 . The rotational speed of the impeller is defined as U_1 and the resultant vector between U_1 and C_1 is the velocity of the air relative to the rotating vane known as the relative velocity, W_1 .

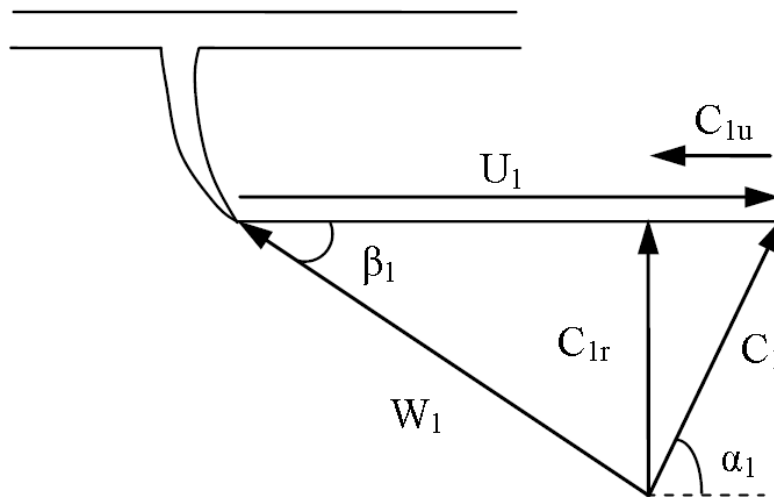


Figure 3.2 Velocity triangle at inducer. (Section through inducer at radius r_1) [46]

Where C_{1r} is the axial velocity of the flow while C_{1u} is the tangential velocity of the flow. α_1 and β_1 are the flow direction relative to casing and to rotor respectively.

The air has an exit velocity of C_2 coming out the impeller, as shown in the exit velocity triangles in Figure 3.3. The impeller tip rotational speed U_2 and the relative velocity, W_2 ideally follows the direction of the blade and the absolute velocity C_2 completes the triangle. The exit gas angle α_2 is the angle between the absolute velocity and the radial direction. β_2 is the angle between the relative velocity and the radial direction. Two further components of the absolute velocity can also be drawn. C_{2r} is the radial velocity of the flow and C_{2u} is the tangential velocity of the flow.

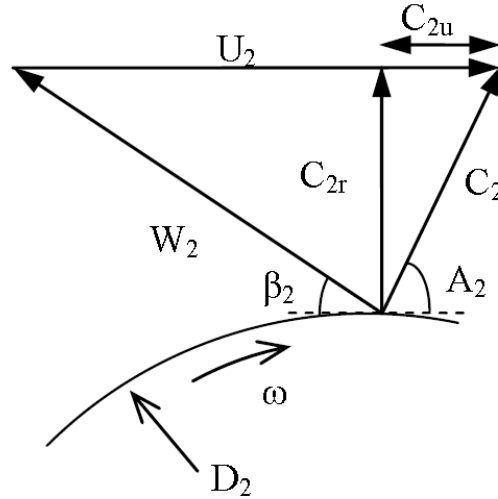


Figure 3.3 Velocity triangles at impeller tip. (Section through impeller tip at radius r_2) [46]

3.1.3 The Vaneless Diffuser

The advantages of the vaneless diffusers are wide range of operation and its cost for manufacture. However one of its disadvantages is its size [47]. The capability of diffusion can be evaluated by the velocity ratio between the outlet and the inlet. When it is assumed that $b_2\rho_2 = b_3\rho_3$, the velocity ratio can be expressed as

$$\frac{C_3}{C_2} = \frac{D_2}{D_3} \quad (3.1)$$

where C_3 is the velocity at the outlet and C_2 is the velocity at the inlet. D_2 is the diameter at the impeller tip and D_3 is the diameter at the outlet. b_2 and b_3 are the width at the outlet of impeller and vaneless diffuser respectively. Similarly, ρ_2 and ρ_3 are the gas density at the outlet of impeller and vaneless diffuser respectively. The process of the formula derivation can be seen below.

In Figure 3.4, it shows velocity triangles at the inlet and exit of vaneless diffuser.

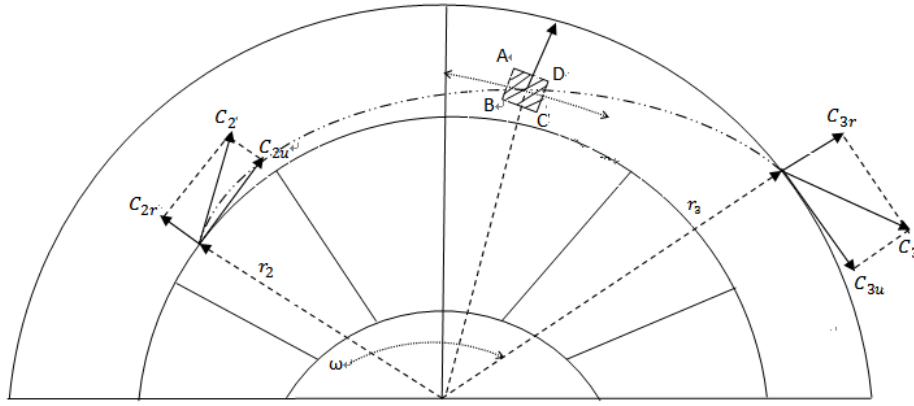


Figure 3.4 Flow inside the Vaneless diffuser [47]

The moment of momentum equation at the vaneless diffuser inlet and outlet can be written as

$$\Delta M = \Delta m (c_{2u}r_2 - c_{3u}r_3) \quad (3.2)$$

where ΔM is the torque acting on the gas element Δm . The flow inside the diffuser is symmetrical and so the pressure on the surface 'AB' and 'CD' is equal. When eliminating the friction force, only the centrifugal force acts on Δm , so the moment of force to spindle is zero.

$$c_{2u}r_2 = c_{3u}r_3 \quad (3.3)$$

According to the continuity equation, the change of radial velocity of gas c_r along with radius can be found. Ignoring choke at the outlet of the impeller, the mass flow rate through the vaneless diffuser can be written as

$$G_c = \rho_2 c_{2r} \pi D_2 b_2 = \rho_3 c_{3r} \pi D_3 b_3 \quad (3.4)$$

It is assumed that $b_2 \rho_2 = b_3 \rho_3$; Therefore, $c_{2r} D_2 = c_{3r} D_3$;

$$\frac{c_3}{c_2} = \frac{\sqrt{c_{3u}^2 + c_{3r}^2}}{\sqrt{c_{2u}^2 + c_{2r}^2}} = \frac{\sqrt{(c_{2u}^2 + c_{2r}^2) \left(\frac{D_2}{D_3}\right)^2}}{\sqrt{c_{2u}^2 + c_{2r}^2}} = \frac{D_2}{D_3} \quad (3.5)$$

3.1.4 The Vaned Diffuser

The vaned diffuser is usually used in turbochargers that require high pressure ratios and high efficiencies with lower flow ranges. They are more commonly found on larger compressors. Its overall diffusion rate is higher than vaneless diffuser with the same radius ratio. The tangential

component of velocity is reduced more quickly by reducing the surface friction and producing a high peak efficiency, which can be several percentage points above the vaneless diffuser efficiency over the same flow range. However, the optimised operating range will also be reduced. The reduced tangential velocity results in a shorter flow path and a more compact diffuser. This gives the vaned diffuser a greater advantage where more compact compressor designs are required.

3.1.5 The Volute

The volute after the diffuser is commonly used to direct the flow to the next component and pressure ratio is barely changed through the volute. In the turbocharger centrifugal compressor with a vaneless diffuser, the volute plays a significant role in determining the overall performance characteristic, yet a relatively small amount of research has taken place in volute design compared to impellers and diffusers [62].

3.2 Compressor Model Structure

3.2.1 Mathematic Description for the Centrifugal Compressor

A centrifugal compressor model is presented in this chapter. The model in this thesis is based on the first thermodynamics principle, i.e. where energy transfer is being taken into consideration including the losses determined from the compressor geometry and not from the experimentally determined characteristic performance curves. In this thesis, the different losses in each component of compressor are mathematically modelled for developing compressor characteristics. The losses can be analysed individually to produce improved thermodynamic compressor efficiency.

For convenience, the compressor is commonly divided into different parts with stations which are located at the inlets and exits of different parts. It can be divided into five stations, as demonstrated in Figure 3.5.

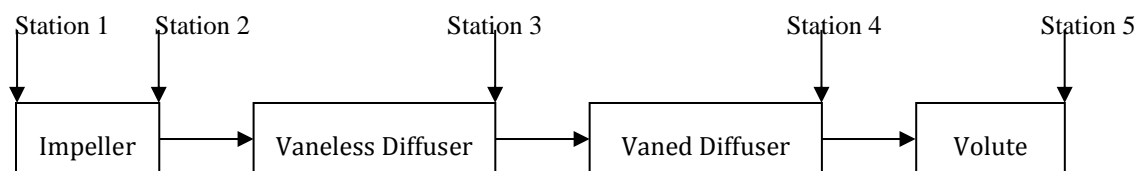


Figure 3.5 Compressor Component Division

Stations 1 and 2 are the impeller inlet and exit and station 2 is also the diffuser inlet. Station 3 is the vaneless diffuser exit and vaned diffuser inlet. Station 4 is the vaned diffuser exit and volute

inlet and station 5 is the volute exit.

The variables in the model associated with different stations will be inlet pressure, inlet temperature, inlet velocities, exit pressure, exit temperature, exit velocities. The following Figure 3.6 clearly shows the variables associate with each component in the centrifugal compressor.

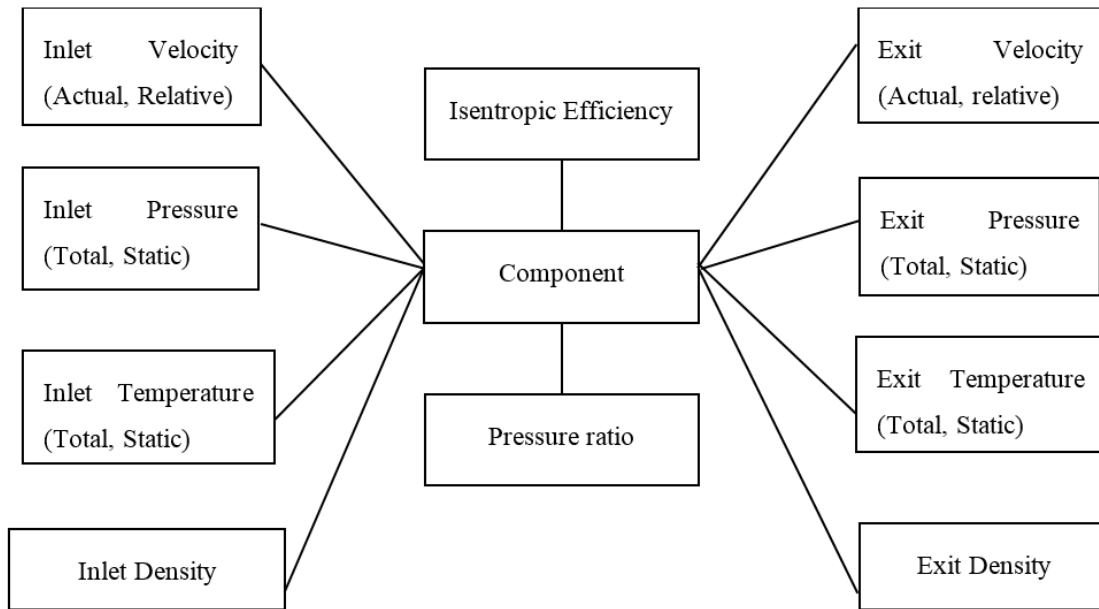


Figure 3.6 Variables used to describe each compressor component

3.2.2 Flow Chart for the Centrifugal Compressor Performance Prediction

Now that the centrifugal compressor has been mathematically described as above, a method is needed to simultaneously solve the extensive set of derived equations. Solving the equations by hand is possible, but Matlab has been used to solve the set of equations. The flow chart presented in Figure 3.7 shows the method of coupling the components of the centrifugal compressor together into one system. The calculation process can be clearly seen from the flow chart. It also can be seen that the centrifugal compressor model was composed of several sub models such as Impeller model, Vaneless diffuser model, Vaned diffuser model and volute model.

The program inputs are the ambient temperature and pressure, rotational speed, fluid mass flow rate, and compressor geometry. The geometry input into the system is the component diameters, component passage heights, component flow areas, impeller and vaned diffuser blade angles, impeller and vaned diffuser blade thicknesses, impeller and vaned diffuser blade quantities, impeller and shroud clearances, and material surface roughness.

The compressor calculation was starting from the compressor geometry and ambient conditions. The stations downstream are subsequently evaluated using upstream results and appropriate equations connecting the inlet and exit of each component. For the impeller, rothalpy (defined as the difference between the total enthalpy and angular momentum) remained constant across the component due to its rotating frame of reference, while the enthalpy remained constant across stationary components [43].

The general procedure is to first calculate the isentropic (ideal) conditions through the impeller. Second, the isentropic conditions are used to quantify the various losses that occur in the impeller. The last step is to transform the impeller exit conditions into meaningful parameters that can be compared to measured data. The impeller exit conditions are then used as inlet conditions to the vaneless diffuser. The vaneless diffuser leads to the vaned diffuser, which then leads to the compressor volute.

Since the impeller is rotating during operation, it is better to employ the rotating frame as the reference. The outputs of the proposed model are velocities, Mach number, temperatures, pressures and flow density for the impeller. Then those parameters can be used for similar calculations for the impeller throat. And the same method will be used for the isentropic exit. The throat information is saved and passed to the “isentropic exit” subroutine. In the “isentropic exit” subroutine, the thermodynamic process is assumed to be isentropic meaning that there are no losses considered. The isentropic process is regarded as ideal thermodynamic process for turbomachinery. The information is saved and passed to the losses subroutine and actual exit subroutine. Losses can be evaluated in the form of total pressure loss. The total pressure loss is then used in the “actual exit” subroutine to calculate the absolute parameters for the impeller exit which will be used for the modelling of the vaneless diffuser.

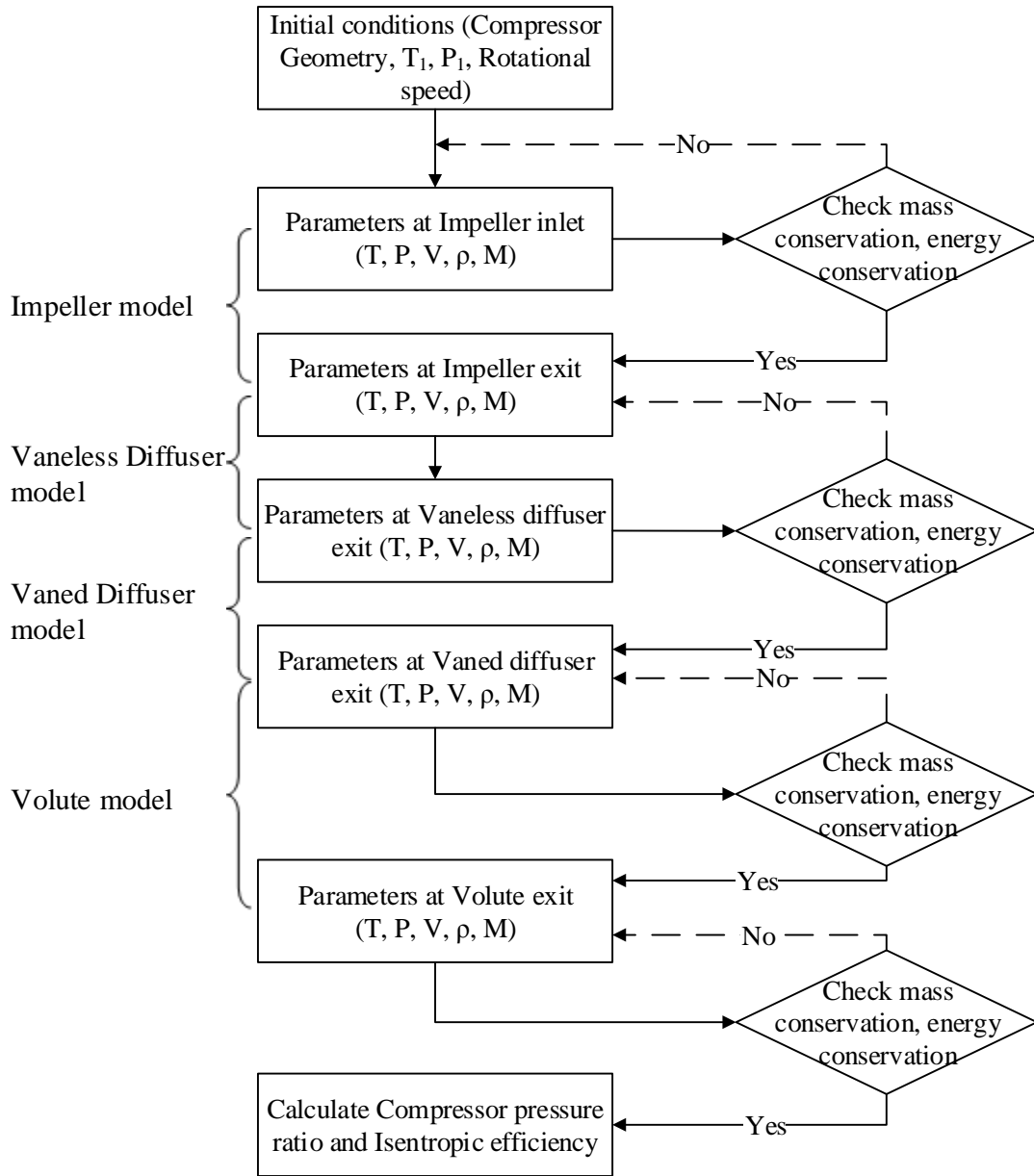


Figure 3.7 Flow Chart for the Compressor Performance Prediction

3.3 Centrifugal Compressor Model

3.3.1 The Impeller Inlet

The most important geometrical parameter of the impeller is the inlet annulus or cross-sectional area, A_1 , which is the narrowest point between the main blades. It can be defined as:

$$A_1 = \pi/4(D_{t1}^2 - D_{h1}^2) \quad (3.6)$$

Where D_{t1} and D_{h1} are the inducer tip and hub diameters respectively.

The mass flow rate \dot{m} and C_1 is given by

$$C_1 = \frac{\dot{m}}{\rho_{01} A_1}, \quad (3.7)$$

where ρ_{01} is the constant stagnation density at the inlet, C_1 is the absolute velocity at inlet and A_1 is the inlet area. The tangential velocity U_1 of the inducer with a diameter D_1 , can be calculated as

$$U_1 = \frac{D_1}{2} \omega = \frac{D_1 \pi N}{60}, \quad (3.8)$$

where ω is the impeller angular velocity and N is the rotational speed of the impeller. The average diameter D_1 is defined as

$$D_1^2 = \frac{1}{2}(D_{t1}^2 + D_{h1}^2) \quad (3.9)$$

where D_{t1} and D_{h1} are the tip diameter and hub diameter respectively.

From the velocity triangle in the figure explained earlier, the correlation between the velocities can be deduced.

$$C_{1r} = C_1 \sin \alpha_1 \quad (3.10)$$

where C_{1r} is the radial component of flow velocity at inlet and α_1 is the absolute flow angle.

$$(3.11)$$

$$C_{1u} = C_1 \cos \alpha_1$$

where C_{1u} is the tangential component of velocity at inlet

$$W_1 = \frac{C_{1r}}{\cos \beta_1} \quad (3.12)$$

where W_1 is the relative velocity at impeller inlet and β_1 is the blade angle at inlet.

The static temperature at impeller inlet can be calculated from the total temperature at the impeller inlet and the inlet velocity.

$$T_1 = T_{t1} \cdot \frac{C_{1r}^2}{2C_p} \quad (3.13)$$

The Mach number at impeller inlet can be calculated from the inlet velocity and the inlet temperature.

$$M_1 = \frac{C_{1r}}{\sqrt{\gamma R T_1}} \quad (3.14)$$

The inlet static pressure can be computed using compressible relationships [89]:

$$P_1 = P_{t1} / \left[1 + \left(\frac{\gamma-1}{2} \right) M_1^2 \right]^{\frac{\gamma}{\gamma-1}} \quad (3.15)$$

Using the ideal gas equation, the density can be computed using the inlet pressure and temperature:

$$\rho_1 = \frac{P_1}{R T_1} \quad (3.16)$$

3.3.2 The Impeller Throat

The impeller throat is defined as the location in the impeller with the smallest area and it is normally quite close to the inlet of the impeller. The flow condition around the throat can be determined by using the velocity triangle, correlations of pressure, temperature, density and interactions between inlet and exit.

The radial component of flow velocity at throat C_{aTh} can be calculated as

$$C_{rTh} \approx C_{1r} \quad (3.17)$$

where C_{1r} is the radial component of flow velocity at inlet [69].

The tangential component of flow velocity at throat C_{uTh} can be calculated as

$$C_{uTh} = U_{Th} - \frac{C_{rTh}}{\tan \beta_{Th}} \quad (3.18)$$

where U_{Th} is the tangential speed at throat, C_{rTh} is the radial component of flow velocity at blade throat, and β_{Th} is the blade angle at throat.

According to the velocity triangles, the absolute velocity at throat C_{Th} can be calculated as

$$C_{Th} = \sqrt{C_{uTh}^2 + C_{rTh}^2} \quad (3.19)$$

The tangential velocity U_{Th} of the impeller throat can be obtained as

$$U_{Th} = \frac{\pi N_c D_{th}}{60} \quad (3.20)$$

where N_c is the rotational speed of compressor and D_{th} is diameter at blade throat. The diameter at the impeller throat D_{th} can be calculated if the throat area is known.

$$D_{th} = \sqrt{\frac{4 \cdot A_{th}}{\pi}} \quad (3.21)$$

where A_{th} is the throat area. According to the velocity triangles, the impeller inlet relative velocity W_{Th} can be calculated as

$$W_{Th} = \sqrt{C_{Th}^2 + U_{Th}^2} \quad (3.22)$$

where C_{Th} is the absolute velocity at throat. The impeller throat static pressure P_{Th} can be calculated as

$$P_{Th} = \frac{P_{tTh}}{\left[1 + \left(\frac{\gamma-1}{2}\right) M_{Th}^2\right]^{\frac{\gamma}{\gamma-1}}} \quad (3.23)$$

where P_{tTh} is the total pressure at impeller throat. The flow density at impeller throat ρ_{Th} can be calculated as

$$\rho_{Th} = \frac{P_{Th}}{RT_{Th}} \quad (3.24)$$

The correlations between the inlet and exit can be expressed as

$$T_{tTh} = T_{t1} \cdot \left[\frac{2N\pi(C_{1u}r_{m1} - C_{uTh}r_{mTh})}{60C_p} \right] \quad (3.25)$$

where T_{tTh} is the total temperature at impeller throat. The static temperature at the impeller throat can be calculated as

$$T_{sTh} = \frac{T_{tTh}}{\left[1 + \left(\frac{\gamma-1}{2}\right) M_{Th}^2\right]^{\frac{\gamma}{\gamma-1}}} \quad (3.26)$$

where T_{tTh} is the total temperature at impeller throat and M_{th} is the Mach number at impeller throat. The total pressure at impeller throat can be calculated as

$$P_{tTh} = T_{t1} \left(\frac{T_{tTh}}{T_{t1}} \right)^{\frac{\gamma}{\gamma-1}} \quad (3.27)$$

3.3.3 The Impeller Exit

The gas leaves the impeller at the impeller tip with velocity C_2 . The impeller tip rotational speed U_2 and the relative velocity, W_2 ideally follows the direction of the blade and the absolute velocity C_2 completes the triangle. C_{a2} and $C_{\theta 2}$ are the radial and tangential components of the absolute velocity respectively.

The radial component of impeller outlet flow velocity C_{2r} is given by

$$C_{2r} = \frac{\dot{m}}{\rho_2 A_2}, \quad (3.28)$$

where ρ_2 is inlet density and A_2 is the impeller exit area. The tangential velocity U_2 , at diameter D_2 is calculated as

$$U_2 = \frac{D_2}{2} \omega = \frac{D_2 \pi N}{60} \quad (3.29)$$

where ω is the angular velocity of the impeller and N is the number of revolutions per minute. The radial component of impeller outlet flow velocity C_{2u} can be calculated as

$$C_{2u} = \sigma U_2 \quad (3.30)$$

where σ is the slip factor. The Relative flow velocity at impeller Outlet W_2 can be expressed as

$$W_2 = \frac{C_{2r}}{\cos \beta_2} \quad (3.31)$$

where β_2 is the the angle between the relative velocity and the tangential direction.

$$\beta_2 = \tan^{-1} \left(\frac{C_{2r}}{U_2 - C_{2u}} \right) \quad (3.32)$$

The angle between the absolute velocity and the tangential direction α_2 can be calculated as

$$\alpha_2 = \tan^{-1}\left(\frac{C_{2r}}{C_{2u}}\right) \quad (3.33)$$

The total temperature at impeller exit can be calculated as

$$T_{t2} = T_{t1} + \frac{\sigma \cdot U_2^2}{c_p} \quad (3.34)$$

The static temperature at impeller exit can be calculated from the total temperature at the impeller exit and the exit velocity.

$$T_2 = T_{t2} - \frac{C_2^2}{2c_p} \quad (3.35)$$

The Mach number at impeller exit can be calculated from the exit velocity and the exit temperature.

$$M_2 = \frac{C_2}{\sqrt{\gamma R T_2}} \quad (3.36)$$

The density can be computed using the impeller exit pressure and temperature.

$$\rho_2 = \frac{P_2}{R T_2} \quad (3.37)$$

The isentropic total pressure (ideal) at impeller exit can be calculated as

$$P_{t2} = \left(\frac{T_{t2}}{T_{t1}}\right)^{\frac{\gamma}{\gamma-1}} P_{t1} \quad (3.38)$$

The impeller exit static pressure can be obtained using compressible relationships [90]:

$$P_{2,ideal} = \frac{P_{t2}}{\left[1 + \left(\frac{\gamma-1}{2}\right) M_2^2\right]^{\frac{\gamma}{\gamma-1}}} \quad (3.39)$$

3.3.4 Losses in the Impeller

The impeller losses were determined in the rotating frame of reference in the form of a total relative pressure loss [91]:

$$\Delta P_{tr} = f_c (P_{tr1} - P_1) \sum_i K_i \quad (3.40)$$

where P_{tr1} is the total relative pressure at impeller inlet and P_1 is the static pressure at the impeller inlet. f_c is a correction factor defined as

$$f_c = \frac{\rho_{tr2} T_{tr2}}{\rho_{tr1} T_{tr1}} \quad (3.41)$$

where ρ_{tr} is the total relative density. ρ_{tr1} and ρ_{tr2} can be respectively calculated as

$$\rho_{tr1} = \frac{P_{tr1}}{RT_{tr1}} \quad (3.42)$$

$$\rho_{tr2} = \frac{P_{tr2}}{RT_{tr2}} \quad (3.43)$$

Then the correction factor f_c can be rearranged as

$$f_c = \frac{P_{tr2}}{P_{tr1}} \quad (3.44)$$

P_{tr1} and P_{tr2} can be respectively calculated as [91]:

$$P_{tr1} = P_{s1} \left[1 + \left(\frac{\gamma-1}{2} \right) M_{r1}^2 \right]^{\frac{\gamma}{\gamma-1}} \quad (3.45)$$

$$P_{tr2} = P_{s2} \left[1 + \left(\frac{\gamma-1}{2} \right) M_{r2}^2 \right]^{\frac{\gamma}{\gamma-1}} \quad (3.46)$$

The relative Mach number M_{r1} and M_{r2} can be obtained

$$M_{r2} = \frac{W_2}{a_2} \quad (3.47)$$

$$M_{r1} = \frac{W_1}{a_1} \quad (3.48)$$

where W_1 and W_2 are the relative velocity at the impeller inlet and exit respectively.

To obtain the loss in the impeller, the isentropic flow conditions have to be calculated first. Then the real flow conditions can be determined by adding the losses to the isentropic flow conditions. The non-isentropic conditions can be obtained by using conservation of rothalpy. Rothalpy is the difference between the total enthalpy and angular momentum which can be calculated by using the isentropic relative total temperature and the actual relative total temperature.

$$T_{tr,ideal} = T_{tr,actual} \quad (3.49)$$

The actual total relative pressure at the impeller exit is defined as

$$P_{tr2,actual} = P_{tr2,ideal} - \Delta P_{tr} \quad (3.50)$$

where $P_{tr2,ideal}$ can be calculated as

$$P_{tr2,ideal} = P_{2,ideal} \left[1 + \left(\frac{\gamma-1}{2} \right) M_{r2}^2 \right]^{\frac{\gamma}{\gamma-1}} \quad (3.51)$$

According to various researches about centrifugal compressor performance prediction, there are commonly 9 losses that could affect the performance of the impeller, which will be discussed in details as follows.

3.3.4.1 Calculation of Incidence Loss

Incidence loss is mainly caused by the flow incidence at different operating conditions:

$$K_{inc} = 0.8 \left[1 - \frac{C_{r1}}{W_1 \sin(\theta_{r1})} \right]^2 + \left[\frac{t_{b1} \cdot Z_{im}}{2 \cdot \pi \cdot r_1 \cdot \sin(\theta_{r1})} \right]^2 \quad (3.52)$$

where t_{b1} is the impeller inlet blade thickness, θ_{r1} is the inlet mean blade angle, Z_{im} is the impeller blade numbers.

3.3.4.2 Calculation of Clearance Loss

Clearance loss is caused by the mixing of the tip clearance flow and the main flow

$$K_{cl} = \frac{2\dot{m}_{cl}\Delta P_{cl}}{\dot{m}_{p1}W_1^2} \quad (3.53)$$

ΔP_{cl} is the pressure difference across the gap and it can be calculated as

$$\Delta P_{cl} = \frac{\dot{m}(r_2 C_{U2} - r_{m1} C_{U1})}{Z \cdot \bar{r} \cdot \bar{b} \cdot L} \quad (3.54)$$

where U_{cl} is the velocity of the leakage flow and \dot{m}_{cl} is the clearance gap leakage flow rate.

$$U_{cl} = 0.816 \sqrt{\frac{2\Delta P_{cl}}{\rho_2}} \quad (3.55)$$

$$\dot{m}_{cl} = \rho_2 \cdot Z \cdot \varepsilon \cdot L \cdot U_{cl} \quad (3.56)$$

where ε is the clearance gap width and L is the mean streamline meridional length.

$$\bar{r} = \frac{r_{m1} + r_2}{2} \quad (3.57)$$

$$\bar{b} = \frac{b_1 + b_2}{2} \quad (3.58)$$

3.3.4.3 Calculation of Entrance Diffusion Loss

Entrance diffusion loss is caused by the diffusion in the region between the blade inlet and the throat. The blade thickness at the inlet is an important factor for the characteristics of the diffusion. The entrance diffusion loss in impeller can be obtained as

$$K_{\text{diff}} = 0.8 \left[1 - \frac{W_{1\text{Th}}}{W_1} \right]^2 \bar{\omega}_{\text{inc}} \quad (\bar{\omega}_{\text{diff}} \geq 0) \quad (3.59)$$

3.3.4.4 Calculation of Skin Friction Loss

Skin friction loss or wall friction loss is caused by the flow viscosity at the solid surface that is

$$K_{\text{sf}} = 4C_f \left(\frac{\bar{W}}{W_1} \right)^2 \frac{L_B}{D_H} \quad (3.60)$$

$$\bar{W}^2 = \frac{(W_1^2 + W_2^2)}{2} \quad (3.61)$$

where L_B is the blade mean camberline length, D_H is the hydraulic diameter, b_2 is the impeller exit width, θ_2 is the discharge blade angle and Re_d is the Reynolds number.

$$D_H = \frac{\frac{\pi}{2} \cos(\theta_{m1})(D_{1\text{tip}}^2 - D_{1\text{hub}}^2)}{\pi \cdot \cos(\theta_{m1})(D_{1\text{tip}} + D_{1\text{hub}}) + 2 \cdot Z \cdot (D_{1\text{tip}} - D_{1\text{hub}})} + \frac{\pi D_2 b_2 \cos(\theta_2)}{\pi D_2 \cos(\theta_2) + Z \cdot b_2} \quad (3.62)$$

$$b_2 = \frac{A_2}{\pi D_2} \quad (3.63)$$

$$Re_d = \frac{\rho C D_H}{\mu} \quad (3.64)$$

For laminar conditions,

$$C_f = C_{f\ell} = \frac{16}{Re_d}; \quad (Re_d < 2000) \quad (3.65)$$

For turbulent flow over smooth surfaces,

$$\frac{1}{\sqrt{4C_{f\text{ts}}}} = -2 \log_{10} \left[\frac{2.51}{Re_d \sqrt{4C_{f\text{ts}}}} \right]; \quad (Re_d \geq 2000) \quad (3.66)$$

For turbulent flow over rough surfaces,

$$C_{f\text{tr}} = \frac{\left(\frac{1}{-2 \log_{10} \left[\frac{e}{3.71 D_H} \right]} \right)^2}{4} \quad (Re_d \geq 2000) \quad (3.67)$$

Surface roughness has to be considered when the following condition is met

$$Re_e = \frac{(Re_d - 2000) \cdot e}{D_H} > 60 \quad (3.68)$$

Thus, the friction coefficient for turbulent conditions

$$C_f = C_{ft} = C_{fts} ; (Re_e < 60) \quad (Re_d > 4000) \quad (3.69)$$

$$C_f = C_{ft} = C_{fts} + (C_{ftr} - C_{fts}) \left(1 - \frac{60}{Re_e}\right); (Re_e \geq 60) \quad (Re_d > 4000) \quad (3.70)$$

$$C_f = C_{fl} + (C_{ft} - C_{fl}) \left(\frac{Re_d}{2000} - 1\right); (2000 < Re_d < 4000) \quad (3.71)$$

3.3.4.5 Calculation of Choking Loss

Choking loss is caused by the flow with a Mach number higher than 1 which can be expressed as

$$K_{ch} = 0.5(0.05X + X^7) \quad (X > 0) \quad (3.72)$$

$$K_{ch} = 0; \quad (X < 0) \quad (3.73)$$

where X is constraint condition which can be calculated as

$$X = 11 - \frac{10 \cdot C_r \cdot A_{Th}}{A^*_{Th}} \quad (3.74)$$

where C_r is the contraction ratio and can be calculated as

$$C_r = \sqrt{\frac{A_1 \sin(\theta_{m1})}{A_{Th}}} \quad (3.75)$$

A^*_{Th} is the sonic flow throat area and can be mathematically described as

$$A^*_{Th} = \frac{\dot{m}}{a_{Th} \rho_{Th}} \quad (3.76)$$

$$a_{Th} = \sqrt{\gamma R T_{Th}} \quad (3.77)$$

3.3.4.6 Calculation of Blade Loading Loss

Blade loading loss is caused by negative pressure gradients on the blade which leads to separation or stall when the conditions is severe. The Blade loading loss can be defined as

$$K_{bl} = \frac{(\Delta W / W_1)^2}{24} \quad (3.78)$$

where ΔW is the average blade velocity difference which can be calculated as

$$\Delta W = \frac{2\pi D_2 U_2 I_B}{Z \cdot L_B} \quad (3.79)$$

I_B is the blade work coefficient which can be calculated as

$$I_B = \sigma \cdot (1 - \lambda \cdot \Phi_2 \cot(\theta_2)) - \frac{U_1 C_{U1}}{U_2^2} \quad (3.80)$$

where Φ_2 is the impeller exit flow coefficient and it can be calculated as

$$\Phi_2 = \frac{\dot{m}}{\rho_2 A_2 U_2} \quad (3.81)$$

λ is the tip distortion factor which can be calculated as

$$\lambda = \frac{1}{1 - B_2} \quad (3.82)$$

where B_2 is the tip blockage equation which can be calculated as

$$B_2 = \bar{\omega}_{sf} \frac{P_{v1}}{P_{v2}} \sqrt{\frac{W_1 D_H}{W_2 b_2}} + [0.3 + \frac{b_2^2}{L_B^2}] \frac{A_R^2 \rho_2 b_2}{\rho_1 L_B} + \frac{\varepsilon}{2b_2} \quad (3.83)$$

P_v is the velocity pressure which can be calculated as

$$P_v = P_t - P_s \quad (3.84)$$

A_R is the passage area ratio which can be calculated as

$$A_R = \frac{A_2 \sin(\theta_2)}{A_1 \sin(\theta_{1Th})} \quad (3.85)$$

3.3.4.7 Calculation of Hub to Shroud Loading Loss

Hub to shroud loading loss accounts is caused by the pressure gradient in the hub to shroud direction which is similar to the blade loading loss. Secondary flow can occur which could lead to stall eventually. This type of loss is defined as

$$K_{hs} = \frac{(\bar{k}_m \bar{b} \bar{W} / W_1)^2}{6} \quad (3.86)$$

where \bar{W} is the average relative velocity and it can be calculated as

$$\bar{W} = \frac{W_1 + W_2}{2} \quad (3.87)$$

\bar{k}_m is the passage curvature which can be calculated as

$$\bar{k}_m = \frac{\alpha_{C2} - \alpha_{C1}}{L} \quad (3.88)$$

α_{C1} and α_{C2} are the hub cone angle at the inlet and the exit respectively.

3.3.4.8 Calculation of Blockage Loss

The flow in converging nozzles will be speeded up in the flow direction and the fluid is turned along the camber line in the meridional direction. This causes the growth of boundary layers with loss of kinetic energy and blockage. Blockage loss is caused by the flow separation and recirculation with negative pressure gradients. The expansion loss in the rotor can be calculated as

$$K_{\text{block}} = \left[\frac{(\lambda - 1)C_{r2}}{W_1} \right]^2 \quad (3.89)$$

where λ is the tip distortion factor and it can be calculated as

$$\lambda = \frac{1}{1 - B_2} \quad (3.90)$$

B_2 is the tip blockage and it can be calculated as

$$B_2 = \frac{[K_1 + K_2(\bar{C}_R^2 - 1)]L_B}{w_2} \quad (3.91)$$

where w is the blade-to-blade width and it can be calculated as

$$w = \frac{2\pi r \sin(\theta_2)}{Z} \quad (3.92)$$

\bar{C}_R , K_1 , K_2 are the blockage correlations and they can be calculated as

$$\bar{C}_R = \frac{1}{2} \left[\frac{C_{r2} \sin(\theta_2)}{C_{r1} \sin(\theta_1)} + 1 \right] \quad (3.93)$$

$$K_1 = 0.2 \left[1 - \frac{1}{C_L C_\theta} \right] \quad (3.94)$$

$$K_2 = \frac{2\theta_c}{125 C_\theta} \left[1 - \frac{2\theta_c}{22 C_\theta} \right] \quad (3.95)$$

θ_c is the diffuser divergence angle and it can be calculated as

$$2\theta_c = 2\tan^{-1}\left[\frac{(w_2 - t_{b2})\frac{b_2}{b_1} - w_2 + t_{b2}}{2L_B}\right] \quad (3.96)$$

where L is the mean streamline length of vaned diffuser and it can be calculated as

$$L = \frac{\Delta C}{C_2 - C_1} \quad (3.97)$$

ΔC is the average blade-to-blade velocity difference and it can be calculated as

$$\Delta C = 2\pi \frac{r_2 C_{U2} - r_1 C_{U1}}{ZL_B} \quad (3.98)$$

3.3.4.9 Calculation of Mixing Loss

Mixing loss is caused by the mixing of wake flow and the main stream flow which can be calculated as

$$K_{\text{mix}} = \left[\frac{C_{r,\text{wake}} - C_{r,\text{mix}}}{W_1} \right]^2 \quad (3.99)$$

where $C_{m,\text{wake}}$ is the radial component of wake velocity in the nozzles.

$$C_{r,\text{wake}} = \sqrt{W_{\text{Sep}}^2 - W_2^2} \quad (3.100)$$

$C_{r,\text{mix}}$ is the radial component of mixing flow velocity in the nozzles.

$$C_{r,\text{mix}} = \frac{C_{r2} A_2}{\pi D_2 b_2} \quad (3.101)$$

$$W_{\text{Sep}} = W_2; (D_{\text{eq}} \leq 2) \quad (3.102)$$

$$W_{\text{Sep}} = \frac{W_2 D_{\text{eq}}}{2}; (D_{\text{eq}} > 2) \quad (3.103)$$

where D_{eq} is the equivalent diffusion ratio and it can be calculated as

$$D_{\text{eq}} = \frac{W_{\text{max}}}{W_2} \quad (3.104)$$

$$W_{\text{max}} = \frac{W_1 + W_2 + \Delta W}{2} \quad (3.105)$$

The actual flow conditions are obtained by combining the flow at isentropic status and the loss models. The average efficiency and power balance of each component can be obtained using the actual flow conditions at the exit. The actual total pressure is the difference between the ideal total

pressure and the actual total pressure loss.

$$P_{t2,actual} = P_{t2,ideal} - \Delta P_{t2} \quad (3.106)$$

The actual total pressure is used to calculate actual flow conditions at the exit of the volute using assuming that enthalpy is not changing and so does the total temperature. Then again those parameters can be used to determine the mean efficiency and the power output.

3.3.5 The Vaneless Diffuser

The vaneless diffuser is a device in the shape of an annular channel which is commonly used to convert the flow velocity to static pressure. It is known that $T_{t3} = T_{t2}$ due to the assumption that enthalpy is conserved.

$$P_{t3} = \left(\frac{T_{t3}}{T_{t2}} \right)^{\frac{\gamma}{\gamma-1}} P_{t2} \quad (3.107)$$

Similar to the impeller, the static temperature at vaneless diffuser exit can be calculated from the total temperature and the inlet velocity.

$$T_3 = T_{t3} - \frac{C_3^2}{2C_p} \quad (3.108)$$

The Mach number at vaneless diffuser exit can be calculated from the velocity and the static temperature.

$$M_3 = \frac{C_3}{\sqrt{\gamma R T_3}} \quad (3.109)$$

The vaneless diffuser exit static pressure can be obtained using correlations for compressible flow and are defined as

$$P_3 = \frac{P_{t3}}{\left[1 + \left(\frac{\gamma-1}{2} \right) M_3^2 \right]^{\frac{\gamma}{\gamma-1}}} \quad (3.110)$$

The density can be computed using the pressure and temperature.

$$\rho_3 = \frac{P_3}{R T_3} \quad (3.111)$$

The radial component of flow velocity at the vaneless diffuser exit can be calculated as

$$C_{3r} = \frac{m}{A_3 \rho_3} \quad (3.112)$$

then the tangential component of flow velocity at the vaneless diffuser exit can be calculated as

$$C_{3u} = \sqrt{C_3^2 - C_{3r}^2} \quad (3.113)$$

The loss in the vaneless diffuser can be expressed by using the total pressure loss across it which is defined as

$$\Delta P_{t3} = (P_{t2} - P_2) \sum_i K_i \quad (3.114)$$

The flow conditions are the same at both the inlet of the exit of the impeller and the vaneless diffuser.

3.3.6 Losses in Vaneless Diffuser

There are two losses in the vaneless diffuser described by Serrano [95].

3.3.6.1 Calculation of Skin Friction Loss

Skin friction loss is caused by the viscosity of the flow and can be calculated as

$$K_{sf} = 4C_f \left(\frac{\bar{C}}{C_2} \right)^2 \frac{(r_3 - r_2)}{D_{hyd}} \quad (3.115)$$

where D_{hyd} is the hydraulic diameter and C_f is the skin friction coefficient.

\bar{C} is the average velocity in the vaneless diffuser and it can be calculated as

$$\bar{C}^2 = \frac{(C_2^2 + C_3^2)}{2} \quad (3.116)$$

3.3.6.2 Calculation of Diffusion Loss

Diffusion loss can be used to evaluate the performance of the diffuser which is significantly affected by the inlet diameter of the diffuser. The entrance diffusion loss in vaneless diffuser can be modelled as

$$K_{df} = -2(1-E) \left(\frac{C_{3,ld} - C_2}{\rho_2 C_2} \right) \quad (3.117)$$

where E is the diffusion efficiency and it has a boundary condition that that is mathematically

described as:

$$E=1 \quad D \leq 0 \quad (3.118)$$

$$E=1-0.2\left(\frac{D}{D_m}\right)^2 \quad 0 < D < D_m \quad (3.119)$$

$$E=0.8\sqrt{\frac{D_m}{D}}, \quad D \geq D_m \quad (3.120)$$

D is the divergence parameter and it can be calculated as

$$D = \frac{b_2 \left(\frac{A_3}{A_2} - 1 \right)}{L} \quad (3.121)$$

$$D_m = 0.4 \left(\frac{b_2}{L} \right)^{0.35} \quad (3.122)$$

As discussed before, the actual flow conditions can be obtained by combining the flow at isentropic conditions with proper loss models. The actual total pressure is expressed as

$$P_{t3,actual} = P_{t3,ideal} - \Delta P_{t3} \quad (3.123)$$

The actual total pressure is used to calculate actual flow conditions at the exit of the volute using assuming that enthalpy is not changing and so does the total temperature. Then again those parameters can be used to determine the mean efficiency and the power output.

3.3.7 Calculation of Vaned Diffuser

For the vaneless diffuser and vaned diffuser with the same radius ratio, diffusion is higher in the former device. The total temperature at the vaned diffuser exit can be assumed as the same as the total temperature at the vaned diffuser inlet due to the assumption that enthalpy in the vaned diffuser is conserved.

$$T_{t4} = T_{t3} \quad (3.124)$$

then the static temperature at the vaned diffuser exit can be calculated as

$$T_4 = T_{t4} - \frac{C_4^2}{2C_p} \quad (3.125)$$

where C_4 is the flow velocity at the vaned diffuser exit and it can be calculated as

$$C_4 = C_3 \frac{b_3 D_3 \sin \alpha_3}{b_4 D_4 \sin \alpha_4} \left(\frac{T_3}{T_4} \right)^{\frac{1}{\gamma-1}} \quad (3.126)$$

where it is assumed $b_4=b_3$ and $\alpha_4=\alpha_3+\frac{15}{180\pi}$.

Similar to other components, the radial component of flow velocity at the vaned diffuser exit can be calculated as

$$C_{4r} = \frac{m}{A_4 \rho_4} \quad (3.127)$$

then the tangential component of flow velocity at the vaned diffuser exit can be calculated as

$$C_{4u} = \sqrt{C_4^2 - C_{4r}^2} \quad (3.128)$$

The Mach number at vaned diffuser exit can be calculated from the velocity and the static temperature.

$$M_4 = \frac{C_4}{\sqrt{\gamma R T_4}} \quad (3.129)$$

The vaned diffuser exit total pressure and static temperature can be computed as

$$P_{t4} = \left(\frac{T_{t4}}{T_{t3}} \right)^{\frac{\gamma}{\gamma-1}} P_{t3} \quad (3.130)$$

$$P_4 = P_3 \left(\frac{T_4}{T_3} \right)^{\frac{\gamma}{\gamma-1}} \quad (3.131)$$

The density can be computed using the pressure and temperature.

$$\rho_4 = \frac{P_4}{R T_4} \quad (3.132)$$

Similar to the vaneless diffuser, the loss in the vaned diffuser can be represented by using the total pressure loss across it as shown in the following:

$$\Delta P_{t4} = (P_{t3} - P_3) \sum_i K_i \quad (3.133)$$

The inputs required to determine the loss are flow parameters at the inlet, throat and exit assuming isentropic condition. The flow conditions are the same at both the inlet of the vaned diffuser and

the exit of the vaneless diffuser.

3.3.8 Losses in Vaned Diffuser

There are five non-dimensional vaned diffuser losses described in the model.

3.3.8.1 Calculation of Skin Friction Loss

Skin friction loss is the loss generating from the fluid flowing over the wall, which is also known as wall friction. The skin friction loss in vaned diffuser can be modelled as

$$K_{sf} = 4C_f \left(\frac{\bar{C}}{C_3} \right)^2 \frac{L_B/D_H}{(2\delta/D_H)^{0.25}} \quad (3.134)$$

where $\frac{2\delta}{D_H}$ is the boundary layer approximation and it can be calculated as

$$\frac{2\delta}{D_H} = \frac{5.142C_f L_B}{D_H} \quad (3.135)$$

C_f is the skin friction coefficient influenced by the surface roughness.

3.3.8.2 Calculation of Incidence Loss

Incidence loss accounts for the flow adjustment of the actual fluid flow to the blade angle at the inlet of the vaned diffuser. The incidence loss in the rotor can be calculated as

$$K_{inc} = 0.8 \left(\frac{C_3 - C_3^*}{C_3} \right)^2; \quad C_3 \leq C_{3s} \quad (3.136)$$

$$K_{inc} = 0.8 \left[\left(\frac{C_3}{C_{3s}} \right)^2 - 1 \right] \frac{C_{3s}^2}{C_3^2} + \frac{C_{3s} - C_3^*}{C_{3s}^2}; \quad C_3 > C_{3s} \quad (3.137)$$

where C_{3s} is the absolute stall velocity and it can be calculated as

$$C_{3s} = \frac{C_{m3}}{\sin \alpha_{3s}} \quad (3.138)$$

C_3^* is the velocity at the optimum incidence angle and it can be calculated as

$$C_3^* = \frac{C_{m3}}{\sqrt{\sin(\beta_3) \sin(\alpha_{Th})}} \quad (3.139)$$

where α_{Th} is the flow angle at the throat.

3.3.8.3 Calculation of Choking Loss

Choking loss accounts for the Mach number at the throat approaching 1. The choking loss in the vaned diffuser can be modelled as

$$K_{ch} = \frac{1}{2} (0.05X + X^7) \quad (3.140)$$

where X is the constraint condition and it can be expressed as

$$X = 11 - \frac{10C_r A_{Th3}}{A^*} \quad (3.141)$$

A^* is at sonic condition and it can be calculated as

$$A^* = \frac{m}{a_4^* \rho_4} \quad (3.142)$$

C_r is the contraction ratio and it can be calculated as

$$C_r = \sqrt{\frac{A_3 \sin(\theta_3)}{A_{Th3}}} \quad (3.143)$$

where θ_3 is the vaned diffuser Inlet blade angle.

3.3.8.4 Calculation of Mixing Loss

Mixing loss can be defined as

$$K_{mix} = \left[\frac{C_{m,wake} - C_{m,mix}}{C_3} \right]^2 \quad (3.144)$$

where $C_{m,wake}$ is the radial component of wake velocity in the vaned diffuser.

$$C_{m,wake} = \sqrt{C_{sep}^2 - C_{U4}^2} \quad (3.145)$$

$C_{r,mix}$ is the radial component of mixing flow velocity in the nozzles.

$$C_{r,mix} = \frac{A_4 C_{r4}}{2\pi r_4 b_4} \quad (3.146)$$

The actual total pressure is calculated using the following equation:

$$P_{t4,actual} = P_{t4,ideal} - \Delta P_{t4} \quad (3.147)$$

Then the same procedure is applied for the efficiency and power output as discussed previously.

3.3.9 The Volute

Pressure does not change much in the volute and volute is commonly used to direct flow. The total temperature at the volute exit can be assumed as the same as the total temperature at the volute inlet due to the assumption that enthalpy in the volute is conserved.

$$T_{t5} = T_{t4} \quad (3.148)$$

then the static temperature at the volute exit can be calculated as

$$T_5 = T_{t5} - \frac{C_5^2}{2C_p} \quad (3.149)$$

where C_5 is the flow velocity at the volute exit and it can be calculated as

$$C_5 = \sqrt{C_{5u}^2 + C_{5r}^2} \quad (3.150)$$

C_{5r} is the radial component of flow velocity at the volute exit can be calculated as

$$C_{5r} = \frac{\dot{m}}{A_5 \rho_5} \quad (3.151)$$

C_{5u} is the tangential component of flow velocity at the volute exit can be calculated as

$$C_{4u} r_4 = C_{5u} r_5 \quad (3.152)$$

The Mach number at volute exit can be calculated from the velocity and the static temperature.

$$M_5 = \frac{C_5}{\sqrt{\gamma R T_5}} \quad (3.153)$$

The volute exit total pressure and static temperature can be computed as

$$P_{t5} = \left(\frac{T_{t5}}{T_{t4}} \right)^{\frac{\gamma}{\gamma-1}} P_{t4} \quad (3.154)$$

$$P_5 = P_4 \left(\frac{T_5}{T_4} \right)^{\frac{\gamma}{\gamma-1}} \quad (3.155)$$

The density can be computed using the pressure and temperature.

$$\rho_5 = \frac{P_5}{RT_5} \quad (3.156)$$

The volute is the last component in centrifugal compressors. The loss inside the volute can be defined as its total pressure loss as

$$\Delta P_{t5} = (P_{t4} - P_4) \sum_i K_i \quad (3.157)$$

The exit flow conditions of the vaned diffuser can be used as the inlet condition for the volute.

3.3.10 Losses in the Volute

The volute has two non-dimensional losses will be discussed below.

3.3.10.1 Calculation of Skin Friction Loss

Skin friction loss is the loss generating from the fluid flowing over the wall, which is also known as wall friction. The skin friction loss in the exhaust diffuser can be calculated as

$$K_{sf} = 4C_f \left(\frac{C_5}{C_4}\right)^2 \frac{L}{D_H} \quad (3.158)$$

where L is the mean stream line path length of volute and it can be calculated as

$$L = \frac{\pi(r_4 + r_5)}{2} \quad (3.159)$$

D_H is the hydraulic diameter of volute and it can be calculated as

$$D_H = \sqrt{\frac{4A_5}{\pi}} \quad (3.160)$$

3.3.10.2 Calculation of Kinetic Energy Loss

The kinetic energy associated to the exit condition is then considered as wasted, because it can be anymore recovered. The kinetic loss at the volute is expressed as:

$$K_{ke} = \frac{1}{2} C_5^2 \quad (3.161)$$

3.3.10.3 Calculation of Skin Friction Loss

The isentropic solution is used in conjunction with the loss models to evaluate the non-isentropic or actual conditions. The actual exit conditions can be used to determine the component mean

thermodynamic efficiency and power consumption parameters. The actual total pressure is the difference of the ideal total pressure and the total pressure loss.

$$P_{t5,actual} = P_{t5,ideal} - \Delta P_{t5} \quad (3.162)$$

Then the same procedure is applied to obtain the mean thermodynamics efficiency and power output.

3.4 Calculation of Centrifugal Compressor Performance Map

3.4.1 Calculation of Centrifugal Compressor Pressure Ratio

The pressure ratio of each compressor component can be easily determined when the total and static pressures are known.

The pressure ratio in the impeller can be calculated as

$$PR_2 = P_2 / P_1 \quad (3.163)$$

The pressure ratio in the vaneless diffuser can be calculated as

$$PR_3 = P_3 / P_2 \quad (3.164)$$

The pressure ratio in the vaned diffuser can be calculated as

$$PR_4 = P_4 / P_3 \quad (3.165)$$

The pressure ratio in the vaneless diffuser can be calculated as

$$PR_5 = P_5 / P_4 \quad (3.166)$$

Finally, the entire compressor pressure ratio can be calculated from the pressure at the exit and at the inlet.

$$PR = P_5 / P_1 \quad (3.167)$$

3.4.2 Calculation of Centrifugal Compressor Isentropic Efficiency

The isentropic process refers to an idealised thermodynamic process that is adiabatic and reversible. In this idealised process, the work transfers are assumed frictionless, and there is no heat transfer.

The thermodynamic process in centrifugal compressor is far from isentropic process, however the isentropic process is useful to be the basis of comparison for real process happened in centrifugal compressor.

The isentropic efficiency of centrifugal compressor is a parameter to measure the level of degradation of energy. This parameter is used to compare the actual performance of centrifugal compressor and the idealised performance if assumed the thermodynamic process in centrifugal compressor is isentropic. The isentropic efficiency of each compressor component is a function of total pressure and total temperature at compressor component inlet and exit and can be mathematically described as [98]:

$$\eta = \frac{\left(\frac{P_{t,out}}{P_{t,in}}\right)^{\frac{\gamma-1}{\gamma}} - 1}{\left(\frac{T_{t,out}}{T_{t,in}}\right) - 1} \quad (3.168)$$

where is $P_{t,out}$ is total pressure at component exit, $P_{t,in}$ is total pressure at component inlet, $T_{t,out}$ is total temperature at component exit, and $T_{t,in}$ is total temperature at component inlet.

3.5 Summary

In this chapter, a compressor model has been developed by analysing the thermodynamics status and aerodynamic behaviour of the whole compressor system. Those include the flow governing equations such as the ideal gas correlations, mass conservation, energy conservation and velocity triangles based on the operating condition.

As a centrifugal compressor is commonly consisted of four main parts which are the impeller, vaneless diffuser, vaned diffuser, and the volute, it is practical and useful to analyse each of those components individually in order to obtain the whole compressor performance characteristics.

To make the prediction more realistic, loss models have also been applied to each components. The construction of the loss model is obtained by analysing the possible types of losses in each component, finding the dominate losses and etc. Each type of loss can be commonly defined using the appropriate pressure drop across the relevant component. Therefore, the component performance can be estimated by coupling the flow governing equations and the loss models with required input data. With all the key flow parameter known for all components, the overall performance of the whole compressor system can be predicted using the inlet and outlet flow conditions. That overall performance is generally presented in the form of mass flow rate against

pressure ratio and isentropic efficiency.

Chapter 4 Compressor Model Validation

4.1 Model Validation with Experimental Work

The model developed in Chapter 3 has been applied, and this one dimensional (1D) compressor model will be an analysis tool to a centrifugal compressor. Meanwhile, experimental work has been undertaken to validate the 1-D compressor model. The purpose of experimental work is to obtain the characteristic map of compressor and turbine that can be used to validate the capability and accuracy of the proposed 1D compressor model.

4.1.1 Experimental Test Rig

Validation tests were carried out on a 2.0 L diesel engine testbed. The engine was fitted with a turbocharger and the Geometry data of the tested centrifugal compressor are listed in Table 4.1. Experimental data has been collected with the turbocharger working at four different shaft speeds which were spread in its whole operating range: 90K rpm, 130K rpm, 170K rpm and 210K rpm. In this chapter, results from the numerical analysis and the comparison with the experimental data will be discussed in detail.

4.1.2 Validation Results and Discussion

As shown in Figure 4.1, comparison between simulation results and experimental data has been given at a rotational speed of 90K rpm, 130K rpm, 170K rpm, and 210K rpm. All the characteristic curves have good agreement with the experiment data including the trend. For all different shaft speeds tested, pressure ratio decreases while mass flow rate increases after a certain amount. With higher rotational speed, both simulation and experiment gives higher pressure ratio. This model also predicts surge point in good accuracy.

Table 4.1 The operating conditions and compressor geometry data

Parameter	Value
Inlet Static Temperature (K)	293
Inlet Static Pressure (kPa)	101.3
Impeller Inlet Tip Diameter (m)	0.049
Impeller Inlet Hub Diameter (m)	0.033
Impeller Inlet Blade Thickness (m)	0.0037
Impeller Blade inlet angle (°)	45
Impeller Throat Mean Blade Angle (°)	49.023
Impeller Exit Blade Angle (°)	26.238
Vaned diffuser inlet diameter (m)	0.092
Vaned diffuser exit diameter (m)	0.107
Vaned diffuser exit Blade Angle (°)	46.272
Volute inlet diameter (m)	0.107
Volute exit diameter (m)	0.131

Compressor surge was experimentally predicted with the sign of dramatic vibrations by reducing the mass flow. It was assumed that surge would be predicted numerically after the peak pressure ratio, i.e. when the slope of the characteristic curve becomes negative. Surge would commonly predicted from the numerical model when the mass flow is beyond the minimum value the compressor can cope with and it also agreed with the experimental data. It can be seen that speed lines go up from starting point and then goes down until the flow is choked. All surge points on different speed lines match experimental data in acceptable accuracy.

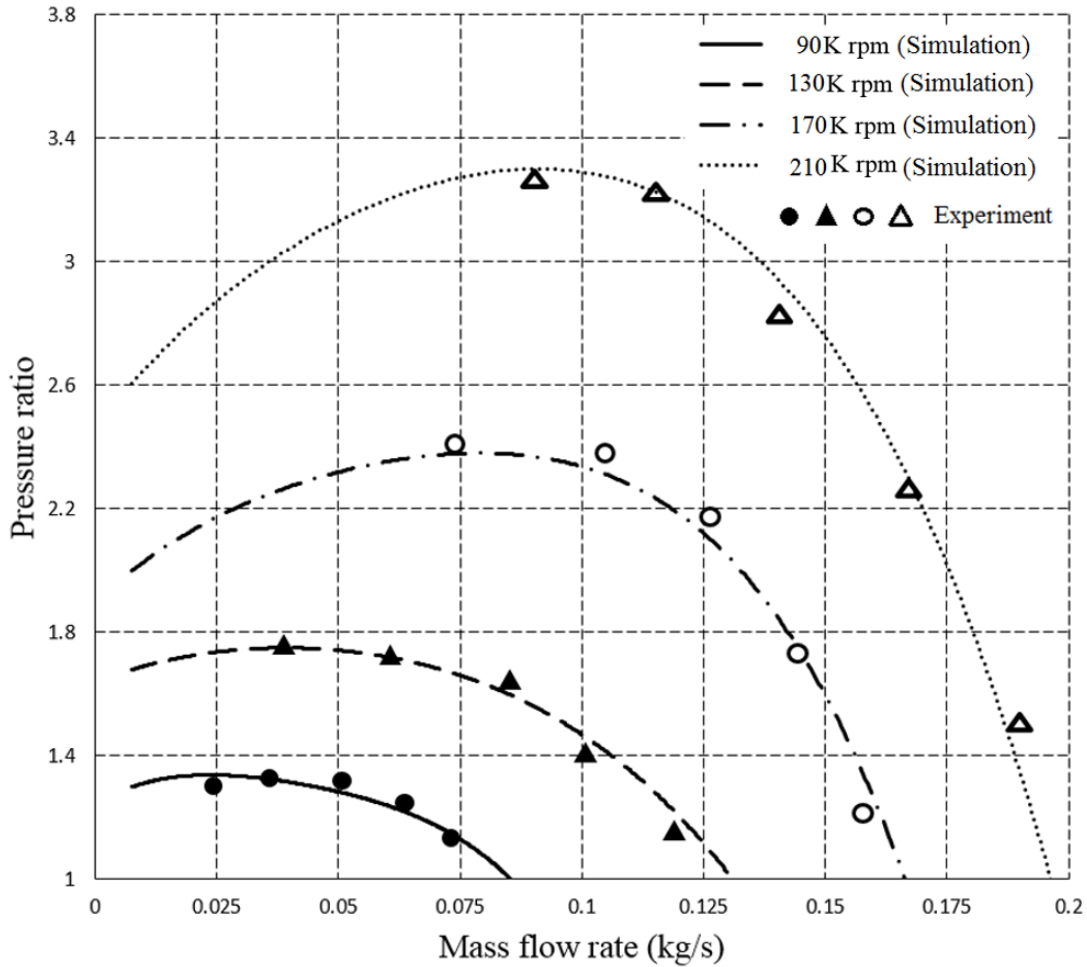


Figure 4.1 Validation of compressor pressure ratio with experimental data

As mentioned in chapter 3, compressor isentropic efficiency is very important for measuring the level of utilisation of available energy. The predicted isentropic efficiency has been validated against experimental data at all four rotational speeds investigated. The comparison between simulation and experiment can be seen in Figure 4.2. All speed lines show good agreement with experimental results. In experimental results, compressor isentropic efficiency goes up towards lower mass flow rate, and reach its peak value around the mid-range. Simulation results also show this trend for all different speed lines. With increasing rotational speed, efficiency line shift toward higher mass flow rate. Both simulation and experiment shows this phenomenon. It also can be seen the optimum efficiency happens at mid-range of rotational speed, i.e. the rotational speed between 130Krpm and 170Krpm.

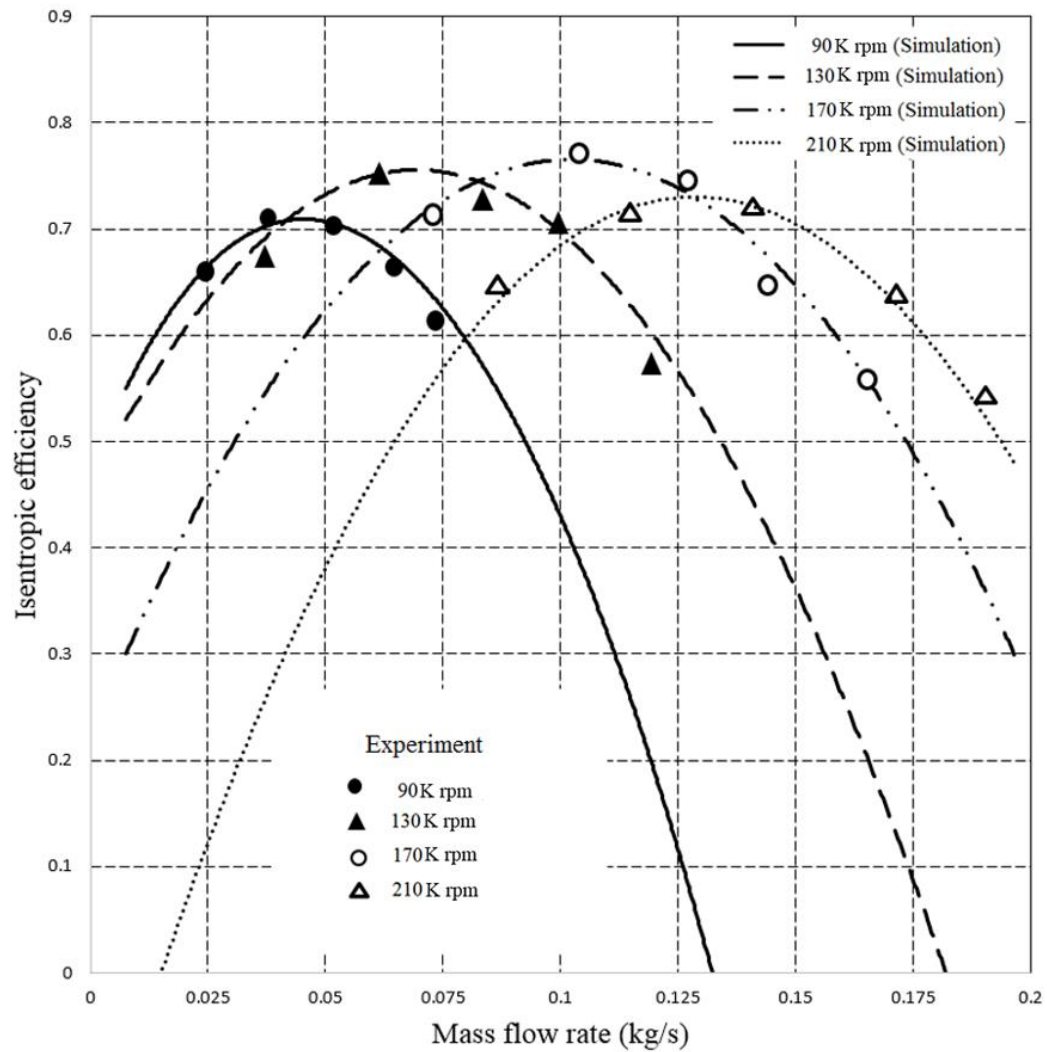


Figure 4.2 Validation of compressor efficiency with experimental data

With the proposed model, losses in centrifugal compressor can be estimated without expensive experiment. As flow details in each component and loss mechanism are the interest in this research, to get a better understanding of the flow can help designer to optimise geometry design and reduce losses in centrifugal compressor and improve compressor performance. It will be also helpful to work out the most efficient scenario at different working condition. In the rest of this chapter, the effect of loss mechanism on centrifugal compressor performance and flow details in each component will be discussed. The effect of compressor geometry on flow triangles will be also examined to provide better understanding of flow in compressors. To investigate the effect of geometrical settings for the compressor which can be applied for generic turbochargers, all the parameters presented were non-dimensionalised. For instance, different losses considered in the investigation were plotted against non-dimensional mass flow rate (referring to the maximum value

of flow rate at each compressor rotational speed).

4.2 Effect of Loss Mechanism on Compressor Performance

By examining the impact of loss mechanism on compressor performance, it is helpful to determine that the dominant loss in each component of centrifugal compressors. Reducing its main losses and therefore reducing costs can significantly improve compressor performance. As shown in Figure 4.3, all losses in a centrifugal compressor are plotted in one graph. It is clearly shown that the effect of different losses on the pressure ratio.

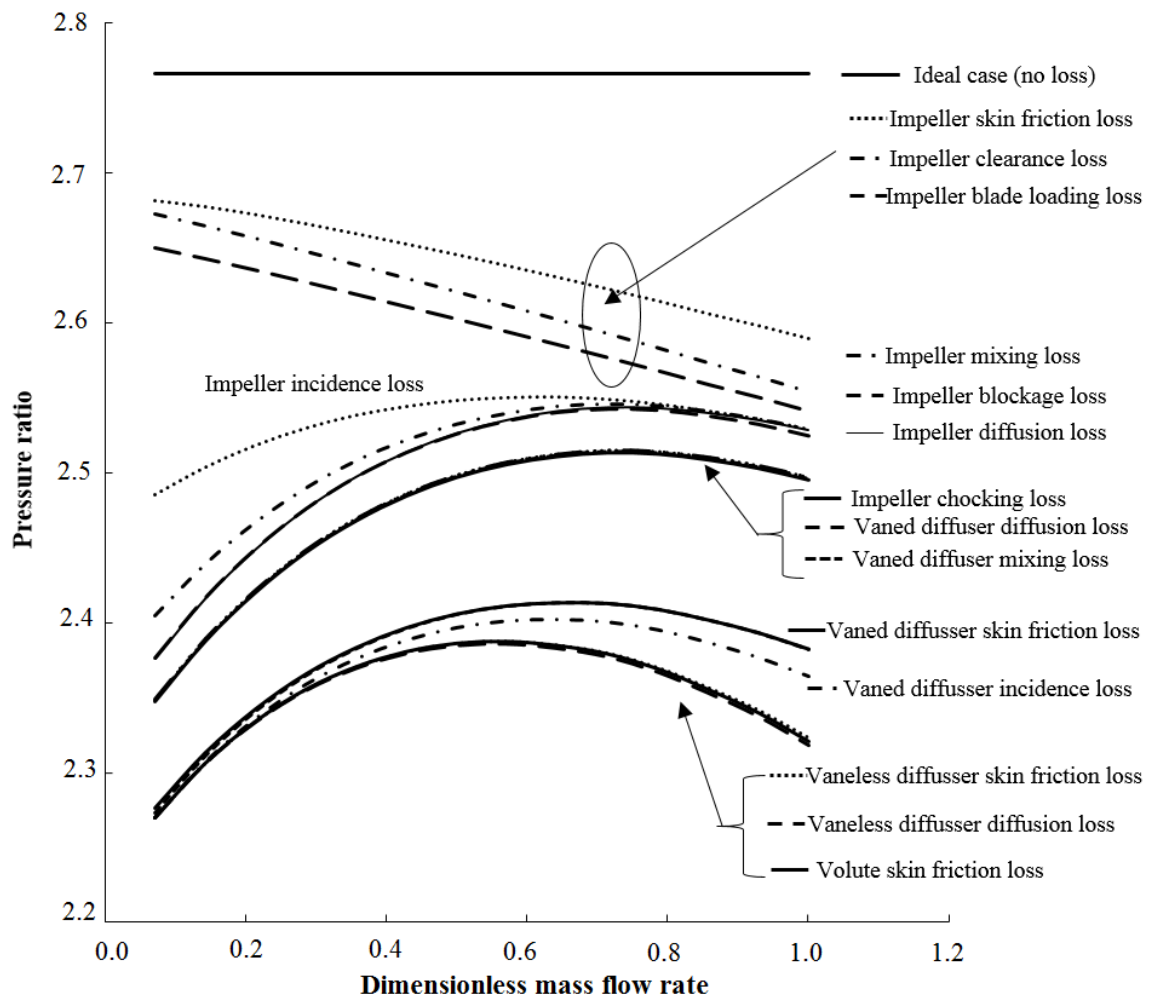


Figure 4.3 Effects of different losses on compressor performance ($N = 170K$ rpm)

Figure 4.3 shows ideal pressure ratio without any losses and the effect of different types of losses on compressor performance. It can be seen from the figure that:

- Without considering any loss (top solid line), pressure ratio should keep constant at a given rotational speed with different mass flow conditions.

- It can be found dominating losses that have significant effect on the shape of the compressor characteristics. It can be seen that the dominant losses in centrifugal compressors are commonly the impeller incidence loss, impeller skin friction loss and vaned diffuser skin friction loss.
- The shape of the performance characteristics is significantly affected by the impeller incidence loss.
- Although losses such as impeller clearance loss, impeller blade loading loss, vaned diffuser incidence loss and blockage loss for vaned diffusers have affect the performance characteristic less than the dominant losses, they still have to be taken into account.
- Losses in the volute do not have noticeable effects on the compressor performance and volute does help with the pressure recovery in the compressor system.

4.3 Pressure Build-up in Each Compressor Component

The compressor model demonstrated in the previous chapter can be also used to predict the pressure building up process in each component of the centrifugal compressor. In Figure 4.4, it shows the effect of different components on the overall performance of the compressor.

Figure 4.4 presents the numerically predicted performance characteristic of the compressor in term of pressure ratio against non-dimensionless mass flow rate with a rotational speed of 170K rpm. It is useful to understand the component performance of the whole centrifugal compressor. It can be concluded from the figure that:

- In all components, impeller is the device for most of the pressure increase.
- Vaned diffuser also contribute considerable pressure increase, compared with other components except impeller.
- It is proved that vaneless diffuser contribute less when work with vaned diffuser.
- It is clear to find that volute contribute little to the pressure recovery in the whole compressor system, which also proves that the volute is used for directing air flow rather than improve compressor performance.

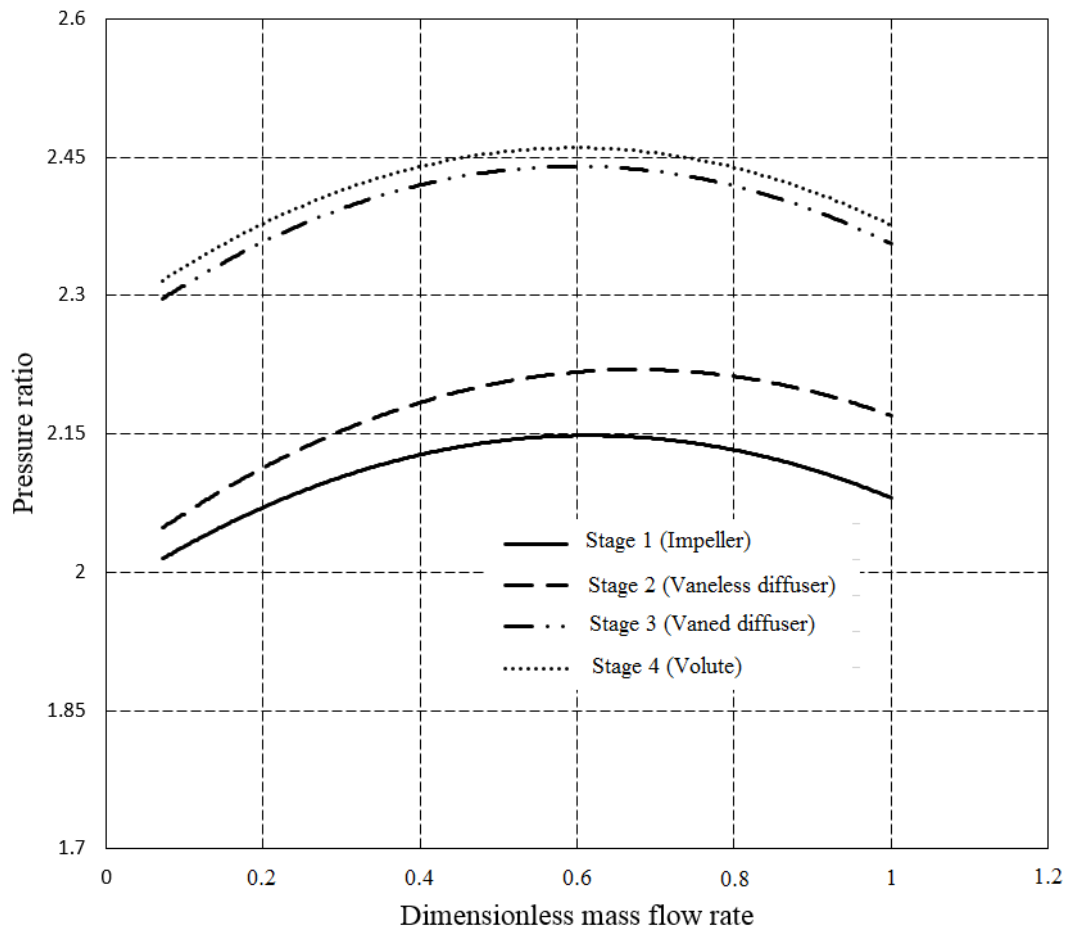


Figure 4.4 The pressure build up in each compressor component ($N = 170K$ rpm)

4.4 Individual Loss Investigation

As the impact of loss mechanism on the compressor performance has been studied, individual loss investigation will be important to help with how to reduce losses thus to increase compressor performance. It is also helpful for understanding different loss process by individual loss analysis. For instance, how is variations of incidence loss and skin loss in the impeller changes as a function of mass flow rate and rotational speed.

4.4.1 Effects of Mass Flow Rate and Rotational Speed on Individual Loss

As mentioned previously, to increase compressor performance by reducing losses in each component, the first thing is to understand individual loss mechanism. Because mass flow rate and rotational speed are two main inputs, it is essential to see variation of individual loss as function of mass flow rate and rotational speed. Figures below show the changes of several losses with mass

flow rate and rotational speed. The chosen losses are those which are more dominate to compressor performance than other losses. By reducing these dominate losses in centrifugal compressor, it can help designers to improve compressor performance distinctly. Figure 4.5 shows the relation between impeller incidence loss coefficient and mass flow rate at four rotational speeds such as 90K rpm, 130K rpm, 170K rpm, and 210K rpm.

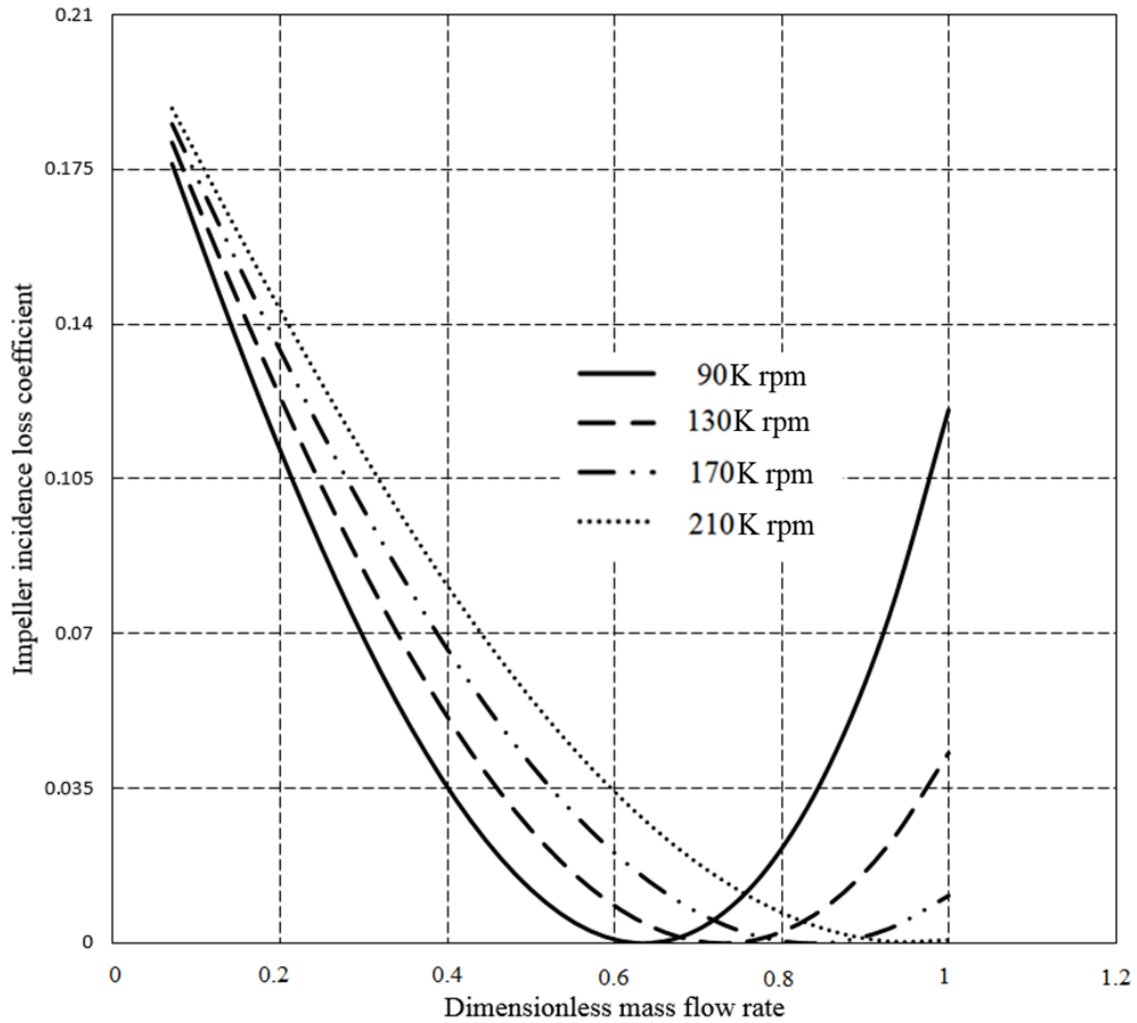


Figure 4.5 Dependency of impeller incidence loss on mass flow rate

It can be seen that incidence loss coefficient are the highest for all rotational speeds investigated with lower mass flow. It decreases as mass flow increases and then increases as the mass flow increases with a mass flow higher than 0.62. As mentioned before, incidence loss is related to incidence angle. Blade angle is always fixed, however flow angle at the inlet of the impeller can be changed with the variation of rotational speed of impeller or mass flow rate. The incidence loss reaches its minimum value where the blade angle and flow angle coincides and the incidence loss

increases as the absolute incidence angle increases. With higher incidence angle, it will require more effort to change the flow to the right direction and therefore higher loss will be encountered. The loss can, however, be minimized through the entire operating range at the cost of installing variable inlet guide vanes to ensure that the flow angle corresponds to the blade angle over most of the operating range. Using the proposed prediction model, the designer can now determine the loss for different operating conditions and determine whether potential improvements justify the cost and complexity of variable inlet guide vanes.

In Figure 4.6, it shows the variation of impeller blade loading loss as a function of mass flow rate at four rotational speeds of 90K rpm, 130K rpm, 170K rpm, and 210K rpm.

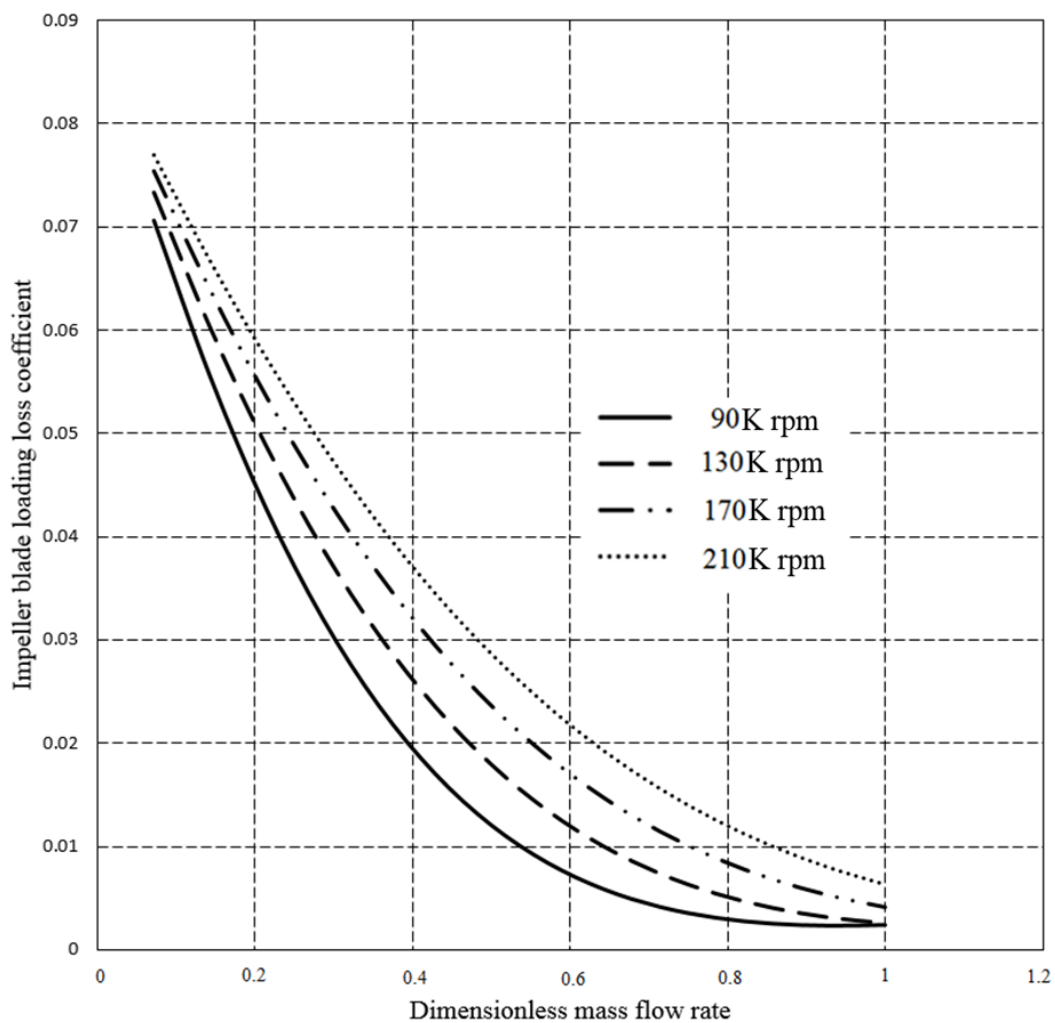


Figure 4.6 Dependency of impeller blade loading loss on mass flow rate

It can be seen that impeller blade loading loss coefficient decreases when mass flow rate goes up. It decreases sharply in the first half of compressor operating range and the curve becomes smooth

when non-dimensionalised mass flow rate over 0.6. The reason for this is that impeller blade loading loss coefficient is depend on the diffusion factor which is the ratio of the relative velocity of the flow at the exit to relative flow velocity of the inlet at shroud. Both of those two velocities will be higher with higher mass flow rate. However, the degree of increase in the relative flow velocity at the exit and the inlet is different. The relative flow velocity at the exit increases more at shroud because the tangential component at the exit is higher which is a typical characteristic of the centrifugal compressor.

In Figure 4.7, it shows the correlation between impeller skin friction coefficient and mass flow rate at four rotational speeds of 90K rpm, 130K rpm, 170K rpm, and 210K rpm.

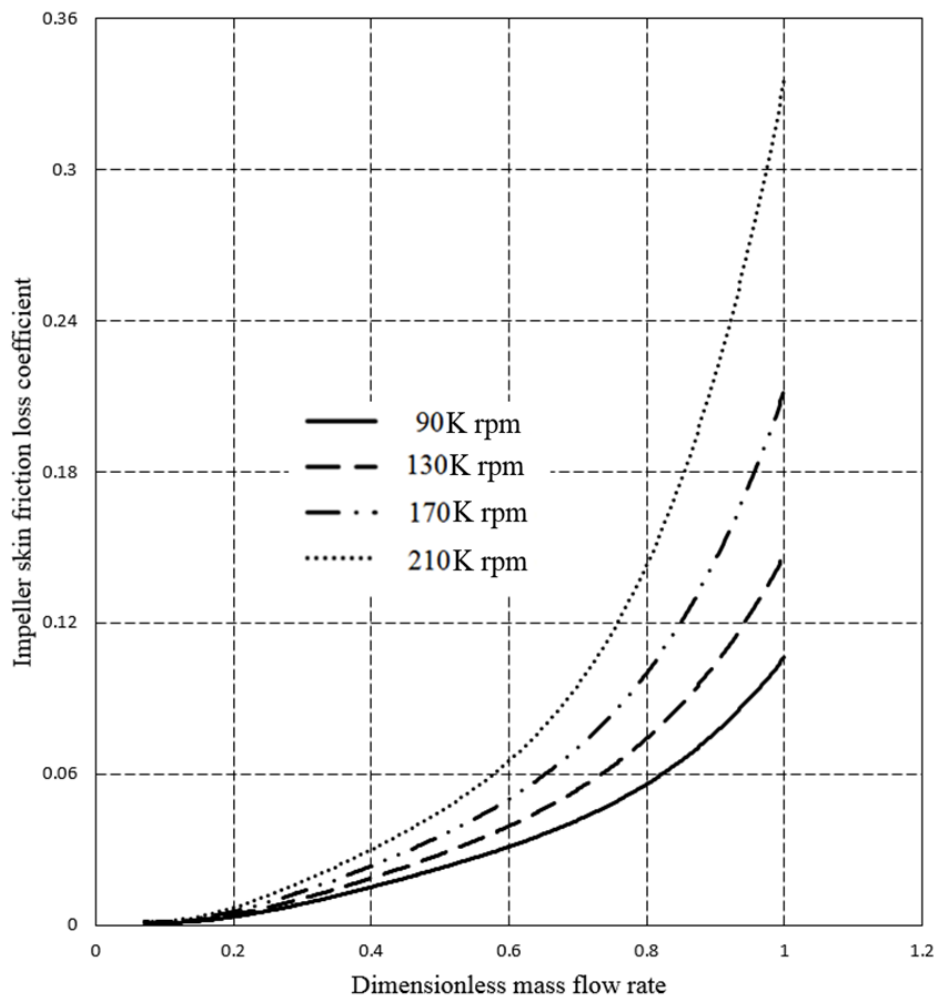


Figure 4.7 Dependency of impeller skin friction loss on mass flow rate

It can be seen impeller skin friction loss coefficient increases as the mass flow rate increases. However, it increases significantly when non-dimensioalised mass flow rate goes over 0.5. It means that skin friction loss is more prominent at higher mass flow rate. The physical explanation

behind this can be that impeller skin friction loss is directly dependent on mean velocity, and the increased mass flow rate in turn increases the mean velocity component. It is well known that friction loss is quite related with the surface roughness, therefore smooth blade surface can minimise impeller skin friction loss even though the cost is noticeable [65]. However, under the help of the developed model for skin friction loss, designer can calculate the exact magnitude of the loss effect on efficiency to determine whether additional machining cost to obtain a smoother blade surface is adjustable or not.

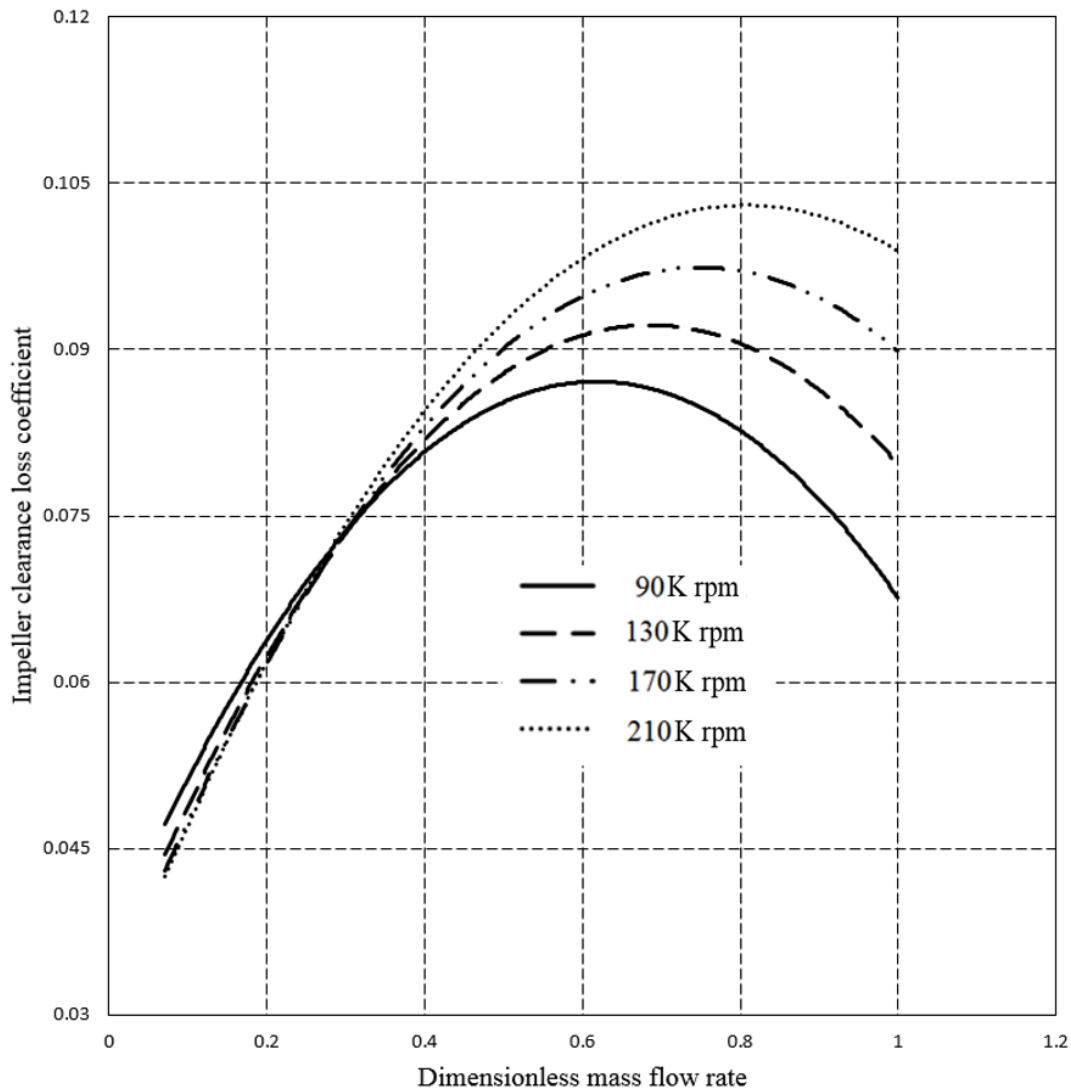


Figure 4.8 Dependency of impeller clearance loss on mass flow rate and rotational speed

As shown in Figure 4.8, the correlation between impeller clearance loss coefficient and mass flow rate can be found at four rotational speeds of 90K rpm, 130K rpm, 170K rpm, and 210K rpm.

It can be seen that impeller clearance loss coefficient goes up with the increase of mass flow rate, and it then decrease quickly at high mass flow rate. The physical meaning behind it is that impeller

clearance loss is proportional to the gap between blades and housing. The larger the gap, the larger the leakage flow and associated loss that can be expected due to the pressure difference over blades. Meanwhile, impeller clearance loss also increases by a larger difference in velocity between the main flow and leakage flow. Increasing mass flow rate will increase flow velocity through impeller. This causes the difference in velocity between leakage flow and main flow to increase, thus increasing the clearance loss. However, at some stage the clearance loss starts to decrease although mass flow still increases. This can be explained by the fact that pressure ratio decreases as a result of increasing mass flow, a characteristic of compressor performance curves. The lower pressure ratio causes less flow to leak over impeller blades, thus decreases the clearance loss.

Figure 4.9 shows the effect of mass flow and rotational speed on the impeller loss coefficient with four different speeds: 90K rpm, 130K rpm, 170K rpm and 210K rpm.

It can be seen that impeller mixing loss coefficient decreases with an increasing mass flow rate. The physical meaning behind it could be that impeller mixing loss is correlated with the jet flow area and the wake flow area. With an increasing mass flow rate, jet flow area will increase dramatically. This means that the wake flow area decreases and mixing loss decreases with an increasing mass flow rate. It also explains that impeller mixing loss coefficient decreases quicker when non-dimensionalised mass flow rate lower than 0.6. It also shows impeller mixing loss coefficient reaches its maximum value at a higher rotational speed.

In Figure 4.3, it can be seen that vaned diffuser skin friction loss is also remarkable in all losses degrading compressor performance. Therefore, the relation between vaned diffuser skin friction loss coefficient and mass flow rate should be considered. The simulation result can be seen in Figure 4.10.

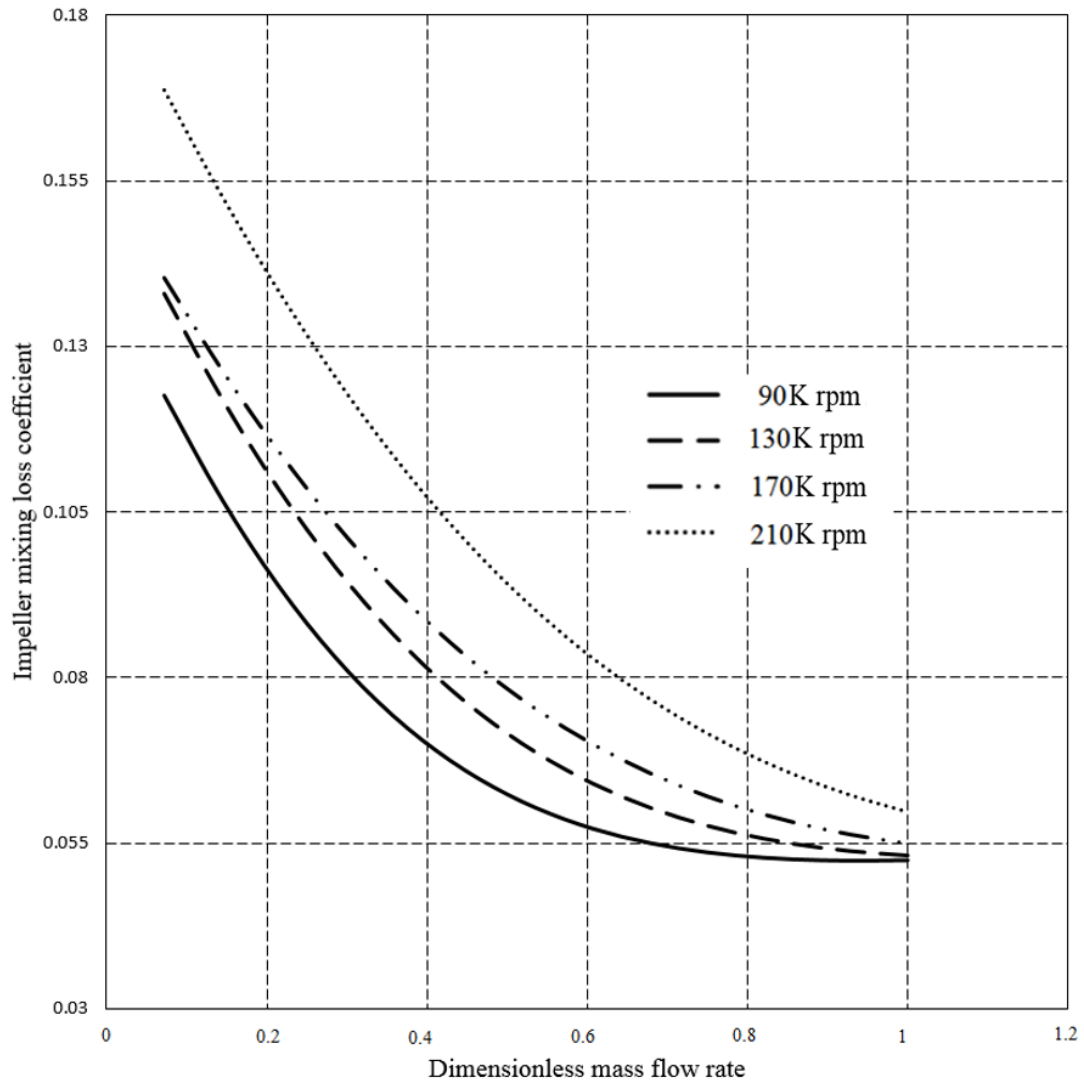


Figure 4.9 Dependency of impeller mixing loss on mass flow rate

Similarly as skin friction loss in impeller and vaned diffuser skin friction loss coefficient shows an ascending trend with the increase of the mass flow rate. It shares the same physical meaning with impeller skin friction loss coefficient. Skin friction loss is directly dependent on the mean velocity, and higher mass flow rate provides fast flow in vaned diffuser. However, the quantity of vaned diffuser skin friction loss coefficient is less than the one with impeller. The reason behind it could be the flow velocity in vaned diffuser is lower than it is in impeller due to the compression in vaneless diffuser. Similarly, vaned diffuser skin friction loss coefficient is also depends on surface roughness. Simulation results could help designer trade-off between higher diffuser efficiency and cost in development.

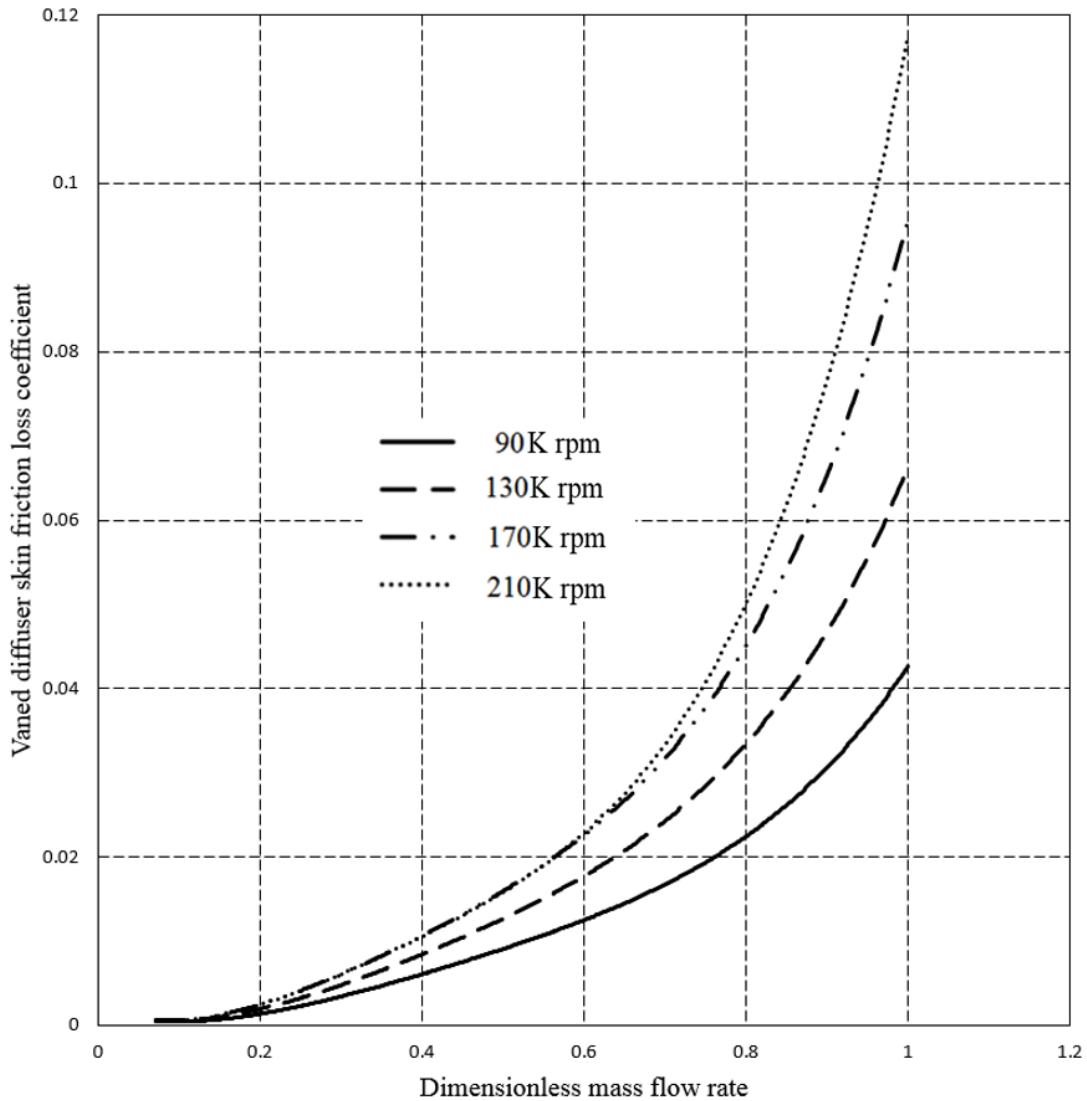


Figure 4.10 Dependency of vaned diffuser skin friction loss on the velocity

4.4.2 Correlations between Individual Loss and Flow Velocity and Its Angle

By understanding the correlation between individual loss and mass flow rate at different rotational speeds, it is worthy to detect the physical interpretation behind it. Simulation of flow velocity and flow angles is useful to get a better understanding of flow in each component of the compressor. It is also helpful to explain the physical meaning of loss mechanism. First of all, it is useful to get a better understanding of the incidence loss mechanism by investigating the effect of the flow angle at the impeller inlet on the impeller incidence loss, which can be seen in Figure 4.11.

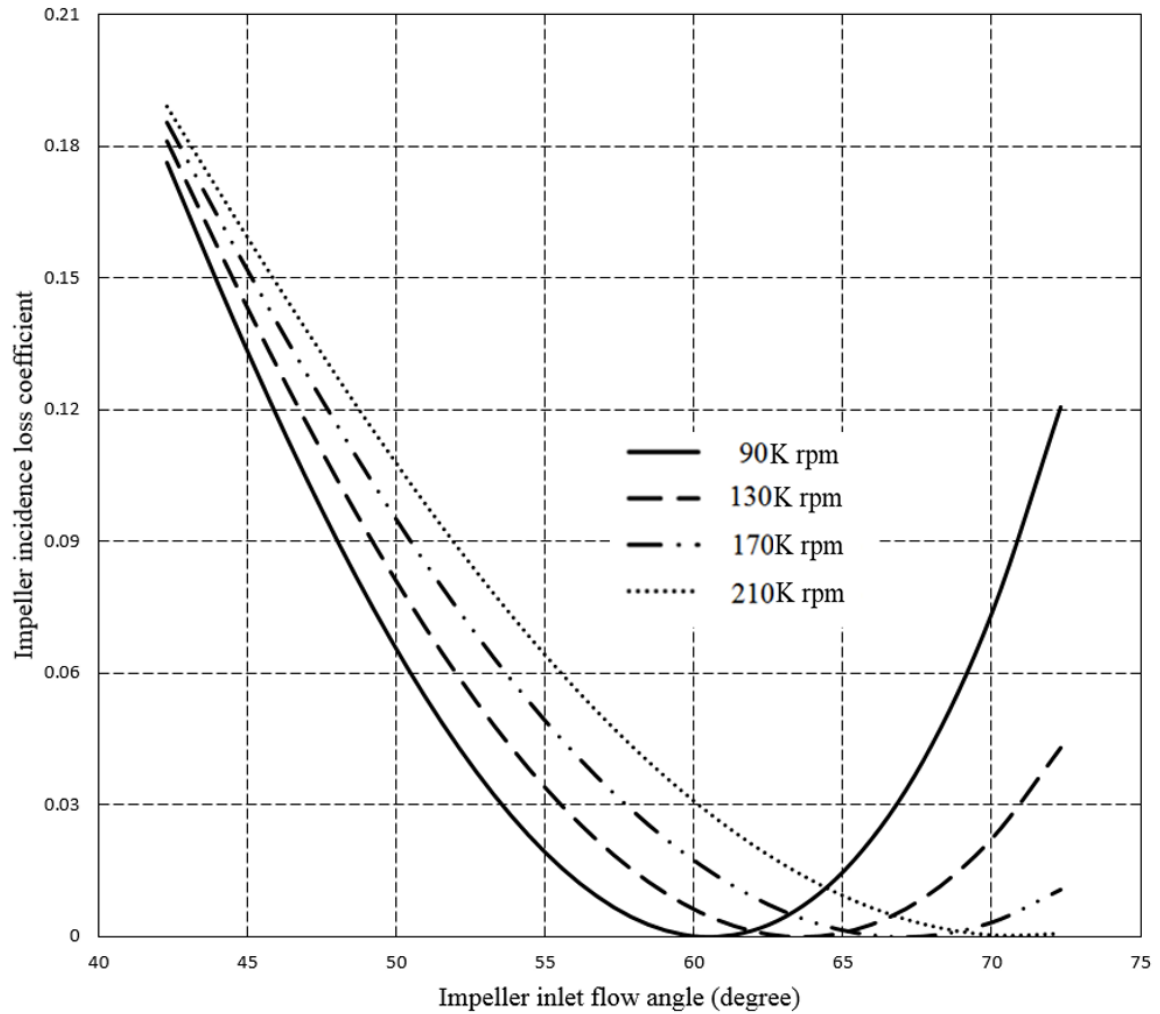


Figure 4.11 Dependency of impeller incidence loss on inlet flow angle

It can be seen that the dependency of impeller incidence loss coefficient on the flow angle at impeller inlet shows a similar trend as the relation between impeller incidence loss coefficient and mass flow rate. It suggests that impeller incidence loss coefficient is directly dependent on the incidence angle. When impeller incidence loss coefficient becomes zero, it means that blade angle and flow angle coincides. When flow angle increase, incidence angle goes up due to blade angle is fixed. Impeller incidence loss coefficient is proportional to the incidence angle. It also shows that flow angle changes for different rotational speeds due to different velocity triangles at impeller inlet.

For the investigation of impeller skin friction loss coefficient, it is worthy to simulate the relation between impeller skin friction loss coefficients and flow velocity at impeller inlet. Simulation results can be seen in Figure 4.12.

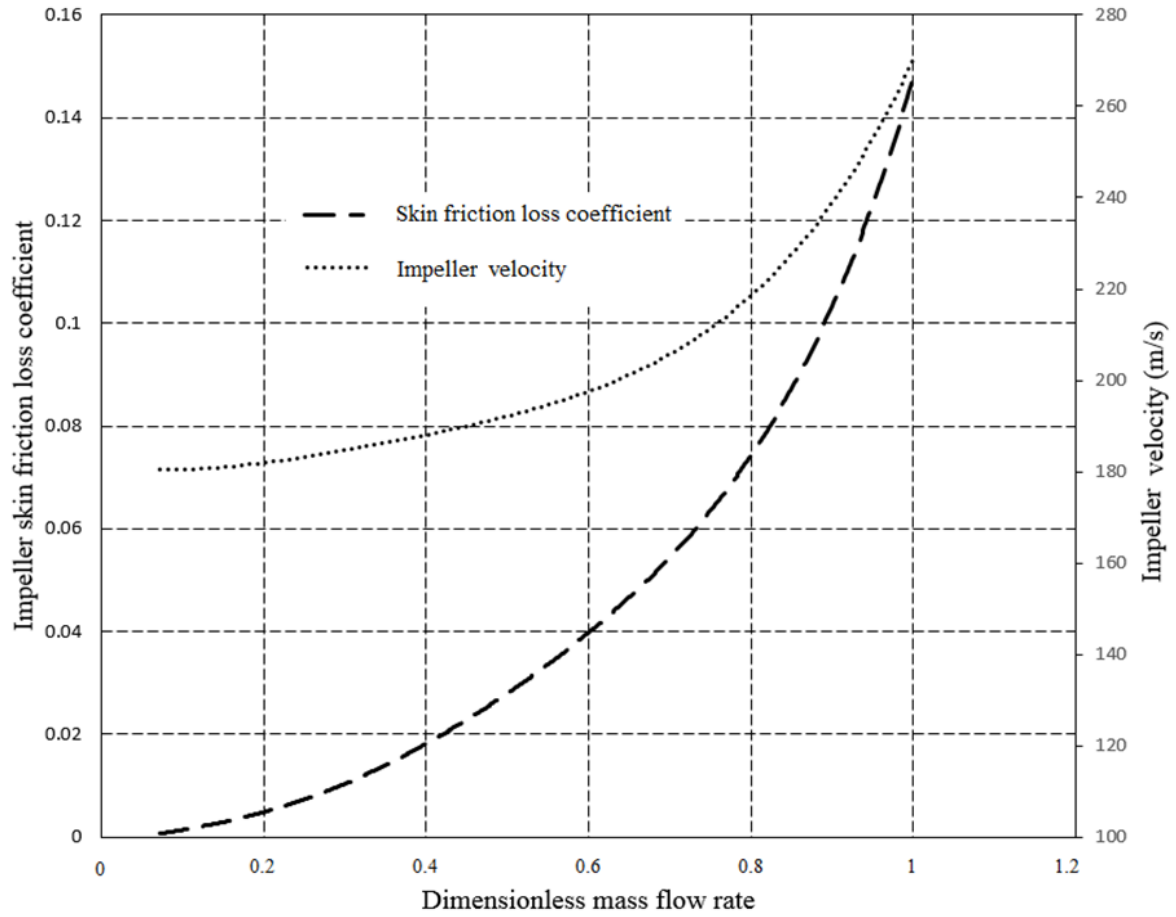


Figure 4.12 Dependency of impeller skin friction loss on velocity

The correlation between impeller inlet velocity and mass flow rate shows a similar trend as the correlation between impeller skin friction loss coefficients and mass flow rate. As mentioned before, impeller skin friction loss is proportional to mean velocity in impeller. As mass flow rate increases, impeller velocity goes up from less than 100m/s to 270m/s. Higher impeller inlet velocity result in increased impeller skin friction loss coefficient. Due to higher flow velocity in impeller, impeller skin friction loss coefficient has more influence on compressor performance than skin friction loss coefficient in other components in compressors.

4.4.3 Effect of Geometry Change on Individual Loss

After studying the physical interpretation behind the dependency of individual loss on mass flow rate at different rotational speeds, effects of compressor geometry parameters on individual loss were investigated. In the design stage, compressor geometry such as impeller diameter, blade angle, and even blade numbers must be carefully optimised in order to have an ideal turbocharger performance. Figure 4.13 below shows dependency of impeller skin friction loss on impeller exit diameter.

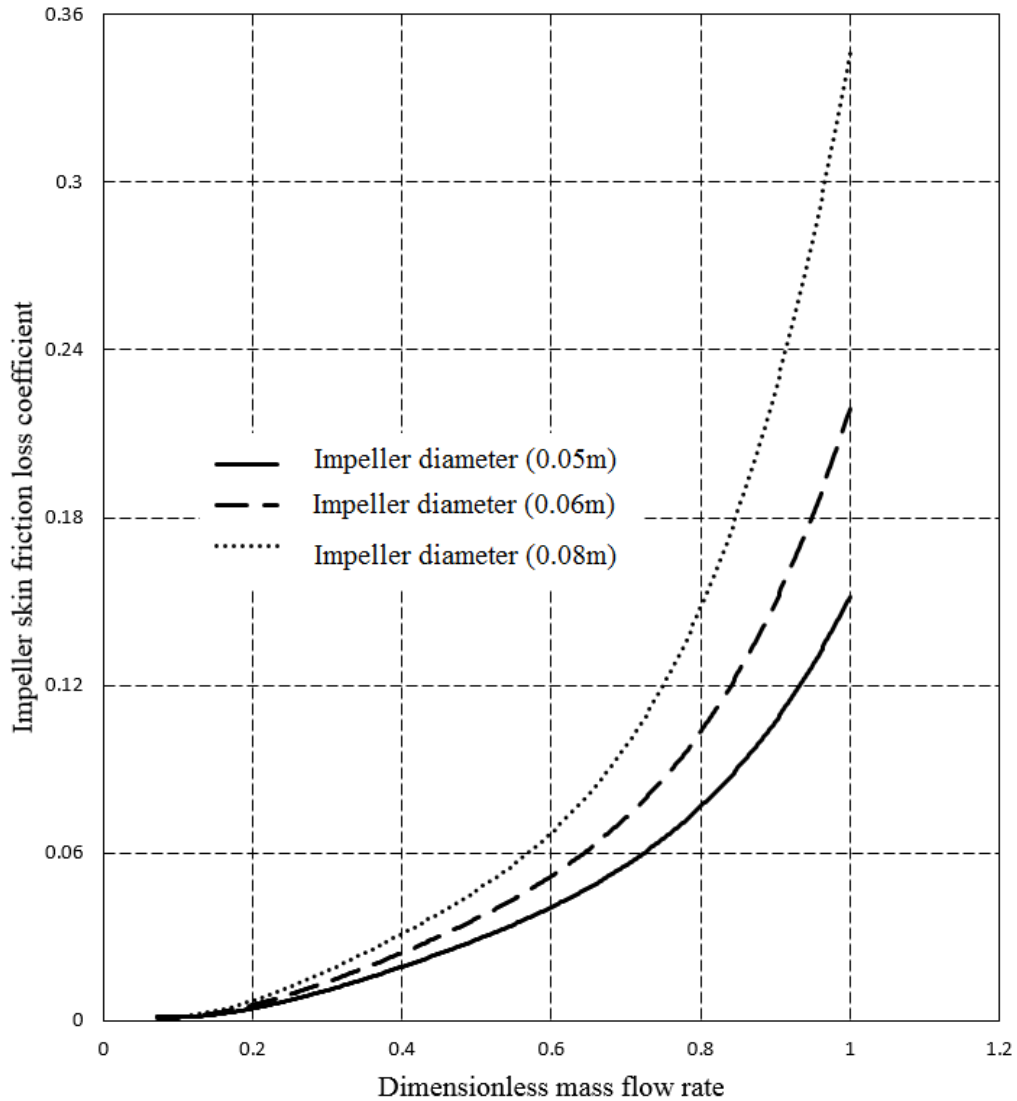


Figure 4.13 Dependency of impeller skin friction loss on exit diameter

As shown in Figure 4.13, it can be seen that impeller skin friction loss will increase as the rotor inlet diameter increases. The reason for that is the increased rotor inlet diameter in turn increases the mean velocity component. Skin friction loss is directly dependent on the mean velocity. Apart from that, skin friction loss is also dependent on the friction factor. Simulation results can help the designer carefully choose impeller size to deal with the trade off between the compressor performance and efficiency.

Figure 4.14 shows the correlation between impeller clearance loss coefficient and mass flow rate at different clearance gaps showing the effect of clearance gap on clearance loss.

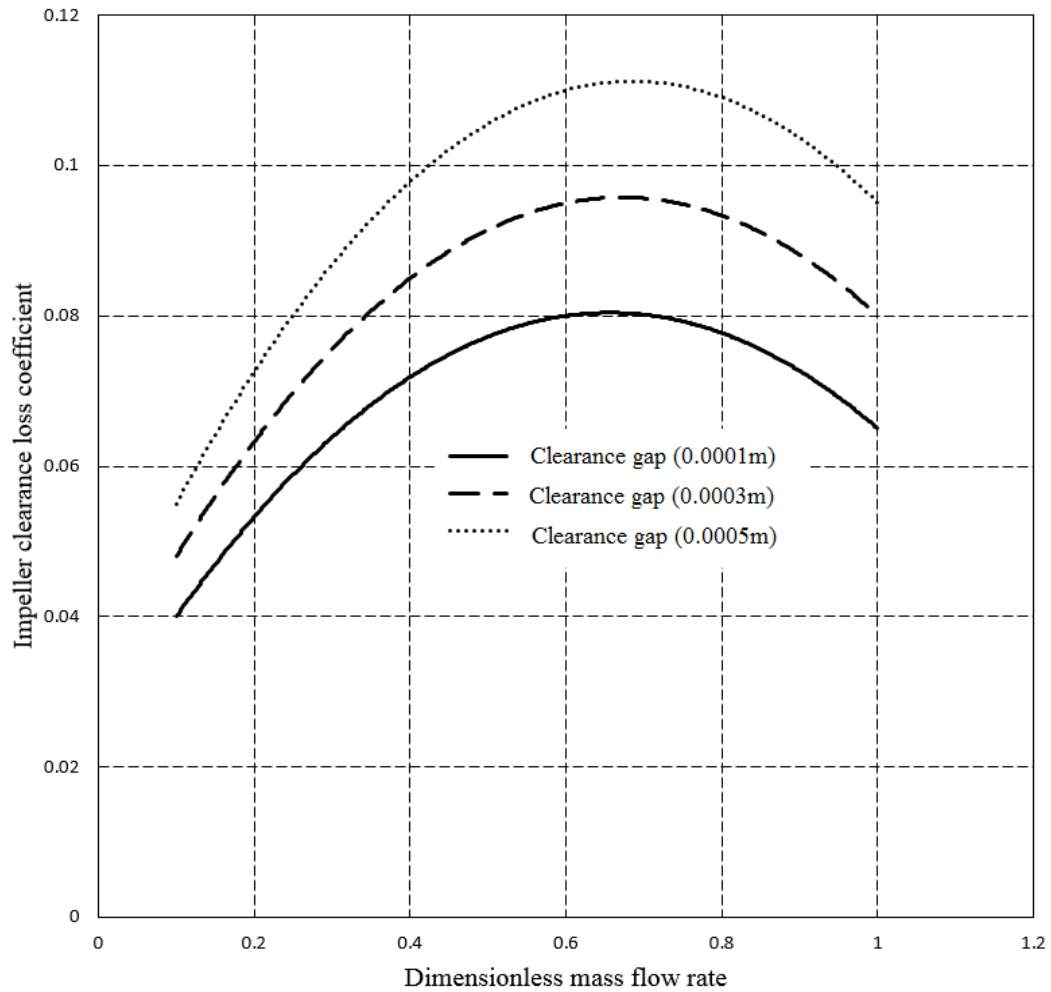


Figure 4.14 Dependency of impeller clearance loss on clearance gap

It can be seen that impeller clearance loss coefficient increase with the increase of the clearance gap up to a value of approximately 0.7. As mentioned before, the larger the gap between blade and housing, the larger leakage flow and associated loss that can be expected due to the pressure difference over blades. Therefore, it is important to keep the clearance gap as small as possible. However, this depends rather severely on manufacturing tolerances making it a rather expensive process for high performance designs. Using the developed model for estimating clearance loss, designers can now calculate clearance loss and optimise performance with respect to minimising clearance loss and unit cost.

In Figure 4.15, it shows the effect of the impeller blade angle on impeller incidence loss coefficient.

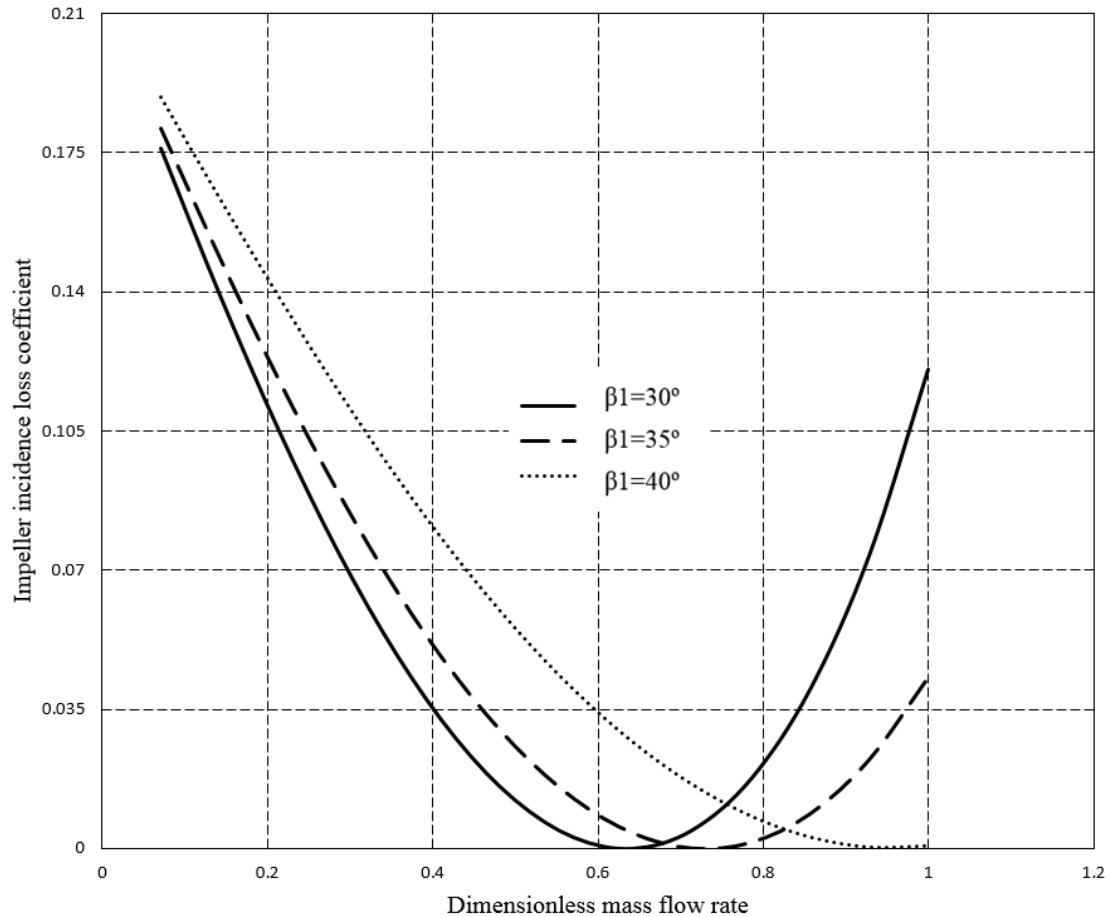


Figure 4.15 Dependency of impeller incidence loss on blade angle

A bigger blade angle will result in a higher impeller incidence angle, a small angle should be chosen normally. However flow angle at impeller inlet also increases as the mass flow rate increases. The choice of the blade angle should consider the operating range in terms of mass flow rate and rotational speeds. The effects of blade angle on the impeller incidence loss coefficient shows a similar trend as the correlation between impeller incidence loss coefficient and mass flow rate. However, different choices of blade angle could also shift impeller incidence loss coefficient characteristic. The physics behind it could be impeller incidence loss coefficient becomes zero when blade angle and flow angle coincides.

4.5 Flow Analysis in the Centrifugal compressor

The investigation of different loss mechanisms in centrifugal compressor is very helpful to improve compressor efficiency. However, the simulation of correlations of mass flow rate, rotational speed and velocity triangles is essential for understanding the compressor performance in depth. To get insight into flow details of a centrifugal compressor, it is necessary to study the effects of mass

flow rate and rotational speed on thermodynamics at each station. With the study of the effect of mass flow rate and rotational speed on velocities, it can be noted that the developed model is capable of predicting of the compressor performance.

4.5.1 Effects of Mass Flow Rate and Rotational Speed on Velocity Triangles

Figure 4.16 shows the correlation between flow velocity at impeller exit and mass flow rate at three different rotational speeds of 90K rpm, 130K rpm, and 170K rpm.

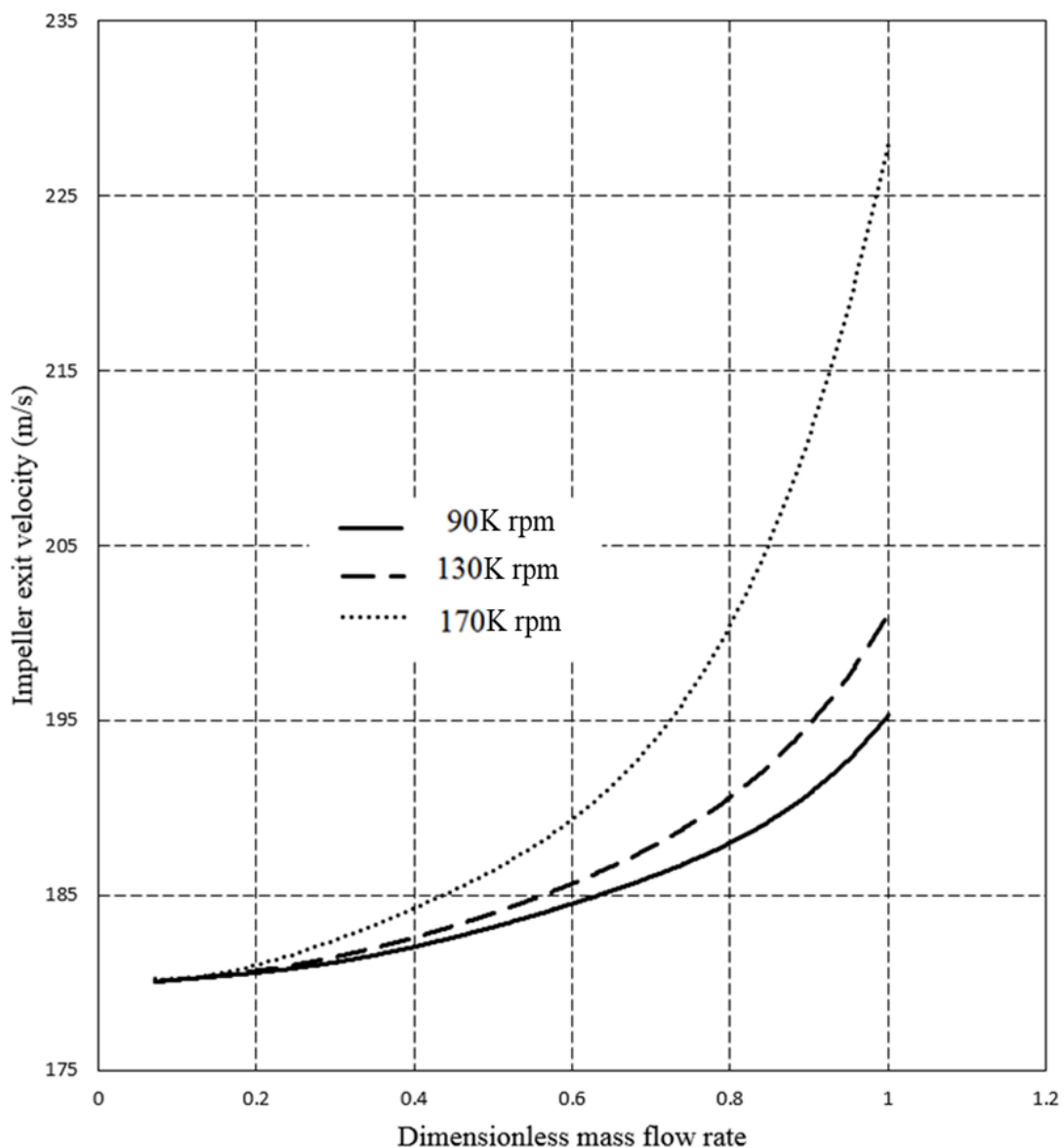


Figure 4.16 Dependency of Impeller exit velocity on mass flow rate

It can be seen that flow velocity at impeller exit increases when mass flow rate goes up. And the flow velocity at impeller exit is also proportional to rotational speed. As mentioned in chapter 3, impeller exit velocity is related to the radial and tangential component. The tangential component

is related to impeller tip rotational speed, which explains that impeller exit velocity increase when rotational speed goes up, as seen in Figure 4.16. When mass flow rate increase, the radial components of absolute velocity goes up according to the conservation of mass, which also push up impeller exit velocity.

4.5.2 Dependency of Flow Angles on Mass Flow Rate and Rotational Speed

Figure 4.17 shows the correlation between impeller inlet flow angle and mass flow rate at three different rotational speeds of 90K rpm, 130K rpm, and 170K rpm.

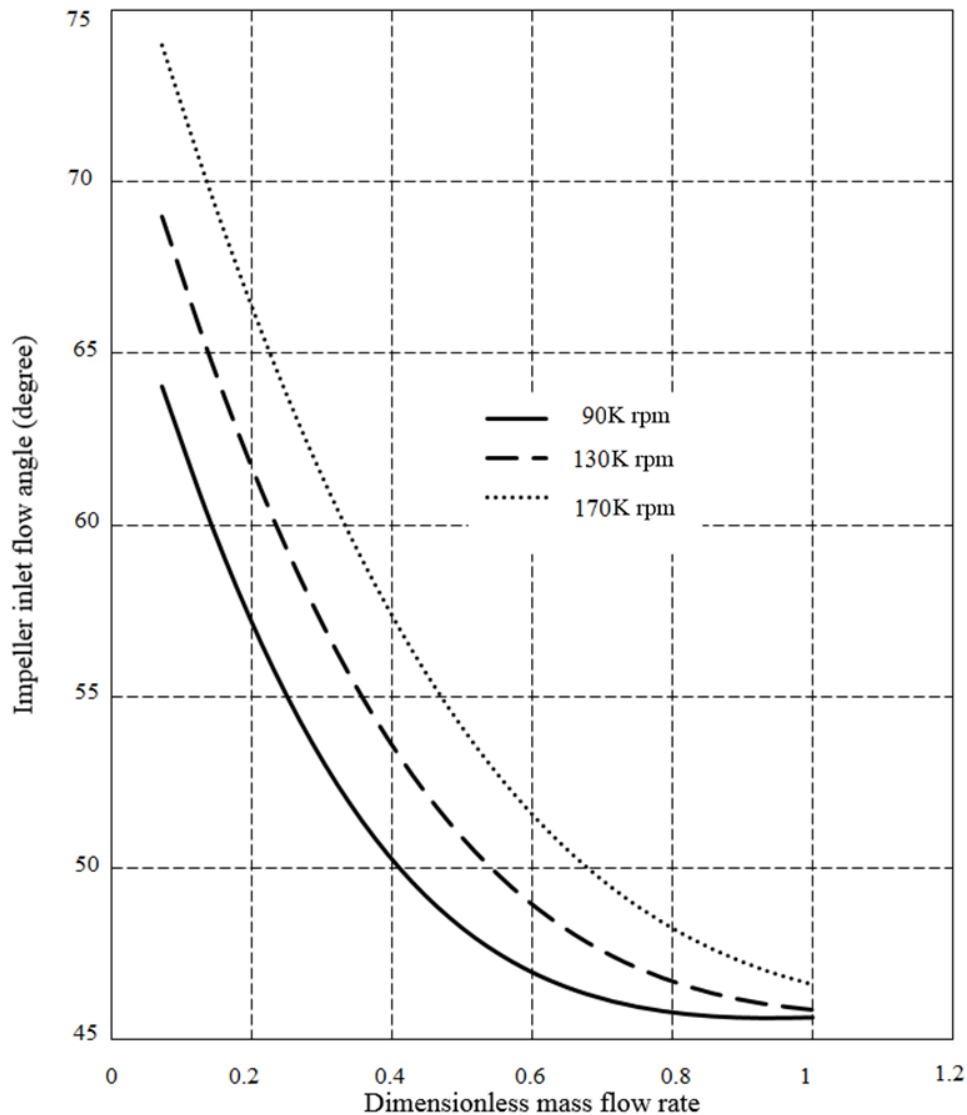


Figure 4.17 Dependency of impeller flow angle on mass flow rate

It can be seen that impeller inlet flow angle decreases when mass flow rate goes up. It could be caused by that impeller inlet flow angle and the radial absolute inlet velocity have an inverse

relationship. As mentioned in Chapter 3, velocity triangle at impeller inlet changes with different mass flow rates. By increasing the mass flow rate, the radial component of absolute inlet velocity will increase due to the conservation of mass when the area of the inlet is constant.

4.6 Summary

The proposed compressor model has been validated using experimental data collected from a 2.0 L diesel engine testbed. Simulation results and experimental data have been compared at four rotational speeds of 90K rpm, 130K rpm, 170K rpm, and 210Krpm. All speed lines have good agreements with the experimental data. The proposed model also predicts surge point in good accuracy, which is very important for defining the stable operating range of the compressor. The prediction of compressor isentropic efficiency also has good agreements with the experimental data.

With the help of the proposed compressor model, all losses in the compressor have been plotted in one graph, which is helpful to distinguish the dominating losses in each component. The pressure ratio is constant with different mass flow rates with no loss in the system. The dominant losses in centrifugal compressors are incidence loss, impeller skin friction loss in the impeller and skin friction loss in the vaned diffuser because they have significant effects on compressor characteristics.

Results also showed the effect of different components on compressor performance. It has been found that the pressure increase was mostly achieved in the impeller. There is no pressure increase inside the volute, which also confirms that the main function of volute is direct the flow to in the required direction.

Individual loss investigation has also been carried out to study the loss mechanism and the physics behind that. The correlation between impeller incidence loss coefficient and mass flow rate has been investigated at four rotational speeds investigated. Similar investigations have been applied to impeller blade loading loss coefficient, impeller skin friction loss coefficient, impeller clearance loss coefficient, impeller clearance loss coefficient as well as impeller mixing loss coefficient. Mechanisms for each loss have been explained based on thermodynamic principles and velocity triangles. The understanding of individual loss mechanism could help the designer with the optimised design and trade-off between better design and potential extra costs.

The correlations of mass flow rate, rotational speed and velocity triangles have been investigated in details. To get insight into flow details, it is essential to study the effect of mass flow rate and rotational speed on thermodynamics at each station inside a centrifugal compressor. The

dependency of inlet flow angle of the impeller on mass flow rate also has been reviewed for three different rotational speeds of 90K rpm, 130K rpm, and 170K rpm. Discussions and explanations have been given based on thermodynamics and velocity triangles.

Chapter 5. Turbocharger Losses Model and Validation

5.1 Introduction

Based on the compressor model demonstrated in Chapter 3, a turbine model would be required to compose a complete turbocharger model. A turbocharger model which can be used for engine simulation should have energy conservation between compressor and turbine. The energy conservation equation can be described as

$$L_t * \eta_m = L_c \quad (5.1)$$

where L_t is turbine output power, L_c is compressor input power, η_m is mechanical efficiency of turbocharger.

Another common parameter for both the turbine and the compressor in one turbocharger is the rotational speed because they are connected through the same shaft.

$$N_t = N_c \quad (5.2)$$

where N_t and N_c are rotational speed of turbine and compressor respectively. According to mass conservation, mass flow rate at the turbine inlet are the sum of mass flow rate at compressor inlet plus mass flow rate of fuel burned in engine.

$$\dot{m}_t = \dot{m}_c + \dot{m}_{fuel} \quad (5.3)$$

Where \dot{m}_t is mass flow rate at turbine inlet, \dot{m}_c is mass flow rate at compressor inlet and \dot{m}_{fuel} is mass flow rate of fuel added into engine cylinder.

5.2 Turbine Model

Similar to the compressor model, the one-dimensional model of turbine is based on momentum conservation, energy conservation for steady flows, continuity of mass, thermodynamic state,

and trigonometric relations. Because radial turbine has similar working mechanism as centrifugal compressor works, only the turbine model and turbocharger model will be described in this chapter.

5.2.1 Basic Theories for Turbine Model

Different from centrifugal compressor, pressurized fluid enters the turbines in a radial direction, then goes through a peripheral volute and a stage of radial nozzle vanes. Rotor is next to the nozzle vanes and where the most energy transfer takes place. Diffuser is the component which recovers the exhaust kinetic energy of fluid after rotor exit. The radial turbine structure can be seen in Figure 5.1

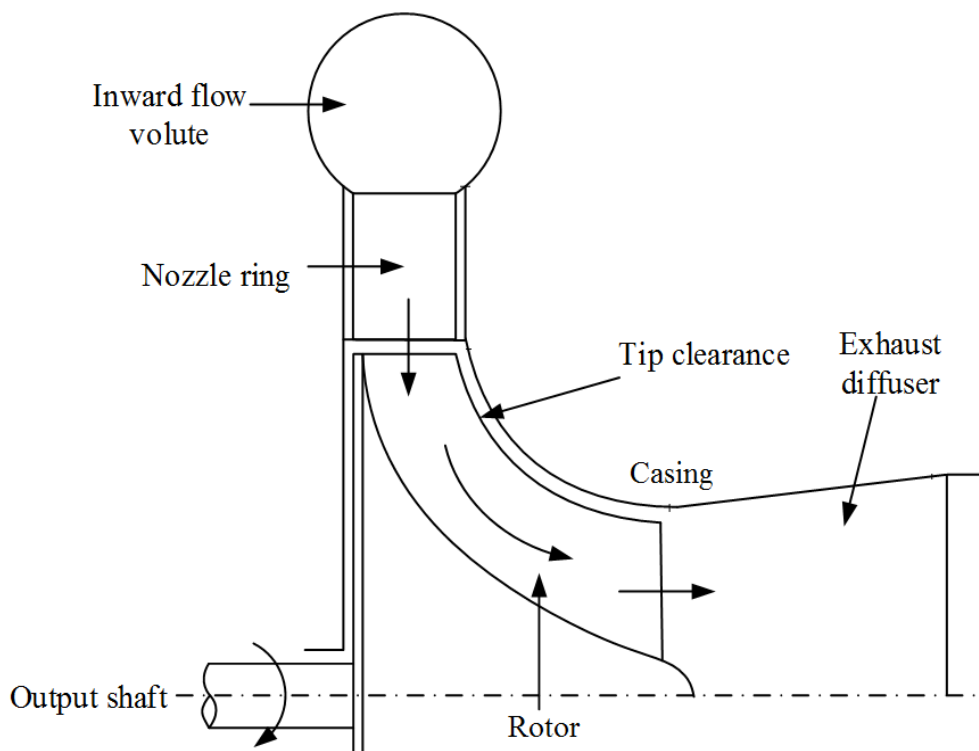


Figure 5.1 Radial turbine structure [73]

For modelling purposes, the radial turbine has been divided into four individual components. Then six stations can be labelled as shown in Figure 5.2. As can be seen station 1 to 6 are totally distinct from the centrifugal compressor model due to different physical structure. Station 1 is volute inlet and Station 2 is volute exit which is also nozzles inlet. It is assumed that the

thermodynamic conditions at nozzles inlet are the same as at volute exit. Similarly, the nozzles exit and turbine rotor inlet have the same conditions. Nozzles exit is Station 3. Although thermodynamic conditions at rotor inlet are the same as nozzles exit, rotor inlet is labelled as Station 4 because a relative velocity is introduced here. Different from nozzles, rotor has more complex velocity triangles presented at the rotor inlet. Station 5 indicates the rotor exit while station 6 indicates the diffuser exit.

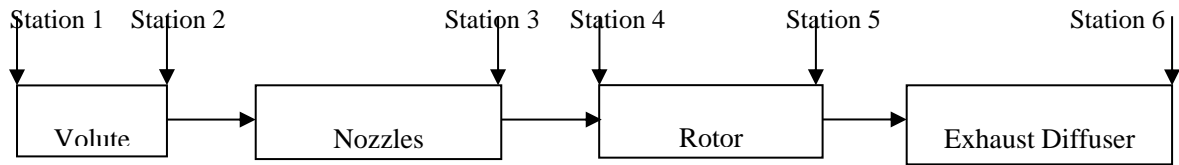


Figure 5.2 Radial turbine component division

Each component in the radial turbine model is fully described with a collection of equations and relevant flow parameters. A set of algebraic equations are related to both the input and output conditions. As mentioned before, equations are all based on rather than empirical expressions. They are derived from equations of energy for steady flows, continuity of mass, conservation of momentum, and thermodynamic equation of state and velocity triangles.

5.2.2 The Volute Model

The purpose of volute in radial turbine is to correct distribute flow to the stator, from the periphery of component to the central part. A typical radial turbine inlet volute can be seen in Figure 5.3

where r_1 and r_2 are the radius at volute inlet and exit respectively. C_1 is velocity at the inlet of volute and A_1 represent volute inlet area.

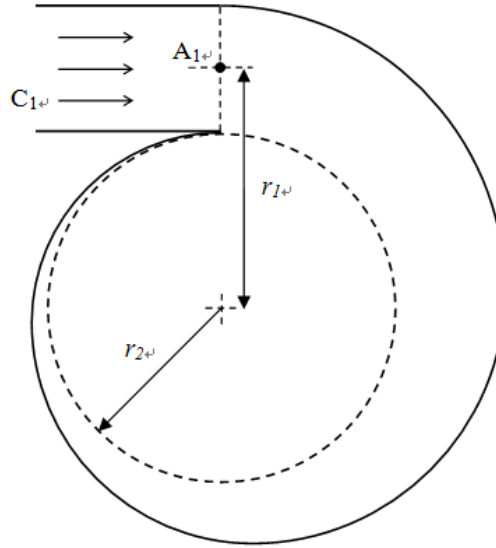


Figure 5.3 Schematic representation of a volute [34]

The volute inlet area A_1 can be calculated from radius at volute inlet and exit.

$$A_1 = \pi(r_1 - r_2)^2 \quad (5.4)$$

The velocity at inlet of volute C_1 can be calculated using the continuity equation.

$$C_1 = \frac{\dot{m}}{\rho_1 A_1} \quad (5.5)$$

Where ρ_1 is density at volute inlet and it can be computed using inlet pressure and temperature.

$$\rho_1 = \frac{P_1}{RT_1} \quad (5.6)$$

5.2.3 Losses in Volute

Two types of non-dimensionalised losses in volute were taken into consideration which will be discussed in the following sections.

5.2.3.1 Calculation of Circumferential Distortion Losses

The circumferential distortion loss coefficient takes into accounts of mixing losses associated with circumferentially non-uniform angular momentum imposed at volute exit [83]. It is given

as

$$K_{\text{cir}} = \left(\frac{r_1 C_1}{r_2} - C_{2u} \right)^2 \frac{1}{C_2^2} \quad (5.7)$$

5.2.3.2 Calculation of Skin Friction Loss

Skin friction loss or wall friction is caused by viscous effect of flow. The skin friction loss in impeller can be defined as [69]

$$K_{\text{sf}} = 4C_f \left(\frac{C_2}{C_1} \right)^2 \frac{L}{D_H} \quad (5.8)$$

where L is mean stream line path length of volute and it can be calculated as

$$L = \frac{\pi(r_1 + r_2)}{2} \quad (5.9)$$

D_H is hydraulic diameter of volute and it can be calculated as

$$D_H = \sqrt{\frac{4A_2}{\pi}} \quad (5.10)$$

C_f is skin friction coefficient which can be calculated in similar way as it in compressor.

The actual total pressure is defined as

$$P_{t2,\text{actual}} = P_{t2,\text{ideal}} - \Delta P_{t2} \quad (5.11)$$

The actual total pressure is used to calculate other actual exit conditions of volute using velocity diagrams, total temperature relationship to calculate static temperature, total pressure relationship to calculate static pressure, density, with assumption that total temperature is constant due to constant enthalpy. The actual exit conditions can be used to determine component mean thermodynamic efficiency and power consumption parameters.

5.2.4 The Nozzles Model

The nozzle in radial turbine is constructed by an annular ring of vanes which is normally used

to direct the flow to the next stage. It extracts fluid from volute, which has already given a swirl velocity component, whose approach angle is expressed by value of α_2 . The main aim of volute-nozzle is to accelerate working fluid and to give ideal incidence angle while leaving nozzle annulus, as required by the rotor inlet in the preliminary geometrical design. The structure of nozzles can be found in Figure 5.4

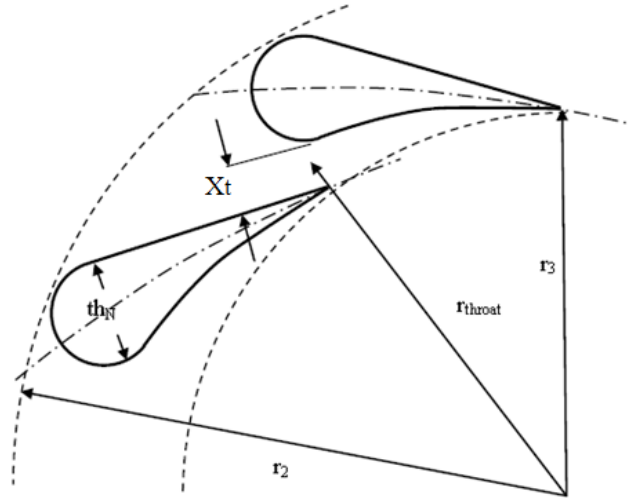


Figure 5.4 Schematic representation of the nozzles [84]

where r_{throat} is radius at nozzle throat, X_t is nozzle throat opening, th_N is thickness of nozzle blade, r_2 and r_3 are radius at nozzle inlet and exit respectively.

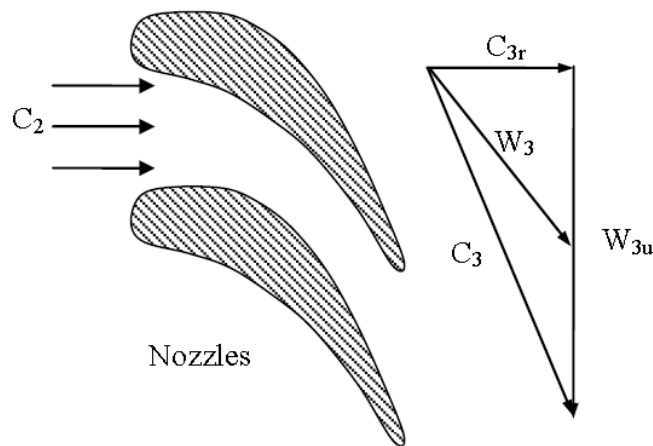


Figure 5.5 Nozzle exit velocity triangles [29]

According continuity equation, velocity at nozzle exit is expressed as

$$C_3 = \frac{\dot{m}}{\rho_3 A_{NT}} \quad (5.12)$$

Radial component of the velocity at nozzle exit is given by

$$C_{3r} = C_3 \cos(\alpha_3) \quad (5.13)$$

Tangential component of velocity at nozzle exit is given by

$$C_{3u} = C_{3r} \tan(\alpha_3) \quad (5.14)$$

In the equation above, A_{NT} is nozzle throat area which can be calculated as

$$A_{NT} = X_t b_3 Z_N - A_{Nb} \quad (5.15)$$

where Z_N is number of nozzle blades.

X_t is nozzle throat opening and it can be calculated as

$$X_t = X_N \cos(\alpha_3) \quad (5.16)$$

where X_N is opening vane spacing and it can be calculated as

$$X_N = \frac{2\pi r_3}{Z_N} \quad (5.17)$$

A_{Nb} is the area occupied by the nozzle blade in radial direction and it can be calculated as:

$$A_{Nb} = th_N b_2 Z_N \quad (5.18)$$

where th_N is the thickness of nozzle blade, b_2 is the nozzle width.

5.2.5 The Variable Nozzle Turbocharger (VNT) Model

Variable Nozzle Turbocharger (VNT), as shown in Figure 5.6, was developed in recent years

for improving turbocharger efficiency and responding time. It provides variable effect aspect ratio (A/R) for different operating conditions. It also has different optimum aspect ratios with low engine speeds and high engine speeds. At low engine speeds, it cannot cope with large aspect ratio for proper boost while it cannot cope with low aspect ratio at high engine speeds with the risk of choke. The aim of VNT is to provide optimum aspect ratio at different operating conditions. Owing to its superior performance, it has been widely employed in current diesel passenger cars.

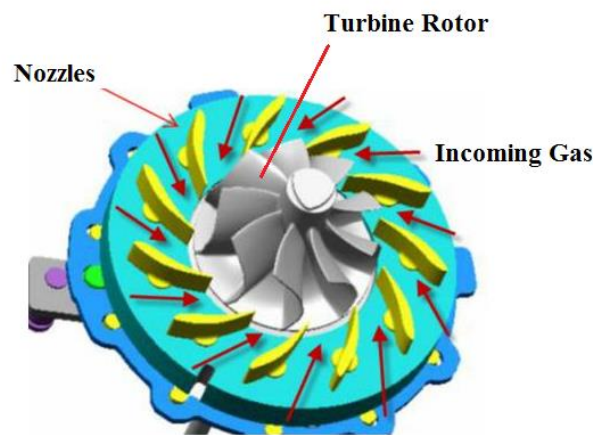


Figure 5.6 Variable nozzle turbine (VNT) [85]

When flow volume of exhaust gas is small and moment energy is also small at low engine speed, vanes are set with narrow spacing. As nozzle opening decreases, the gas at nozzle exit will speed up according to the continuity equation $C_3 = \frac{\dot{m}}{\rho_3 A_{NT}}$. It can be seen in Figure 5.5 that flow angle at nozzle exit α_3 will change with increase of flow velocity. With the increased flow speed, flow also impinges on tip of turbine wheel to increase the moment energy. At high engine speed, the vanes are set to have a wide setting and the turbine wheel works similar as fixed vane turbocharger.

5.2.6 The Rotor Model

Rotor can be considered the most important and most complex component of a radial inflow turbine. The part that has purpose of subtracting energy from fluid and transferring it to rotating

shaft. A typical structure of radial turbine rotor can be seen in Figure 5.7

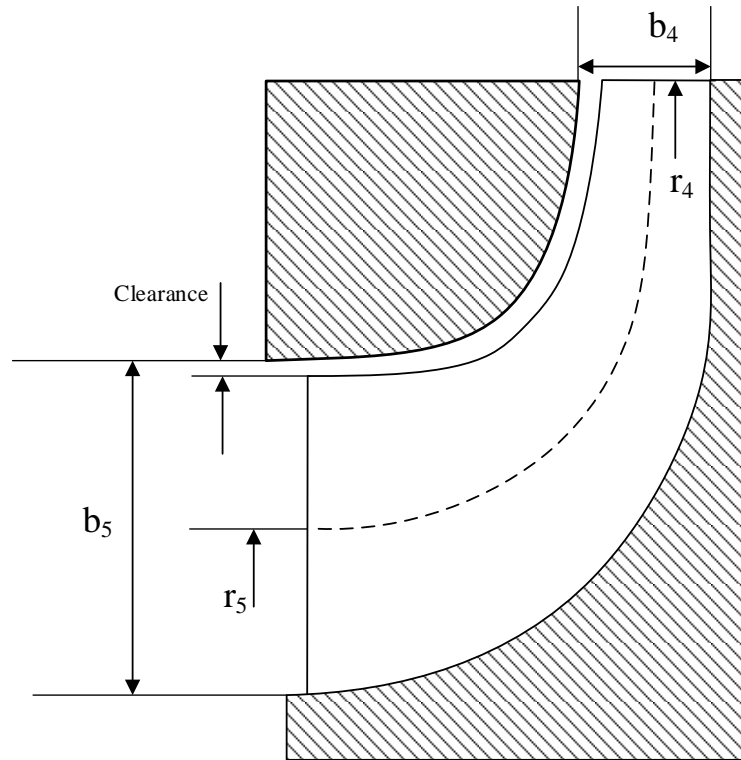


Figure 5.7 Schematic representation of turbine rotor [28]

where r_4 and r_3 are radius at rotor inlet and exit respectively, b_4 and b_5 are widths at inlet and exit.

5.2.7 The Exhaust Diffuser Model

Exhaust diffuser, as shown in Figure 5.8, are commonly used to recover exhaust kinetic energy of the fluid coming out of the rotor. It has different radius at its inlet and exit, so the velocity and pressure of the fluid can be changed due to conservation of angular momentum.

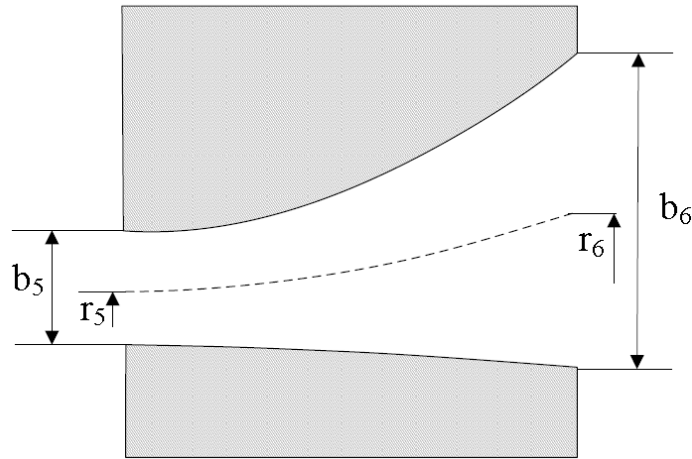


Figure 5.8 Schematic representation of exhaust diffuser [39]

5.3 Calculation of Radial Turbine Power Output

The isentropic power is the difference between the input and the output of the turbine. It can be calculated as the enthalpy between turbine inlet and outlet.

$$P = \dot{m}_{in} \int_0^{T_{in}} C_p dT - \dot{m}_{out} \int_0^{T_{out}} C_p dT \quad (5.19)$$

and it can also be described as

$$P = \dot{m} C_p (T_{in} - T_{out}) \quad (5.20)$$

5.4 Calculation of Radial Turbine Isentropic Efficiency

As mentioned before, isentropic efficiency is normally used to evaluate the performance of turbomachinery. The isentropic efficiency is the ratio of the change of the actual enthalpy inside the turbine and its ideal (i.e. isentropic) enthalpy.

$$\eta = \frac{h_{01} - h_{06}}{h_{01} - h_{s6}} \quad (5.21)$$

Where h_{01} is total enthalpy at turbine inlet, h_{06} is total enthalpy at turbine exit and h_{s6} is

static enthalpy at turbine exit. Different from compressor, total to static isentropic efficiency is commonly used at turbine exit instead of kinetic energy. The turbine isentropic efficiency is a correlation of inlet and outlet flow conditions which can be expressed as follows:

$$\eta = \frac{\left(\frac{P_{t,in}}{P_{t,out}}\right)^{\frac{\gamma-1}{\gamma}} - 1}{\left(\frac{T_{t,in}}{T_{t,out}}\right) - 1} \quad (5.22)$$

5.5 Validation of Turbocharger Model

The proposed model was validated against experimental results obtained on a diesel engine testbed equipped with a VNT turbocharger. Variable Nozzle Turbocharger (VNT) was experimentally tested at different vane positions (20%, 50% and 80% respectively) and different rotational speeds. Three vane positions were then tested at three rotational speeds that are 90K rpm, 130K rpm, and 170K rpm.

The specifications of Variable Nozzle Turbocharger are listed in Table 5.1. Experimental inlet ambient conditions as well as operating conditions were used as input information for the 1D turbine model. The case was numerically performed with different rotational speed and different VGT opening positions with the same boundary conditions as in the experiments.

Table 5.1 The operating conditions and turbine geometry data

Parameter	Value
Turbine Rotor Inlet Diameter (m)	0.043
Turbine Rotor Blade Thickness (m)	0.0033
Rotor Blade inlet angle (°)	30
Blade number	22
Nozzle width (m)	0.012
Nozzle Length (m)	0.035

Diffuser Diameter (m)	0.083
Rotor Blade exit angle (°)	35
Nozzle Thickness (m)	0.0027
Volute inlet diameter (m)	0.095
Volute exit diameter (m)	0.116

5.5.1 Validation of Turbine Expansion Ratio at Different VNT Opening

In Figure 5.9, it shows expansion ratio against mass flow rate under 20% of VNT opening, with three test speeds. Results showed very good agreement with test results. As mass flow rate increases, expansion ratio keeps increase significantly at first. Then the trend becomes more rapid at high mass flow rate. By increasing the speed of the turbocharger, the expansion ratio was significantly increased, in particular for high mass flow rates.

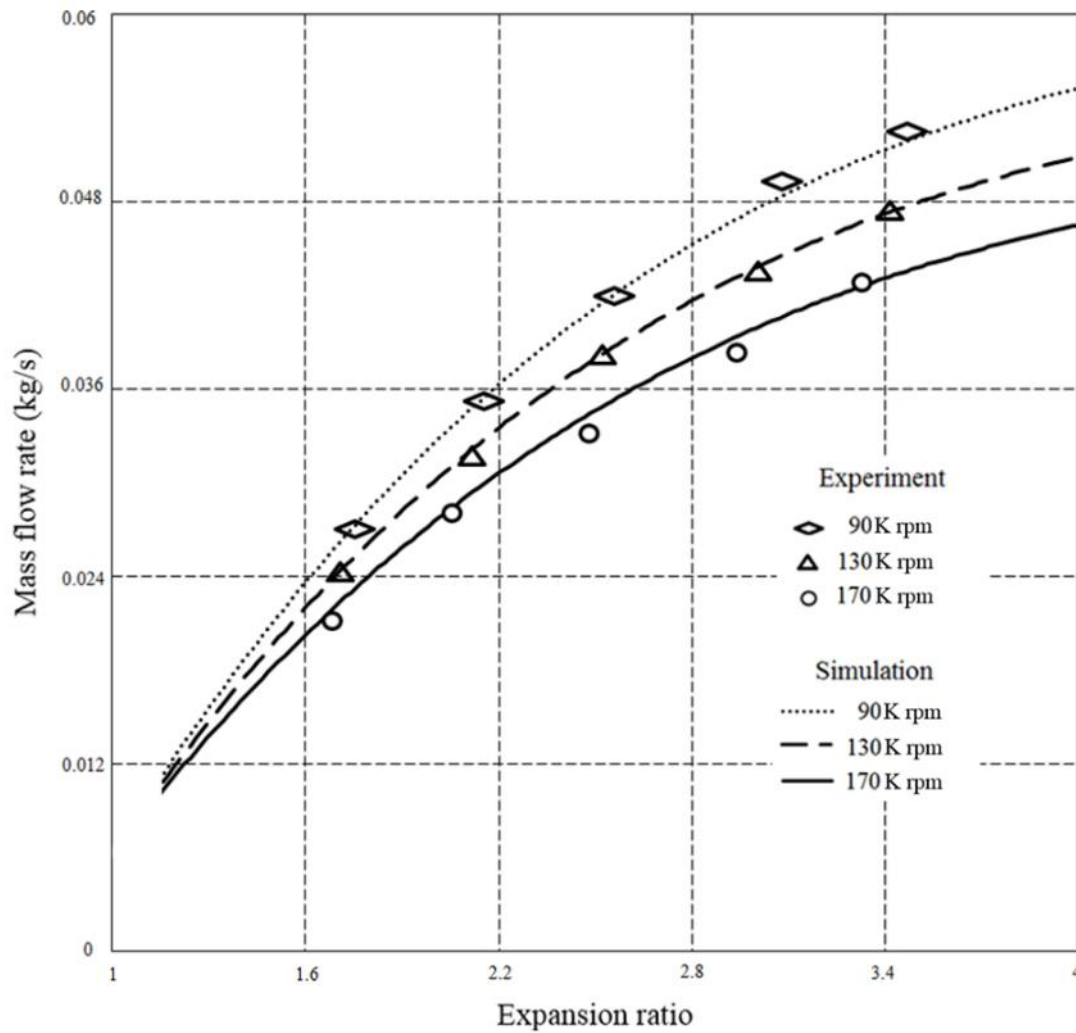


Figure 5.9 Validation of turbine expansion ratio with experimental data (20% opening)

Figures 5.10 and 5.11 show the expansion ratio variation as a function of mass flow rate with 50% and 80% openings at three turbocharger speeds. Simulation results and experimental data are shown to have very good agreement. Meanwhile, the trend is similar as shown in Figure 5.9 for 20% opening. With lower expansion ratio, the comparison at 50% opening has higher mass flow rate than the one at 80% opening. In addition, the influence of turbocharger speed becomes small for 80% openings.

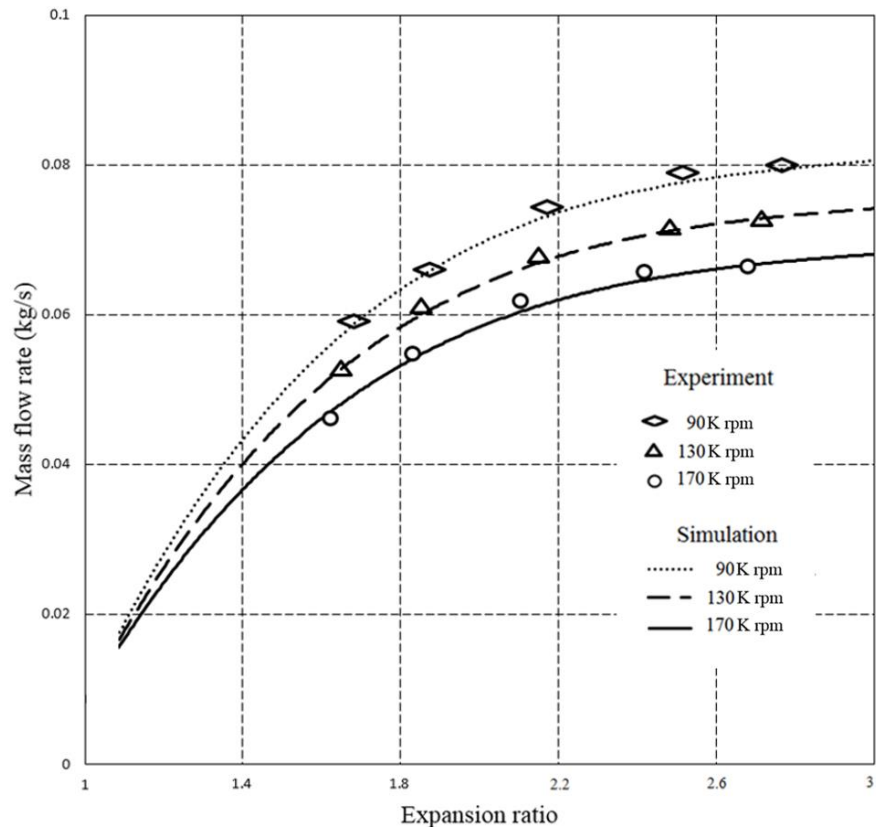


Figure 5.10 Validation of turbine expansion ratio with experimental data (50% opening)

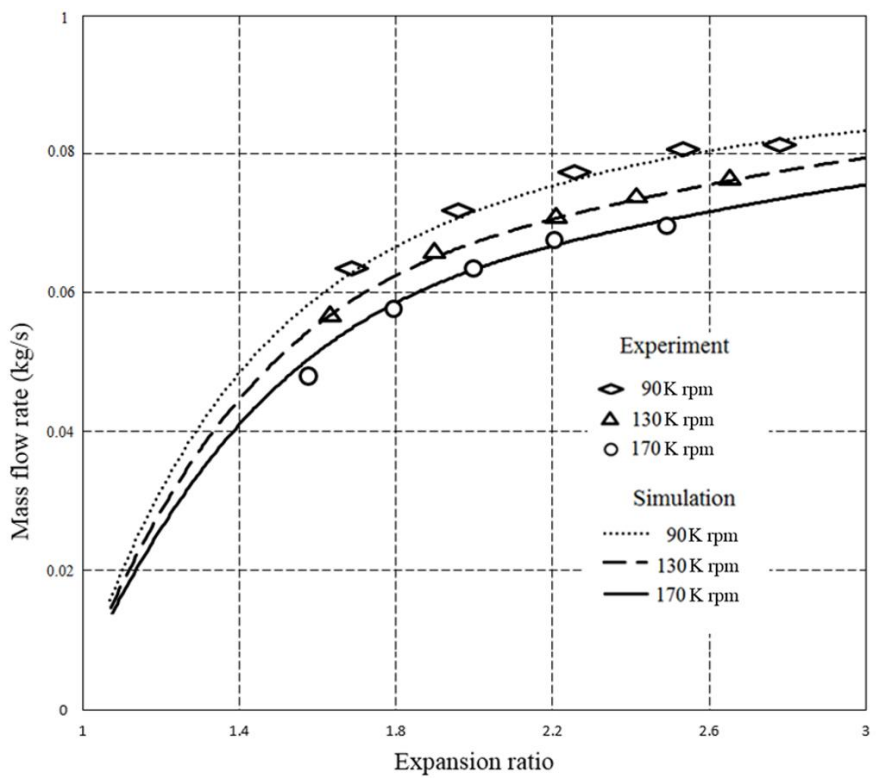


Figure 5.11 Validation of turbine expansion ratio with experimental data (80% opening)

5.5.2 Validation of Turbine Isentropic Efficiency

As shown in Figure 5.12, turbine isentropic efficiency with different expansion ratio at 20% opening of VNT was compared between simulation and experimental data. As simulation results have very good agreement with experimental results, it demonstrates that the developed turbine and turbocharger models are capable of simulating turbine and turbocharger performance with good accuracy.

As turbine isentropic efficiency has a peak value to expansion ratio, the trend is similar for all three turbocharger speeds. However, expansion ratios are different at peak efficiency for different rotational speeds. The higher the turbocharger speed, the higher expansion ratio where the peak isentropic efficiency is achieved.

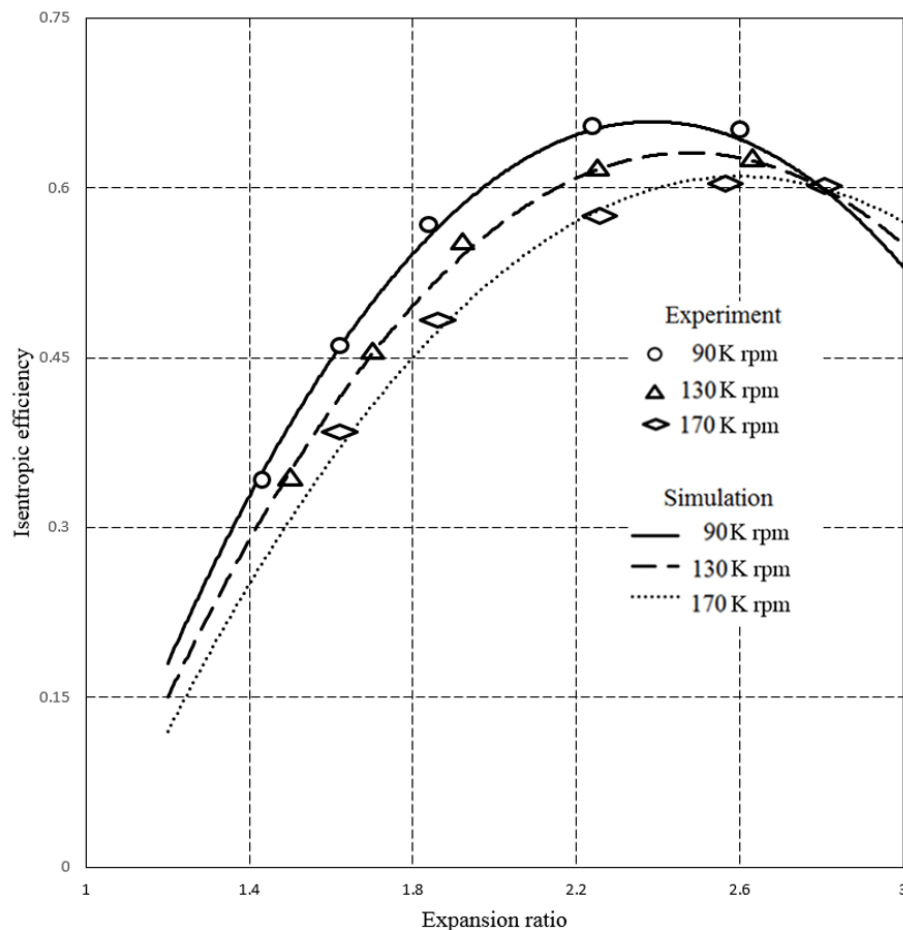


Figure 5.12 Validation of turbine isentropic efficiency with experimental data (20% opening)

Figures 5.13 and 5.14 shows variations of turbocharger isentropic efficiency as a function of expansion ratio with 50% and 80% openings of VNTs. For 50% opening, the peak efficiency was higher than the one with 20% opening. By increasing the VNT opening, the effect of turbine rotational speed was less significant than the one with 20% opening.

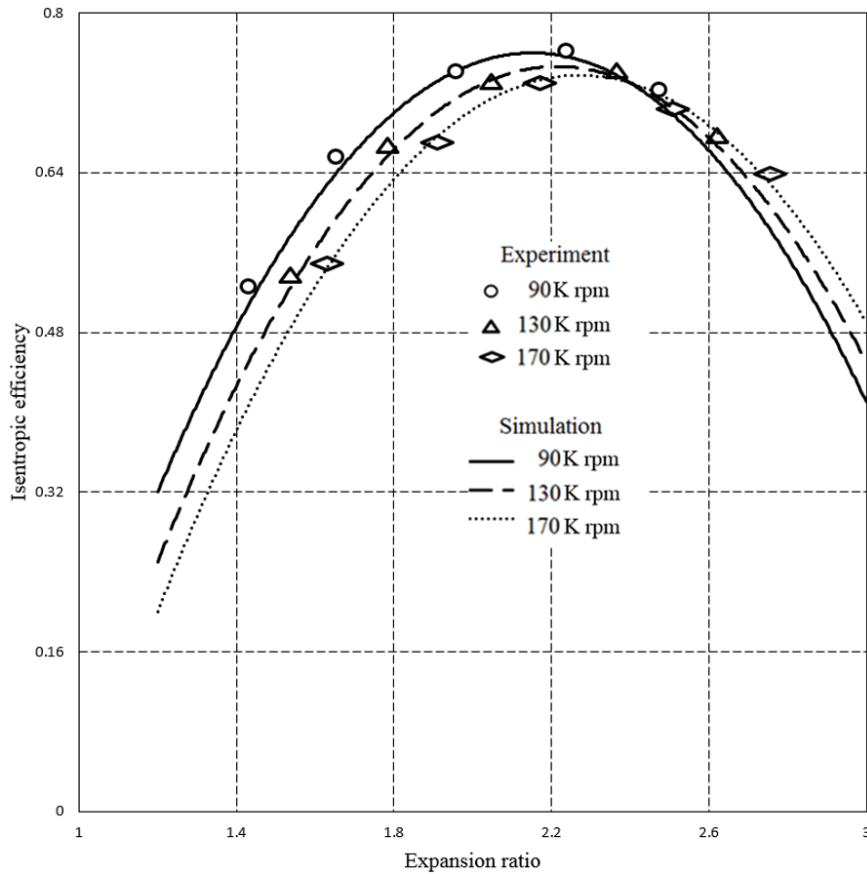


Figure 5.13 Validation of turbine isentropic efficiency with experimental data (50% opening)

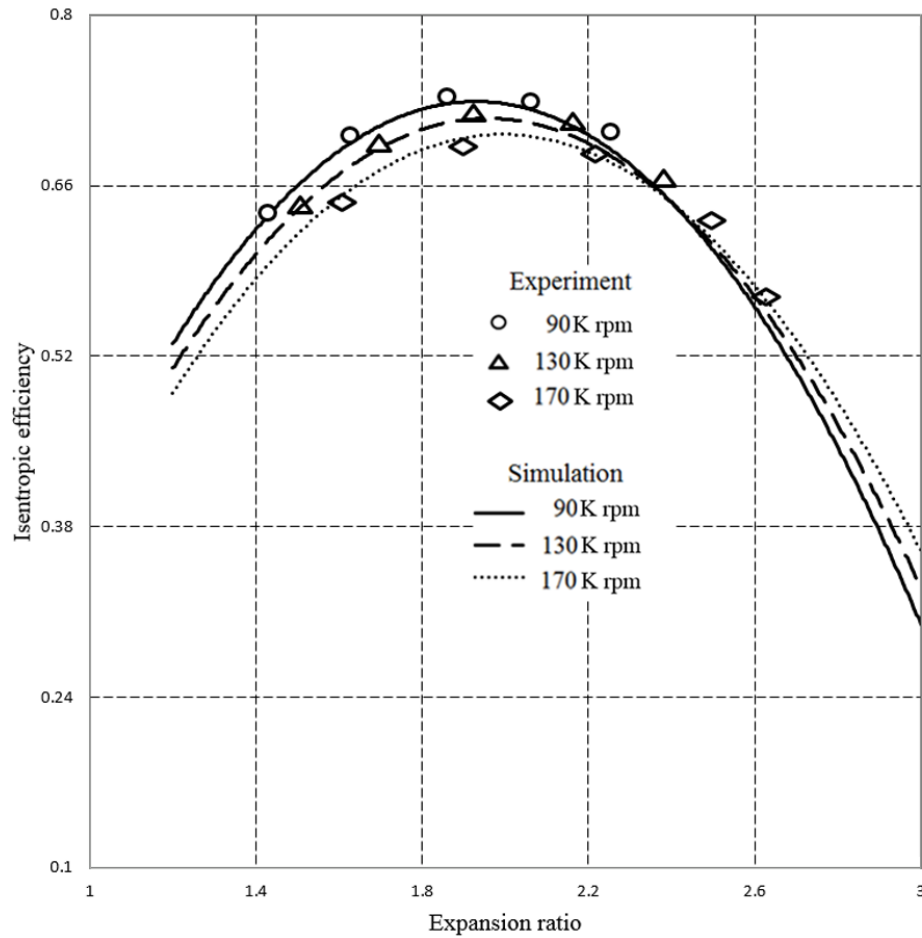


Figure 5.14 Validation of turbine isentropic efficiency with experimental data (80% opening)

5.6 Summary

In this chapter, a turbine model has been demonstrated which is particularly used to predict the characteristics of VNT with different opening positions. It can be used to be coupled with the compressor model described in Chapter 3 to form a complete turbocharger model. Similarly to the compressor model, the model is based on the thermodynamics and aerodynamics correlations within the turbine system. Flow was analysed thermodynamically and aerodynamically for each component of the turbine. Losses have also been considered to make the prediction more realistic. Component performance can be calculated by using the flow governing equations and loss analysis, and the overall turbine performance can be estimated with all the key flow parameters known in each component especially at the inlets and exits of each component.

Then the turbocharger model was validated by comparing the results from the simulation against the experimental data of a VNT with three different opening conditions. Three different rotational speeds were used for each opening condition of the VNT. The characteristics used for comparison are the expansion ratio against mass flow rate and isentropic efficiency. As shown from the results, for all three different openings with three different rotational speeds, the simulation had very good agreement with the experimental data. It was concluded that the model developed was capable of predicting the performance of a VNT with those three different opening positions with good accuracy.

Chapter 6 Optimisation of the Performance of Variable Nozzle Turbochargers (VNT)

6.1 Introduction

In Chapter 5, the performance of turbine with different openings of variable nozzle turbochargers (VNT) has been validated with experimental data. The next objective of this research is to optimise the performance of VNT which can be investigated through simulations using the proposed 1D model.

6.2 The Effects of VNT on Turbine Performance

Figure 6.1 shows the turbine characteristics with three different VNTs openings at the same rotational speed: 20%, 50% and 80% opening.

As shown in the figure, the case with 20% opening of VNTs provided an expansion ratio around 1.8 while both the cases with the other two openings of VNTs provided an expansion ratio less than 1.4. It indicates that higher expansion ratio can be achieved by applying VNTs.

On the other hand, the flow capacity with 80% opening of VNTs is much higher than the case with 20% opening of VNTs at high expansion ratio. For small VNT opening, the turbine will be choked at high engine speeds with high mass flow rate. In that case, the turbocharger will have high pressure at the exit with high associated losses and therefore the power output will be reduced.

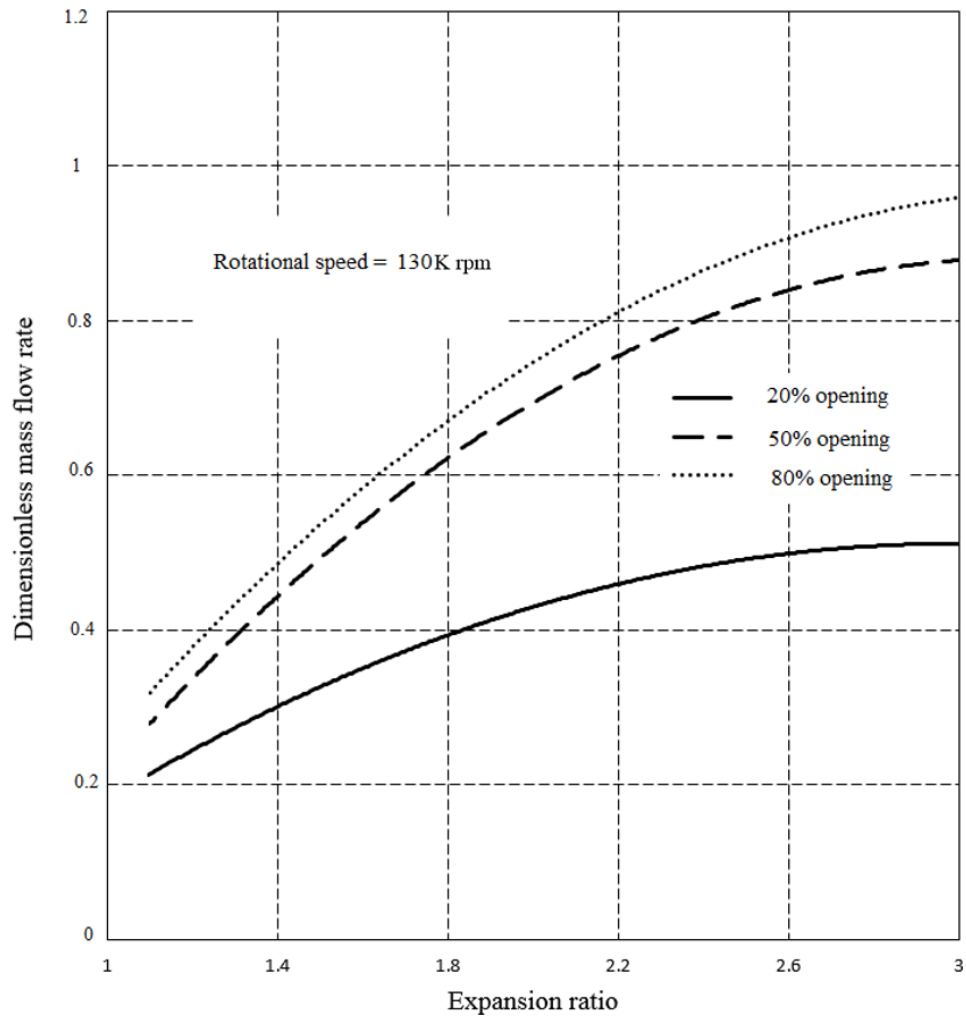


Figure 6.1 Turbine dimensionless performance map at different VNT opening

6.3 The Effects of VNT on Turbine Isentropic Efficiency

The turbine isentropic efficiency characteristics with three different VNT openings are shown in Figure 6.2.

It can be seen that optimum turbine efficiency of the VNT happens with an intermediate opening position which is due to the design of aerodynamics. At 20% VNT opening, turbine isentropic efficiency is lower than other VNT openings due to higher flow velocity and Mach number at nozzle and impeller inlet and hence lower turbine efficiency.

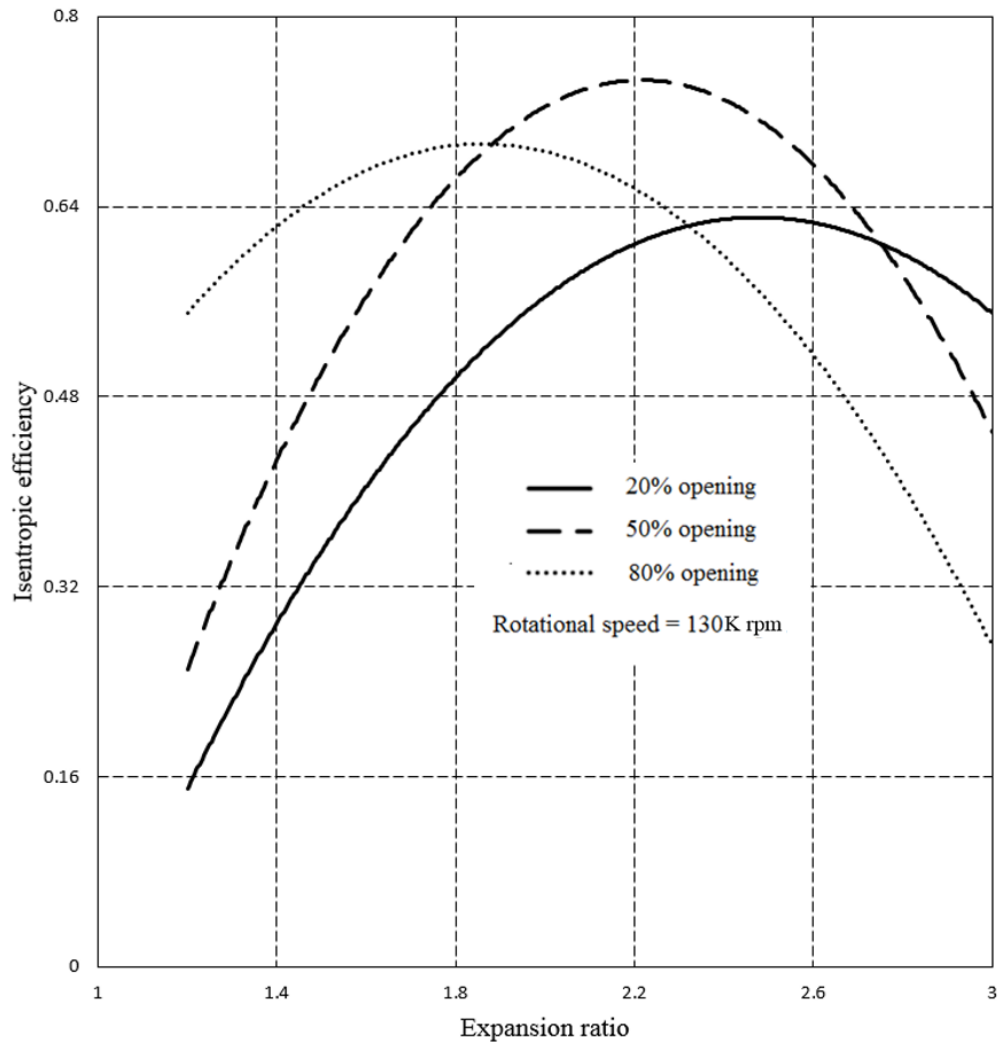


Figure 6.2 Turbine isentropic efficiency at different VNT openings

However, smaller VNT opening provides higher expansion ratio and higher turbocharger power at low mass flow rate (low engine speed). It also means that smaller VNT opening provides quicker transient response and higher boost pressure, which is the biggest advantage of variable nozzle turbocharger against fixed geometry turbocharger. Turbine isentropic efficiency at 80% VNT opening is not optimal because larger flow could cause higher loss. The detailed analysis of effects of loss mechanisms in turbine on its isentropic efficient will be discussed next.

6.4 Investigation of Losses in Turbine under Different VNT Opening

The losses with different VNT openings can affect the expansion ratio. However, they all have similar characteristics by increasing rotational speed at different van positions. Therefore, the loss characteristics for different VNT openings are compared with a rotational speed of 130K rpm.

6.4.1 Rotor Skin Friction Loss

In Figure 6.3, it shows rotor skin friction loss under different VNT opening.

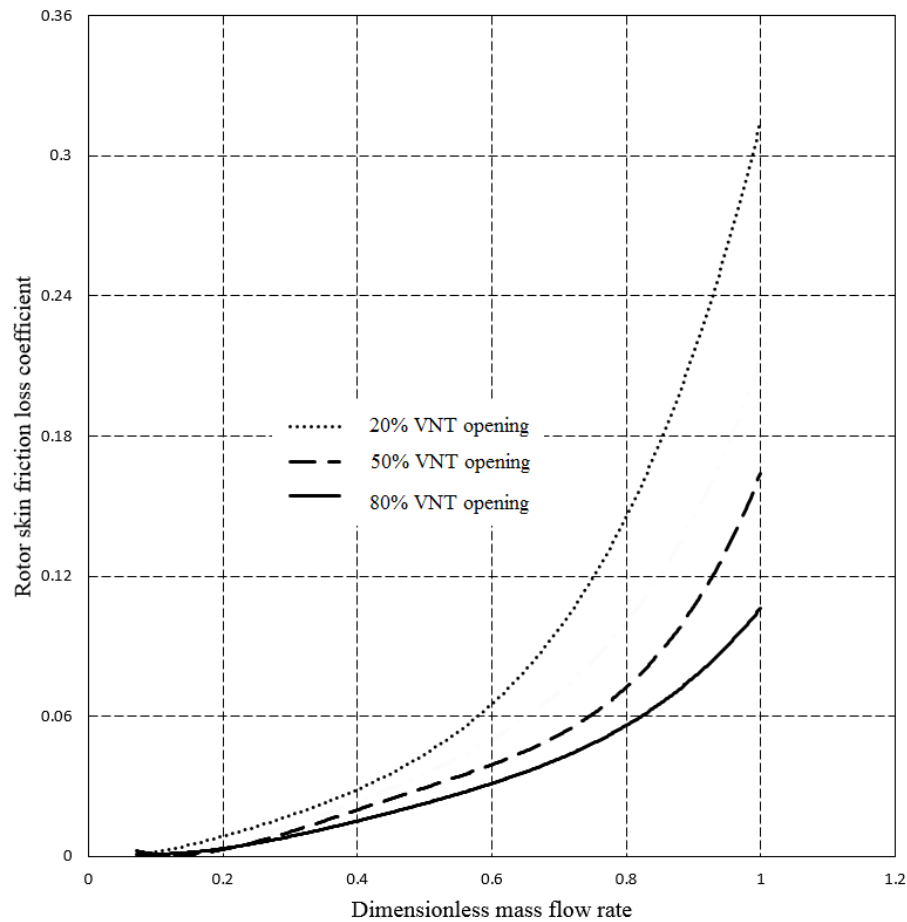


Figure 6.3 Rotor Skin Friction Loss at different VNT openings

It can be seen that the loss increases as the mass flow rate increases for all three different VNT openings. The case with 20% VNT opening shows higher skin friction loss, compared with other VNT openings. The reason for that is the increased mass flow rate indicating increased mean velocity component. As mentioned in chapter 4, skin friction loss is directly dependent on the mean velocity. The physics behind it is similar for turbines. Meanwhile, higher flow velocity exists in rotor at 20% VNT opening due to the flow expansion in nozzle. It is well known that friction loss is correlated with the surface roughness therefore smooth rotor surface could reduce rotor skin friction loss.

6.4.2 Mixing Loss

In Figure 6.4, it shows rotor mixing loss under different VNT opening.

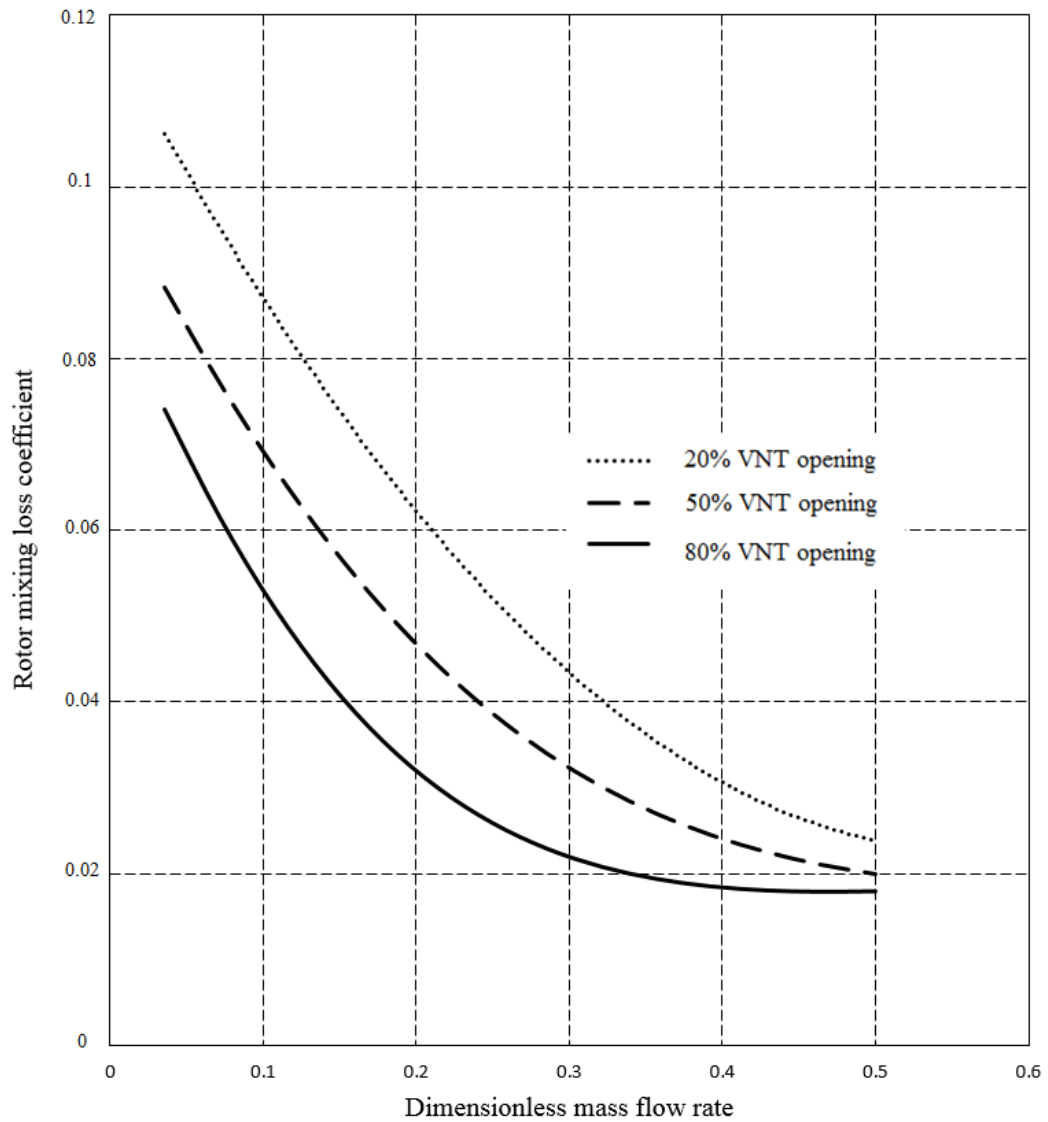


Figure 6.4 Rotor Mixing Loss at different VNT openings

It can be seen that rotor mixing loss decreases with the increase in mass flow rate. As mentioned before, mixing loss is dependent on the magnitude of the wake flow, which is a function of the fraction of wake flow area. It is stated that jet flow area increases with increasing mass flow rate but wake flow area decreases. The case with 80% VNT opening delivers more mass flow than other two VNT openings, which explains that rotor mixing loss is less for larger VNT opening.

6.4.3 Impeller Blade Loading Loss

In Figure 6.5, it shows rotor mixing loss under different VNT opening.

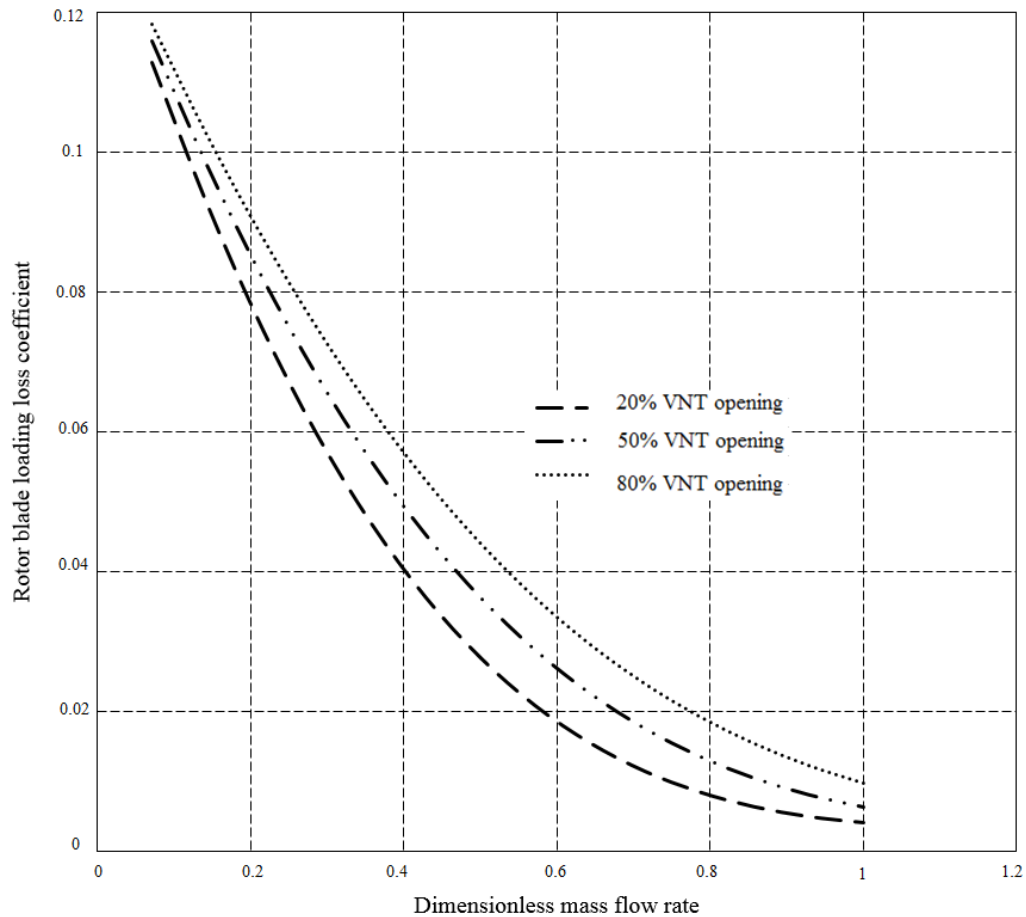


Figure 6.5 Rotor Blade Loading Loss at different VNT openings

It can be seen that rotor blade loading loss decreases with an increasing mass flow rate. Rotor blade loading loss at 80% VNT opening is higher than other VNT openings. The physics behind it could be that rotor blade loading loss coefficient depends on diffusion factor. Relative flow velocities at both inlet and exit will be increased by increasing the mass flow rate. However, the tangential impeller speed at the exit has more influence on the relative velocity at the exit. Meanwhile, 80% VNT opening delivers more mass flow than other two VNT openings.

6.4.4 Nozzle Skin Friction Loss

Different from compressor, skin friction loss in nozzle should be considered, especially for Variable Nozzle Turbines. The investigation of losses in nozzle will be helpful to understand VNT effect on improving turbocharger performance. Figure 6.6 shows nozzle skin friction loss with different VNT openings.

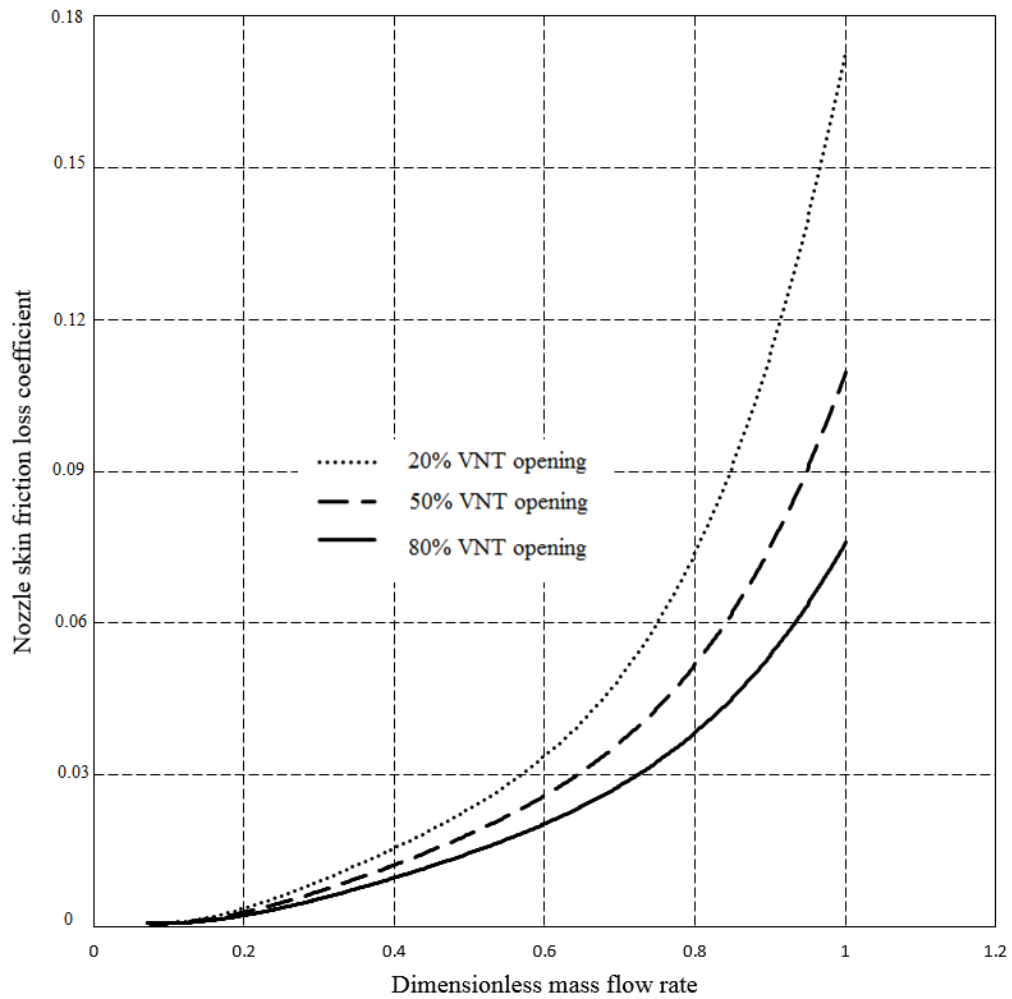


Figure 6.6 Nozzle Skin Friction Loss at different VNT openings

It can be seen that rotor blade loading loss increases when mass flow rate goes up. Nozzle friction loss at 20% VNT opening is higher than other VNT openings. The physics behind it could be that skin friction loss is directly dependent on the mean velocity, and increase mass flow rate gives quicker flow in nozzle. Moreover, flow expands at higher level in nozzle with 20% VNT opening. As a result, 20% VNT opening deliveries flow at highest velocity for a given mass flow rate. Similarly, nozzle skin friction loss coefficient also depends on surface roughness, which should be born in mind for nozzle designer.

6.4.4 Rotor Incidence Loss

Rotor incidence loss plays an important role during the investigation of Variable Nozzle Turbocharger performance. It is known that variable VNT opening directly changes flow angle and velocity at nozzle exit as well as rotor inlet. As mentioned before, rotor incidence loss is correlated with flow angle at rotor inlet. Rotor incidence loss with different VNT openings can be seen in

Figure 6.7.

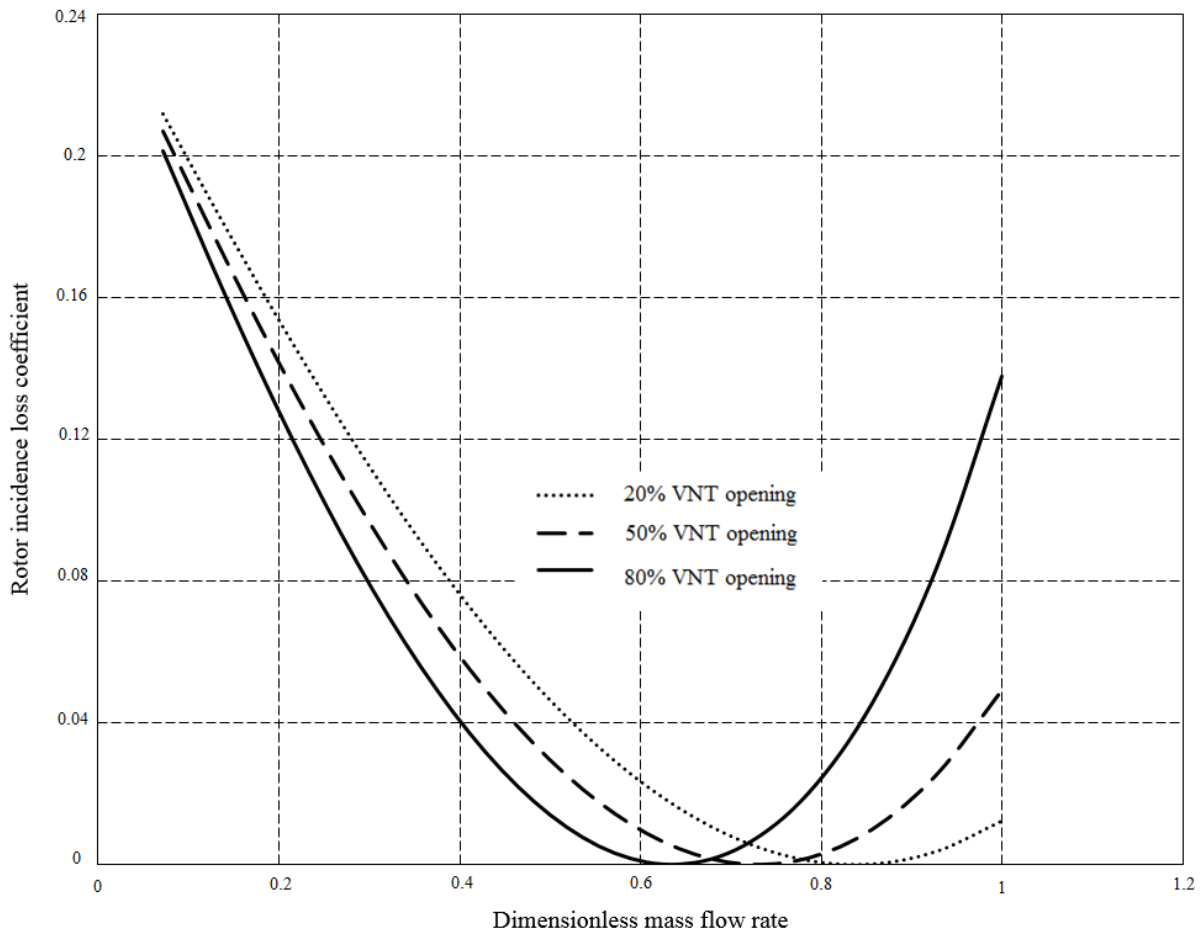


Figure 6.7 Rotor Incidence Loss at different VNT openings

As shown in the figure, rotor incidence loss coefficient characteristics has similar trend for all three VNT openings investigated. With low mass flow, rotor incidence loss coefficient was the highest due to the low axial velocity. It decreased with the increase of the mass flow. It reached a value of 0 with a dimensionless mass flow rate of approximately 0.65, 0.75 and 0.85 for the cases with 80%, 50% and 20% of VNT openings respectively indicating that the flow angle aligned with the rotor blade profile. It then increased sharply towards the choke line of the rotor. For a given rotational speed, rotor incidence loss under 20% VNT opening is different from 80% VNT opening. The physics behind it could be that variable VNT opening changes the flow angle and velocity at rotor inlet. As rotor blade angle is always fixed, rotor incidence loss will changes with variable VNT openings together with different operating conditions.

6.5 Investigation of Rotor Inlet Velocity under Different VNT Opening

Understanding different loss mechanisms in centrifugal compressor is very helpful to improve turbine efficiency by reducing losses. However, the investigation of correlations between rotor inlet velocity and VNT openings as well as correlation between flow angle and VNT openings is very helpful to get visual understanding of the flow in a Variable Nozzle Turbocharger. The correlation between rotor inlet velocity and VNT openings is shown in Figure 6.8.

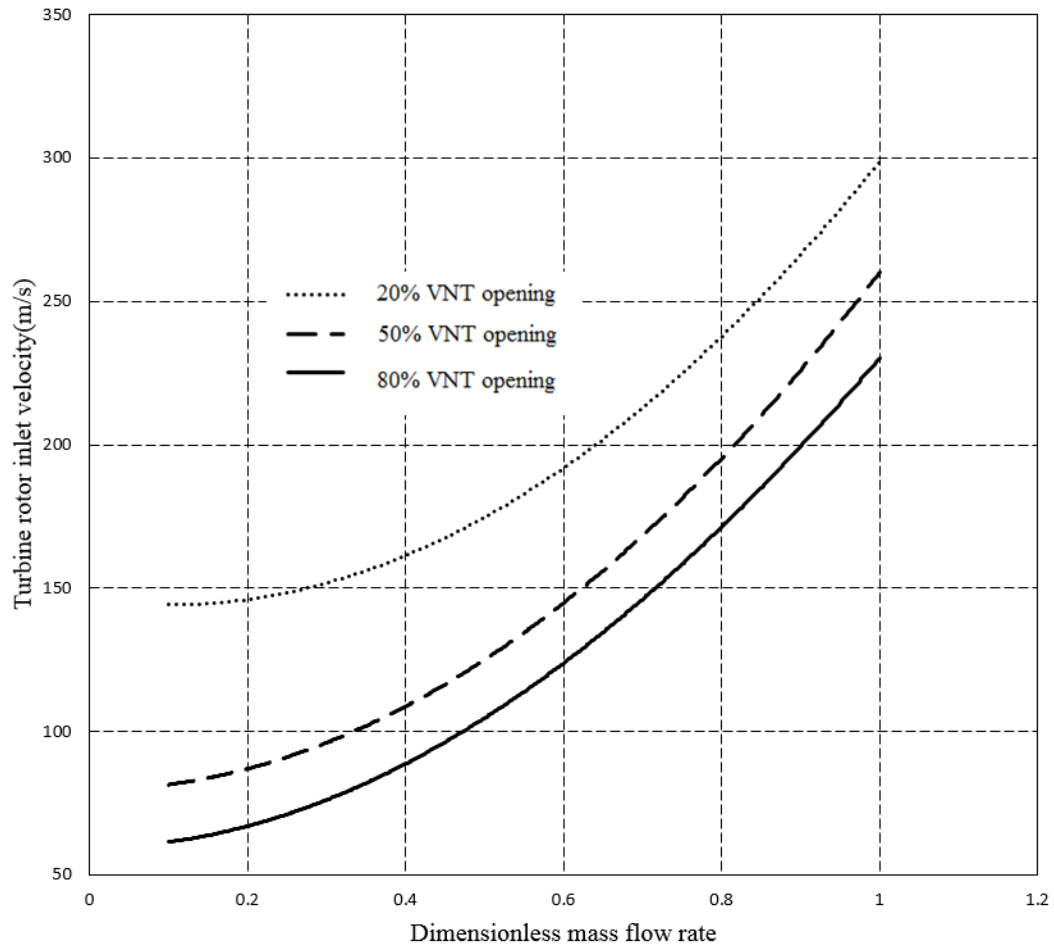


Figure 6.8 Rotor Inlet velocity at different VNT openings

It can be seen that flow velocity at rotor inlet increases when mass flow rate goes up. Moreover, flow velocity at rotor inlet at 20% VNT opening is higher than other VNT openings. The physics behind it could be flow in nozzle expands more at 20% VNT opening. With decreasing nozzle opening, flow will get higher velocity at the expense of lower pressure. It is known that flow velocity at rotor inlet is related with nozzle exit velocity and circumferential speed which is proportional to rotor rotational speed. For a given mass flow rate and rotational speed, velocity at rotor inlet is only correlated with nozzle exit velocity, which is in inverse proportional to nozzle opening.

6.6 Investigation of Flow Angle at Rotor Inlet under different VNT opening

In Figure 6.9, it shows correction between flow angle at rotor inlet and VNT openings.

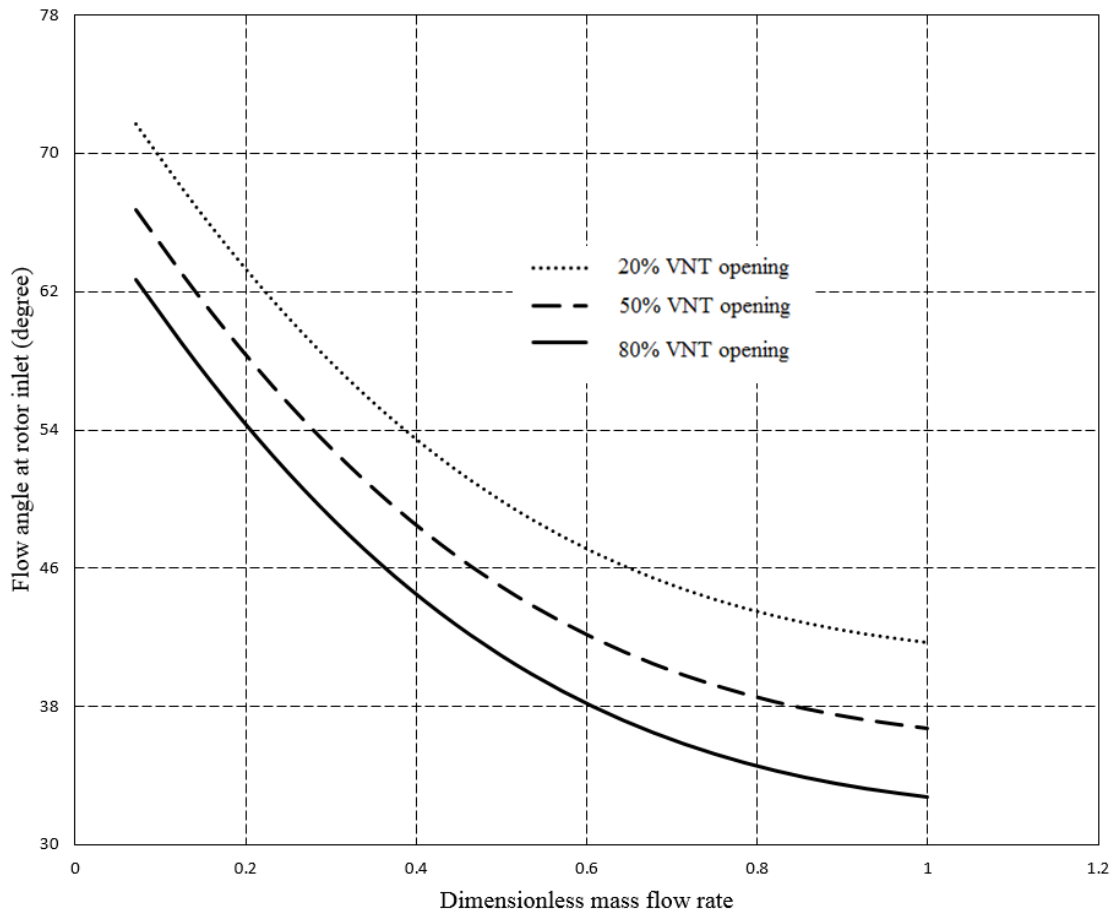


Figure 6.9 Rotor Inlet Flow Angle at different VNT openings

It can be seen that flow angle at rotor inlet shows a decreasing trend when mass flow rate goes up. Flow angle at rotor inlet at 20% VNT opening is larger than other VNT openings. The physics behind it could be that flow in nozzle expands in different level for different nozzle opening. With decreasing nozzle opening area, flow will exit nozzle at higher velocity at the expense of lower pressure. It is known that flow angle at rotor inlet has an inverse relationship with the radial component of nozzle exit velocity.

6.7 Summary

In this chapter, VNT turbine performance was investigated with the developed turbine model described in Chapter 5. Results shows different vane opening has higher effects on turbine

expansion ratio and isentropic efficiency with those small vane openings (for instance around 20%). By analysing variation of various losses with vane opening under different mass flow rate, it demonstrates that effects of vane opening on losses has no obvious different under different vane opening.

In terms of the influence of vane opening on flow velocity and flow angel at the turbine rotor inlet, results show that under low mass flow rate, closing vane opening has bigger influence to the flow velocity at the turbine rotor inlet. The flow angle keeps decreases with mass flow rate with almost linear trend, though the reduction gets small under high mass flow rate. Those information will be important for VNT turbine performance optimization at design stage and calibration stage.

Chapter 7 Implementation of Developed Turbocharger Model Coupled with AVL-BOOST Engine Model

In this chapter, the proposed turbocharger model described in Chapter 5 was coupled with AVL BOOST one dimensional engine model to check its feasibility for modelling the whole engine system. In the environment of AVL BOOST, turbine and compressor map data generated by the proposed turbocharger model was embedded with the 1D engine model developed by AVL-BOOST simulation software. 1D engine simulation allows the prediction of engine performance from any generic configuration. The simulation of a complete engine model can be carried out in a comparatively short time with high accuracy. With 1D engine model, the performance of a turbocharged diesel engine were assessed by coupled simulation. The performance of turbocharger model was also investigated in both cyclic and steady-state simulations.

7.1 AVL-BOOST Engine Model

7.1.1 Model Description

The 1D engine model in environment of AVL BOOST was built based on a Ford 2.0 L four-cylinder DI (Direct Injection) diesel engine. As shown in Figure 7.1, the turbocharger model (marked as TC1 in Figure 7.1) developed in this study was directly coupled in the air path. The output from air box and upstream air intake pipe were inputs for the compressor model. Then the outcome from the compressor was added into engine intake manifold, and then into the main engine cylinder and combustion model. At exhaust side, exhaust gas flow performance was used for the input of the turbine model. The output of the turbine model was linked with after treatment system and other general engine exhaust components.

The dimensions of air path pipes and plenums in this 1D model were based on the relevant pipes and manifolds of an actual Ford engine.

The heat release characteristics over crank angle were defined by the Vibe model [130], which is shown in the equation 7.1. There are four parameters that will affect the heat release behaviour of the cylinder in Vibe model which are the start of combustion, combustion duration, shape parameter m , and parameter a . In order to get accurate simulation results, these parameters have to be carefully validated according to different engine speeds.

$$\frac{dx}{d(\frac{\Phi}{\Phi_z})} = C (m+1) \left(\frac{\Phi}{\Phi_z}\right)^m e^{-C\left(\frac{\Phi}{\Phi_z}\right)^{m+1}}$$

$$dx = \frac{dQ}{Q} \quad (7.1)$$

Where

Q is the heat input of total fuel, (J)

Φ is the angle between initial and current time of the simple Vibe function, (degree)

Φ_z is the duration angle of the simple Vibe function (degree)

m is Vibe function shape parameter,

C is Vibe function parameter, $C = 6.9$ for completer combustion, and

x is cumulative normalized heat released (mass fraction burned).(J/kg)

Figure 7.2 shows the visualization of the compressor map data in the environment of AVL BOOST. The map data was output from the developed turbocharger model.

Table 7.3 shows the values of these parameters used in this model for different engine speeds. The fuelling rate was set differently at different engine speed, in accordance with the fuelling setting in the ECU of a real engine.

Valve lifts and timings as other main air path parameters significantly affect the air scavenge behaviour of an engine, which in turn affects the performances of the engine. Figure 7.3 shows the lift and timing of intake and exhaust valves defined according to the engine manual.

In Figures 7.4 and 7.5, it shows the turbine characteristic map of mass flow rate against turbine efficiency and pressure ratio at different turbine rotational speeds. Those results are produced from the 1D AVL BOOST model coupled with the developed turbocharger model.

Table 7.2 Combustion parameters settings for different engine speeds.					
Engine speed, rpm	Fuelling, mg/cycle	Start of combustion, deg	Combustion duration, deg	Shape parameter m	Parameter a
1000	17.7	1.2	41.2	1.04	6.9
1400	22.02	1.2	52.2	0.92	6.9
1800	25.1	-1.3	64.1	0.85	6.9
2200	24.08	-1.3	73.2	0.84	6.9
2600	23.12	-3.5	80.1	0.83	6.9
3000	23.2	-4.2	86.4	0.78	6.9
3400	22.43	-1.1	90.2	0.68	6.9
3600	22.36	-0.2	91.3	0.64	6.9

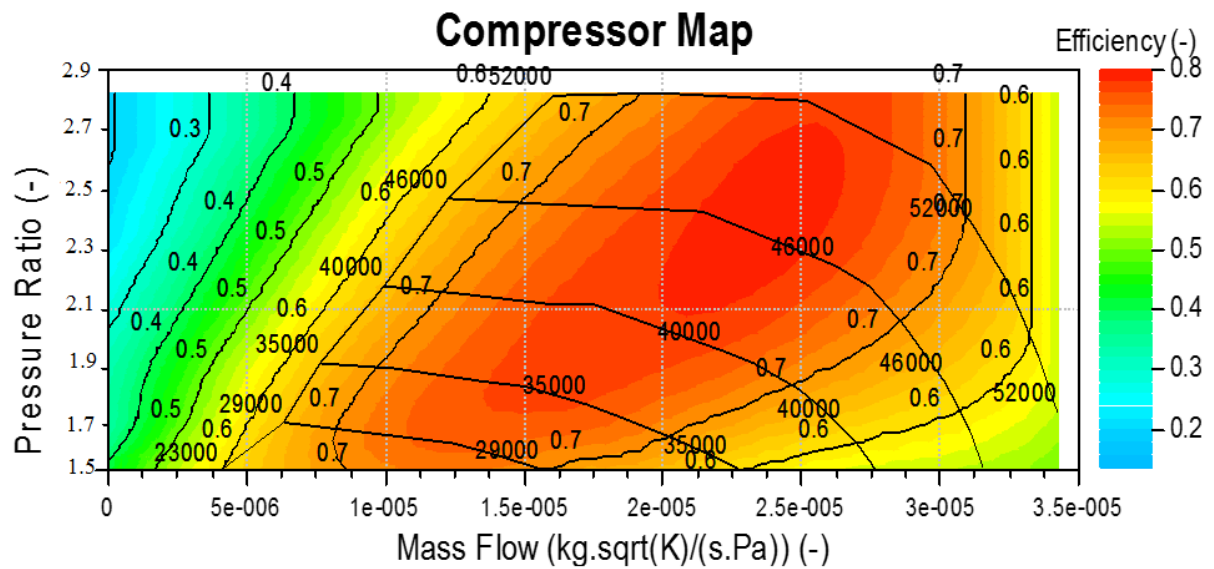


Figure 7.2 Compressor map visualization in AVL BOOST environment

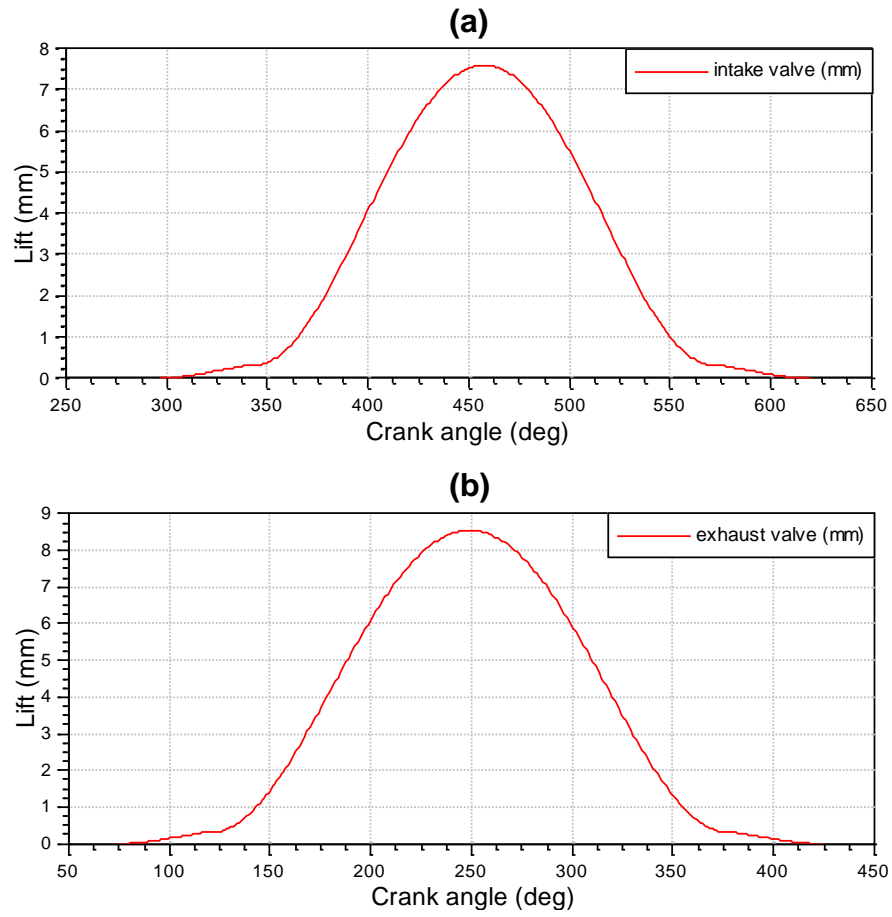


Figure 7.3 Valve lifts for intake valve and exhaust valve.

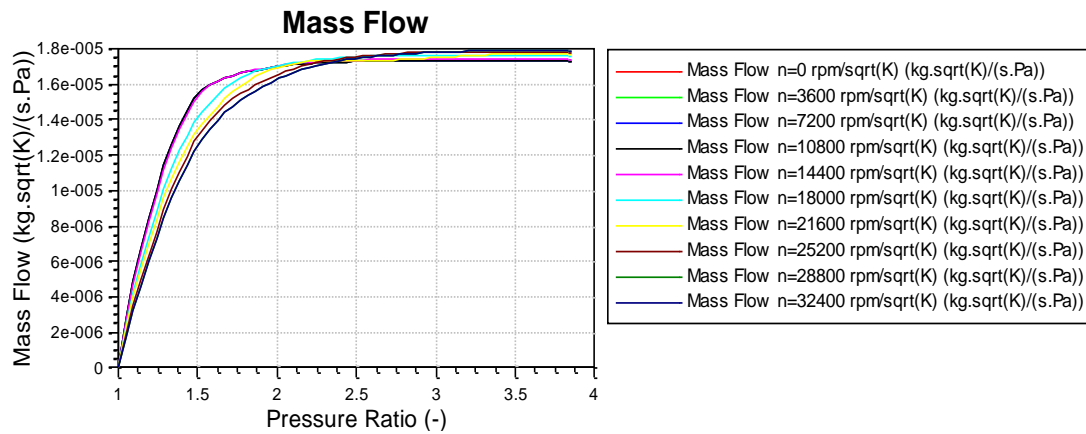


Figure 7.4 Turbine mass flow at different turbine speed.

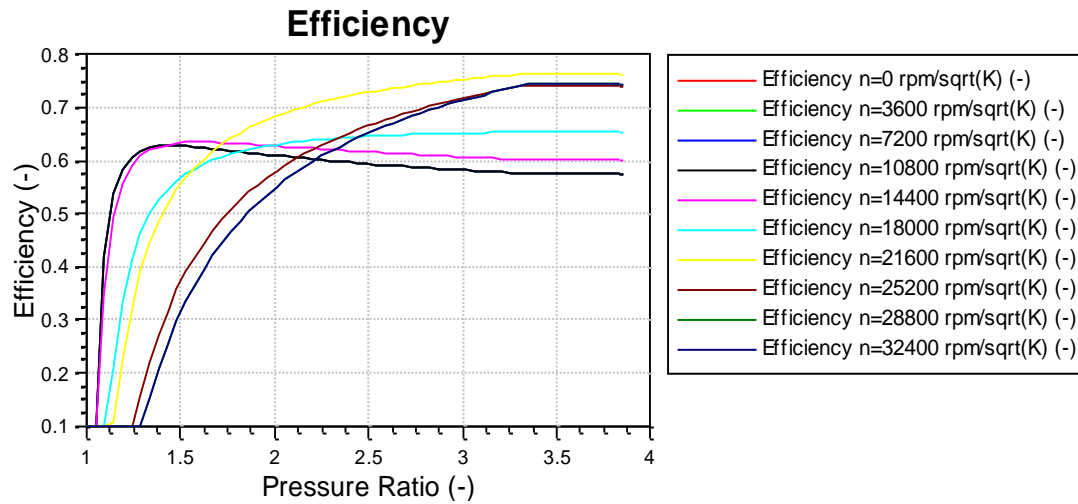


Figure 7.5 Turbine efficiency at different turbine speed.

7.1.2 Model Validation

After the AVL BOOST engine model was initially coupled with the developed turbocharger model, the whole 1D model was validated against experimental results. Figures 7.6 and 7.7 show comparisons between simulation results and experimental results including boost pressure and intake air flow rate at different engine speeds. As can be seen that it has good agreement between the simulation results and the experimental data.

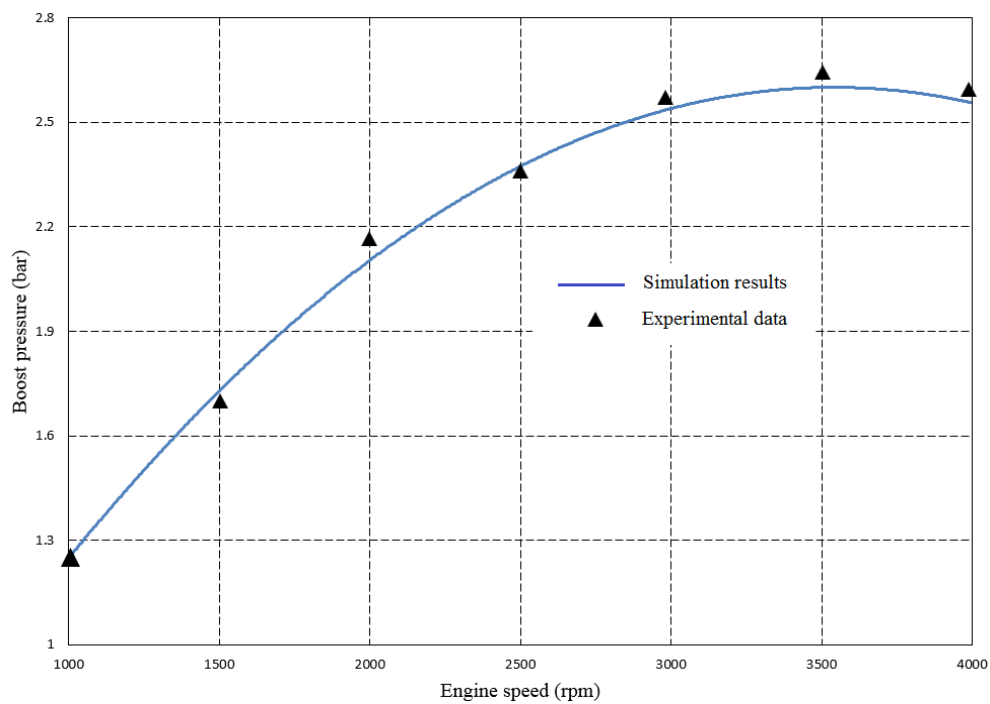


Figure 7.6 Boost pressure validation with experimental data

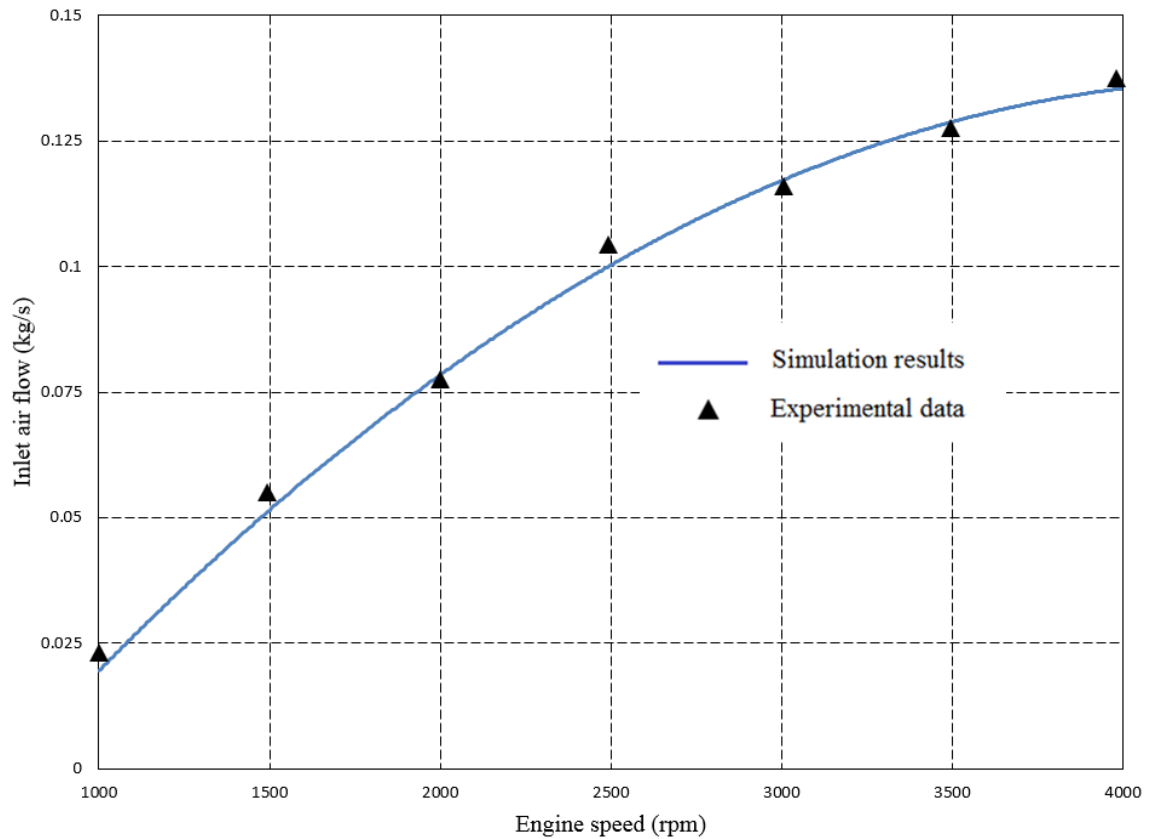


Figure 7.7 Intake air flow validation with experimental data

7.2 Simulation Results

7.2.1 Cyclic Simulation at 3000rpm

The cyclic simulation was performed with one complete engine cycle, which has a crank angle of 720 degree. This allowed the turbocharger and the engine performance to be investigated in detail during each engine cycle.

Figure 7.8 (a) indicates that four cylinders were firing at the predefined sequence. The pressure peak for each cylinder represents the self-ignition happened in each cylinder. Figure 7.8 (b) shows the in-cylinder temperature of cylinder 1 started to drop shortly after the self-ignition and further dropped at the end of exhaust stroke around 340 CA degrees. Figure 7.8 (c) shows the in-cylinder mass started to drop at the beginning of the exhaust stroke and started to increase from the beginning of the intake stroke, and Figure 7.8 (d) shows the valve lifts for intake and exhaust valve respectively for all four cylinders. The red curve shows the intake valve lift and the green one shows exhaust valve lift.

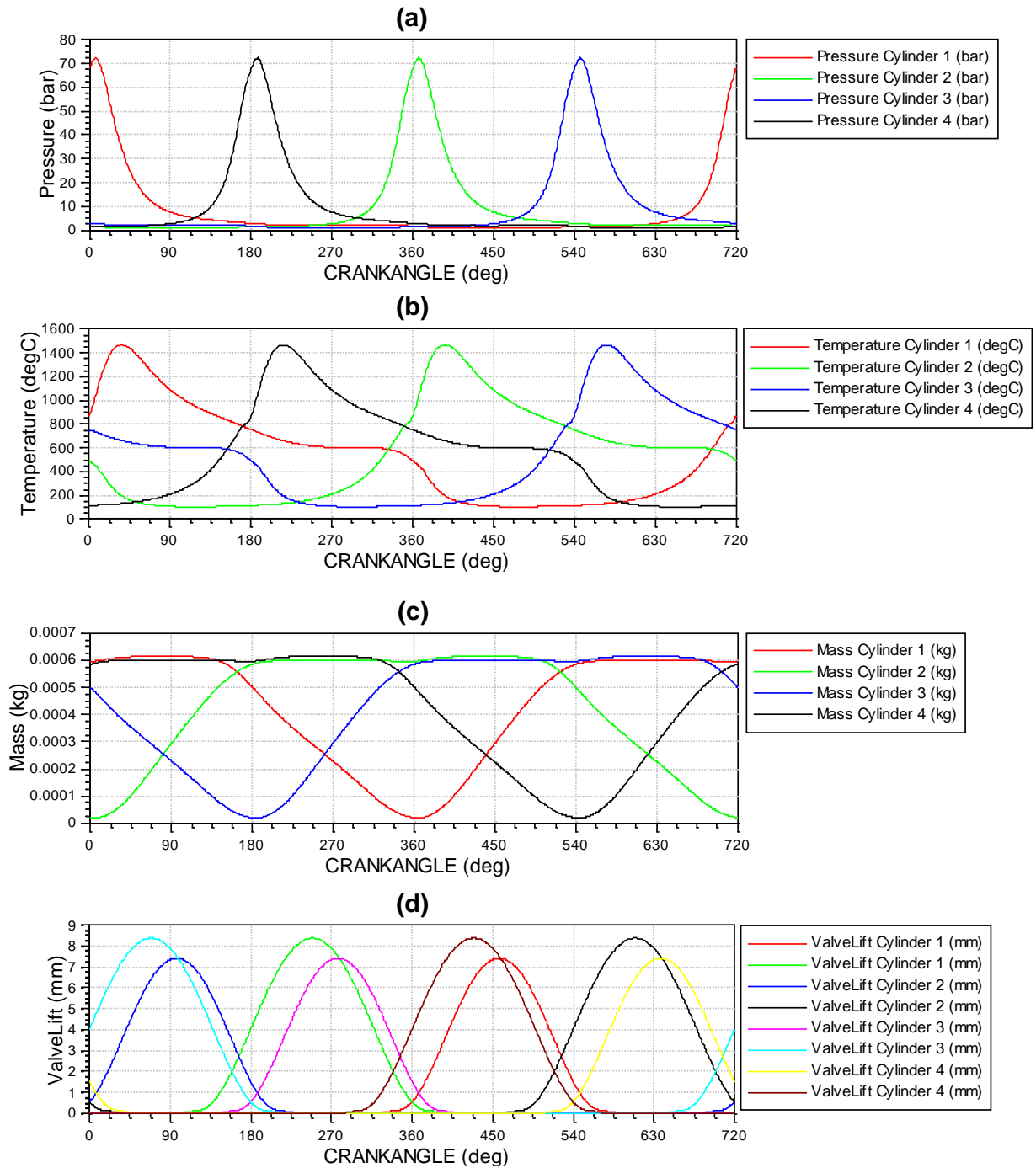


Figure 7.8 In-cylinder simulation results during one complete engine cycle at 3000 rpm.

In-cylinder pressure, (b) in-cylinder temperature, (c) in-cylinder air mass, (d) valve lifts for intake and exhaust valve.

In Figure 7.9, compressor and turbine power and efficiency are presented. In Figure 7.9 (a), the compressor power started to increase after the peak power point of the turbine. There is a similar trend for compressor efficiency curve which is shown in Figure 7.9 (b). Figure 7.9 (c) shows that the turbine power curve has a local power peak at each firing of the cylinders, and the efficiency

curve also has a local efficiency peak at the same point, as shown in Figure 7.9 (d).

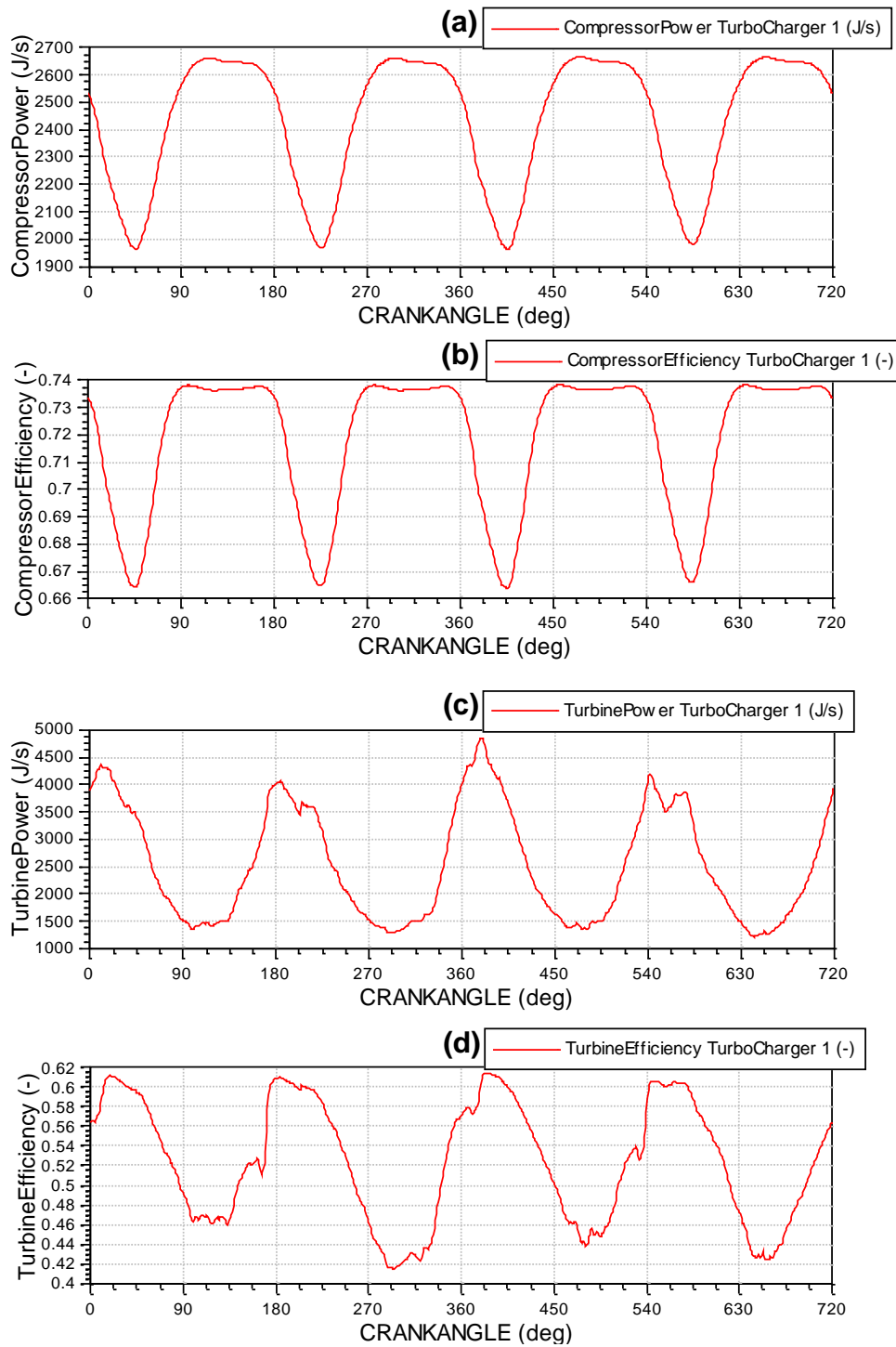


Figure 7.9 Turbocharger performance simulation results during one complete engine cycle at 3000 rpm.

(a) Compressor power, (b) compressor efficiency, (c) turbine power, and (d) turbine efficiency.

7.2.2 Steady-State Simulation Results

Steady-state simulation was performed at one steady operating point of the engine with different engine speeds. Figure 7.10 (a) and (b) shows the results for the case with a speed of 1800 rpm, the engine aspirated the most amount of air and injected the most amount of fuel, and the air/fuel ratio is approximately 24 which shows in Figure 7.10 (c) and (d) indicated that the BSFC was at its lowest at 1800 rpm.

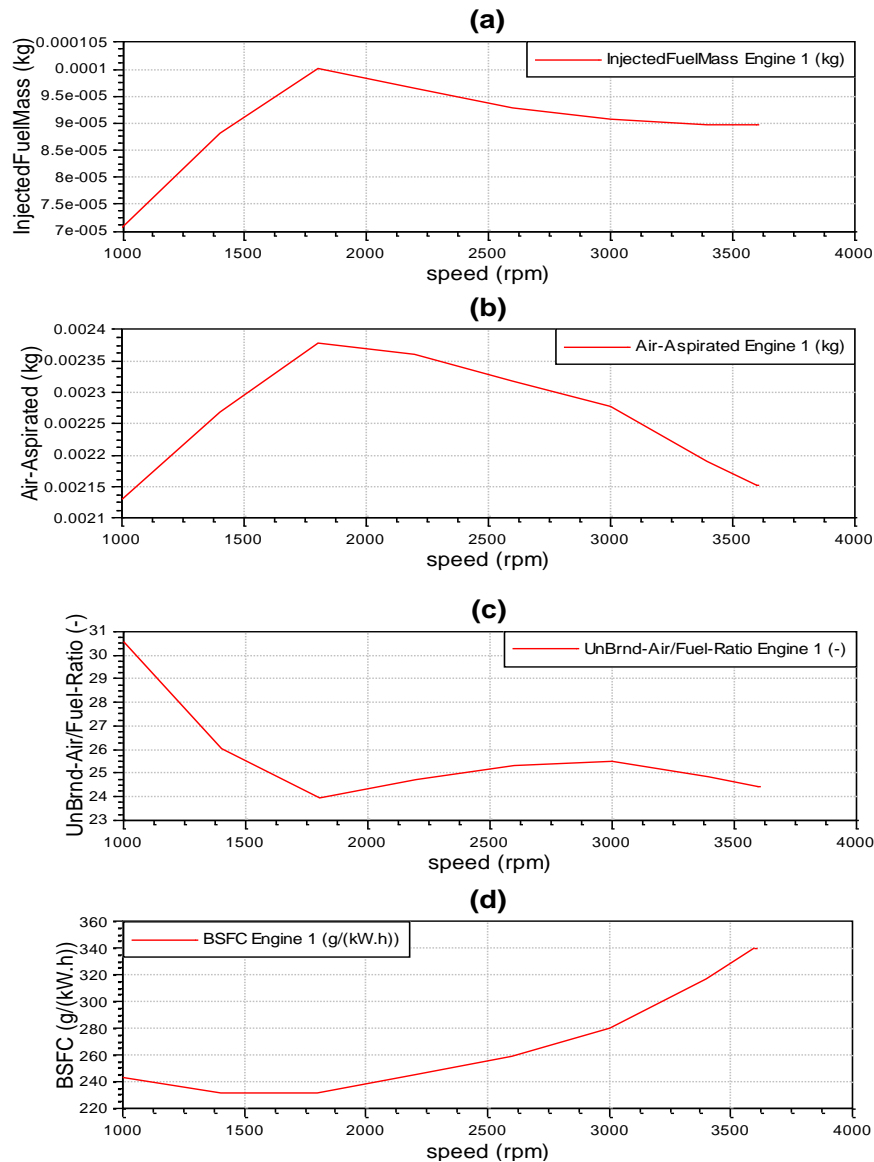


Figure 7.10 Steady-state simulation results at several engine speeds range from 1000 rpm to 3600 rpm.

(a) Total injected fuel mass per cycle, (b) total aspirated air mass during one cycle, (c) air/fuel ratio, and (d) brake specific fuel consumption.

Figures 7.11 and 7.12 show the rotational speed, work, efficiency, and boost pressure of the compressor and the work, and the ratio of the turbine increased with the engine speed. However,

Figure 7.12 (b) shows that the turbine efficiency was highest at an engine speed of 1800 rpm.

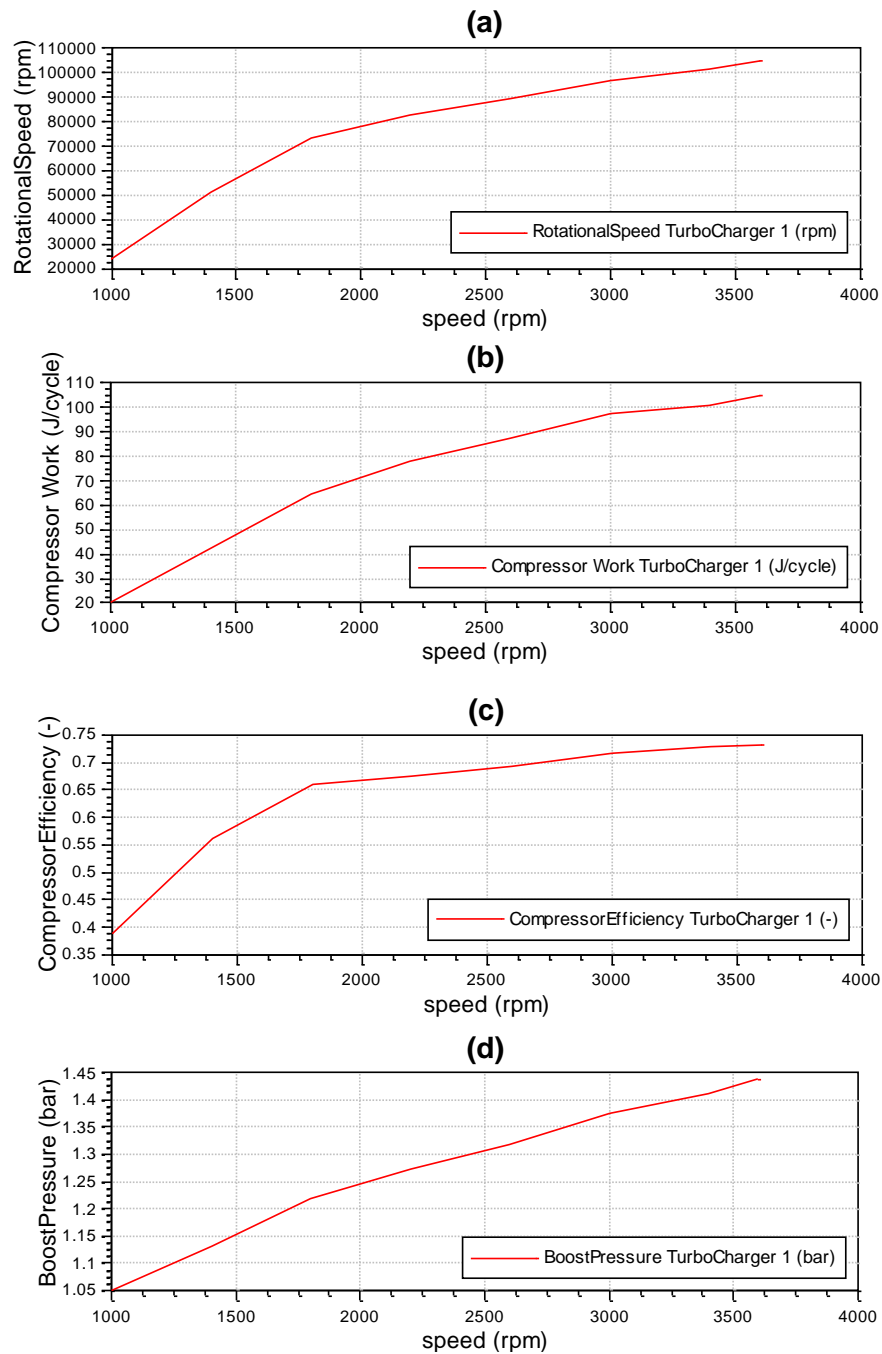


Figure 7.11 Steady-state simulation results of the compressor at different engine speeds range from 1000 rpm to 3600 rpm.

(a) Compressor rotational speed, (b) compressor work, (c) compressor efficiency, and (d) compressor boost pressure to the engine.

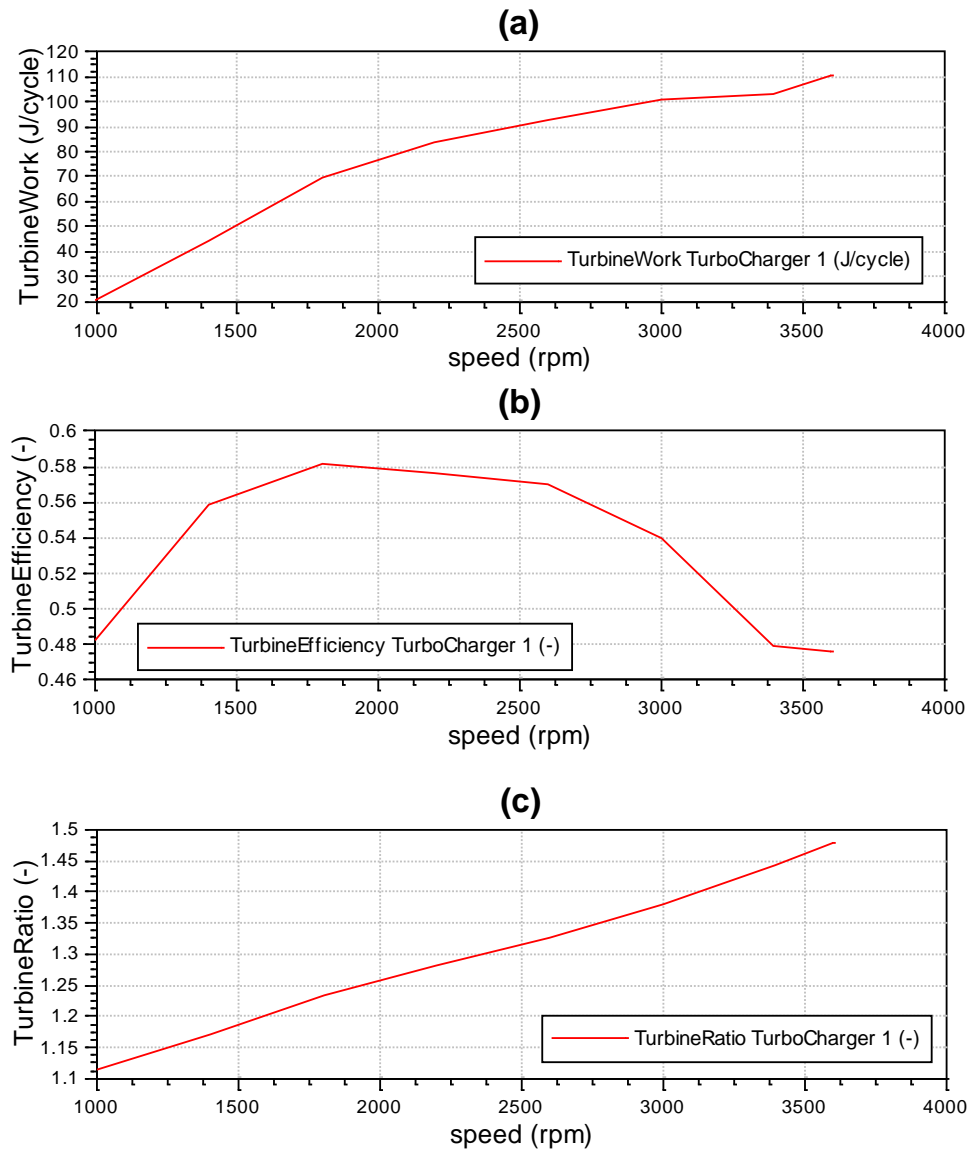


Figure 7.12 Steady-state simulation results of the turbine at different engine speeds range from 1000 rpm to 3600 rpm.

Turbine work, (b) turbine efficiency, and (c) turbine ratio.

7.3 Summary

The developed turbocharger model described in previous chapters has been applied into an engine model by coupling turbocharger model with AVL BOOST engine model. Simulation results of boost pressure and intake air flow rate at different engine speeds have been validated against experiment data and shows good agreement. Simulation was also investigated to study the adaptability of the developed turbocharger model, under both cyclic and steady-state simulation conditions. Results show that performance of turbocharged diesel engines could be assessed with acceptance results for required parameters.

Chapter 8 Conclusions and Recommendations for Future Work

8.1 Conclusions

In this thesis, One-dimensional (1D) compressor and turbine models based on thermodynamics have been developed to predict performance of turbochargers. The compressor model has taken all the losses in each component of the compressor into account for the performance prediction. Through analysis, it was clear that the most of pressure rise was achieved in impellers compared with other components in the compressor system. Where there were barely changes in pressure in volute and it is commonly used to direct the flow.

For the impeller sub model, there are nine losses which could affect compressor performance have been modelled. Several losses degrade compressor performance remarkably such as skin friction loss, incidence loss, mixing loss and blade loading loss. Other losses contribute less for compressor performance degradation such as entry diffusion loss, clearance loss, blade loading loss, hub to shroud loading loss and blockage loss. However, all these losses contributed to the compressor characteristics map.

Two main losses which are skin friction loss and diffusion loss are considered in the vaneless diffuser sub-model. For the vaned diffuser sub-model, three more types of losses were added which are incidence loss, blockage loss and wake mixing loss with the elimination of the diffusion loss. The losses considered in the volute sub-model were the meridional velocity loss, tangential velocity loss and skin friction loss. Through analysing different types of losses in different component of the compressor, it is very helpful for the designers to determine the dominating losses for each component and the whole compressor system. Then that information can be used to inform the new design with less loss in order to improve compressor performance.

The proposed compressor model has been validated with experimental results collected from a 2.0 L turbocharged diesel engine testbed. It showed that the simulation results from this one dimensional compressor model matches experimental data very well.

Effects of all losses on compressor performance have been investigated and presented in one chart, and all dominating losses have been clarified. It shows that the ideal compressor performance map without any losses should be a straight line but different losses could change the compressor characteristics. Individual Loss analysis has also been performed for all dominated losses in compressor, which provides better understanding of each individual loss

mechanism. The effect of mass flow rate and rotational speed on different losses has also been investigated. The results have been presented and discussed in detail. The relationship between velocity triangles and mass flow rate has been investigated in order to get visual understanding of flow in compressor.

The one-dimensional (1D) turbine model has been constructed in a similar way as the compressor model. Then the turbine model has been modified to investigate Variable Nozzle Turbine performance. The proposed model has simulated Variable Nozzle Turbine performance with three nozzle openings: 20%, 50% and 80%. The simulation results match with experimental data very well for each VNT opening position respectively. Predicted turbine performance map clearly showed that variable nozzle turbines can generate more expansion ratio at low mass flow rate, compared with fixed nozzle turbines.

Several losses dominating turbine performance degradation have been investigated to find out how Variable Nozzle Turbine improves turbocharger performance. Simulation results show that a smaller variable nozzle opening contributed to lower turbine efficiency due to the higher flow velocity and Mach number at the nozzle and impeller inlet, even though a smaller variable nozzle opening provides quicker transient response and higher boost pressure. As a result, the optimum turbine efficiency of Variable Nozzle Turbocharger occurs at an intermediate opening due to the aerodynamic design of the turbine stage. The investigation of rotor inlet velocity and flow angle has been performed in order to get visual understanding of flow in Variable Nozzle Turbocharger.

Finally, the proposed compressor model and variable nozzle turbine model have been coupled with AVL BOOST one dimensional engine model to check its feasibility for modelling the entire engine system. Simulation results of boost pressure and intake air flow rate at different engine speeds have been validated against experiment data and results showed good agreement.

8.2 Future work

The followings are recommended for future work:

- Improve the compressor model to further cope with predicting performance for generic compressor configurations in turbochargers.
- Improve the current turbine model to suit twin-entry turbocharger modelling.
- Two-stage turbocharging modelling should also be considered in near future.

Further developments of the turbocharger model could enable it to query a database of existing

components in order to define a turbocharger system that precisely targets a specification of performance characteristics supplied by the end user.

References

- [1] <http://www.sacarfan.co.za/2012/10/turbocharged-vehicles-heading-for-40-percent-market-share>.
- [2] Stone, R, Introduction to Internal Combustion Engines, ISBN 0-333-74013-0, Palgrave, 1999.
- [3] Silva C, Ross M, Farias T. Analysis and simulation of “low-cost” strategies to reduce fuel consumption and emissions in conventional gasoline light-duty vehicles. *Energy Convers Manage*, 215–22, 2009.
- [4] Kesgin U. Effect of turbocharging system on the performance of a natural gas engine. *Energy Convers Manage*, 46(1):11–32, 2005.
- [5] Marcello C, Fabio C, Giorgio R and Yue-Yun W, Design and Validation of a Control-Oriented Model of a Diesel Engine with Two-Stage Turbocharger, SAE Paper 2009-24-0122, 2009.
- [6] Chacartegui R, Sánchez D, Muñoz A, Sánchez T. Real time simulation of medium size gas turbines. *Energy Convers Manage*, 52(1):713–24, 2011.
- [7] Srinivasan.C, Sayooj M.S, Increasing the Efficiency of an Engine by the use of Variable Geometry Turbochargers. *International Journal of Innovative Research in Science, Engineering and Technology*, Volume3, Special Issue 4, April 2014
- [8] Baines N, Hajilouy-Benisi A, Yeo JH. The pulse flow performance and modelling of radial inflow turbines. In: *Proceedings of the IMechE 5th international conference on turbocharging and turbochargers*. C484/006/94; PP209–218, 1994.
- [9] Watson N, Janota M.S, Turbocharging the Internal Combustion Engine, MacMillan, New York, 1982.
- [10] David J, Turbomachinery Performance Modelling, SAE Paper 2009-01-0307, 2009.
- [11] Leduc, P., Dubar, B., Ranini, A., and Monnier, G., “Downsizing of Gasoline Engines: an Efficient Way to Reduce CO₂ Emissions”, *Oil and Gas Science and technology - Rev. IFP*, Vol. 58 (2003), No. 1, pp. 115-127.
- [12] <http://www.eea.europa.eu/data-and-maps/indicators/energy-efficiency-and-specific-co2-emissions/energy-efficiency-and-specific-co2-3>
- [13] Petitjean, D., Bernardini, L., Middlemass, C., Shahed, S., “Advanced Gasoline Engine

Turbocharging Technology for Fuel Economy Improvements,” SAE Technical Paper 2004-01-0988, 2004, doi:10.4271/2004-01-0988.

[14] Capobianco, M., Gambarotta, A. - “Variable geometry and waste-gated automotive turbochargers: measurements and comparison of turbine performance”, ASME Transactions, Journal of Engineering for Gas Turbines and Power, Vol. 114, 553-560, 1992.

[15] Winkler, N., Angstrom, H-E., “Simulations and Measurements of a Two-Stage Turbocharged Heavy-Duty Diesel Engine including EGR in Transient Operation,” SAE Technical Paper 2008-01-0539, 2008, doi: 10.4271/2008-01-0539.

[16] <https://www.avl.com/-/avl-aggressively-downsized-diesel-engine>

[17] Ralf P. Schulz, et al., The new 1.0l Supercharger Zetec RoCam Engine, SAE Paper 2002-01-3438, 2002.

[18] Leonard, O., Adam, O., “A Quasi-One Dimensional CFD Model for Multistage Turbomachines”, Journal of Thermal Science, Vol. 17, No.1 (2008).

[19] Silvia M and Massimo C, Steady and pulsating flow efficiency of a waste- gated turbocharger radial flow turbine for automotive application, Energy, Vol.36, PP.459-465, 2011.

[20] Hojin J, Hyomin J, Seibum C and Minseok K, Modeling and Control of Single Turbocharger with High Pressure Exhaust Gas Recirculation Diesel Engine, SAE Paper 2013-01-2649, 2013.

[21] Muzaffar A.Q, Vikas D and Shakti S, Development of Two-stage Turbocharger System for Off Road Application Diesel Engine in Order to Achieve 75 HP, SAE Paper 2013-01-2749, 2013.

[22] Springer S, Trevor S. Wilson, Hongming X, Simon C, Steve R, Mirosław L. Wyszynski and Jacek Misztal, Modelling and Experimental Investigations of Supercharged HCCI Engines, SAE Paper 2006-01-0634, 2006.

[23] Nicola T and Ricardo M, Experimental Efficiency Characterization of an Electrically Assisted Turbocharger, SAE Paper 2013-24-0122, 2013.

[25] Bandel, W., Fraidl, G., Kapus, P., Sikinger, H., “The Turbocharged GDI Engine: Boosted Synergies for High Fuel Economy Plus Ultra-low Emission,” SAE Technical Paper 2006-01-1266, 2006, doi:10.4271/2006-01-1266.

[26] Akiko K, Yukio T, Takaaki K and Fusayoshi N, Variable Geometry System Turbocharger

- for Passenger Car Diesel Engine, SAE Paper 2001-01-0273, 2001.
- [27] Petitjean D, Bernardini L, Middlemass C, Shahed SM. Advanced Gasoline engine turbocharging Technology for fuel economy Improvements. SAE Paper 2004-01-0988; 2004.
- [28] Chiong M.S, Rajoo S, Ricardo F, Costall A.W. Engine turbocharger performance prediction: One-dimensional modelling of a twin entry turbine, *Energy Conversion and Management*, Vol.57, PP.68-78, 2012.
- [29] Srithar R, Alessandro R, Ricardo F, Unsteady performance analysis of a twin-entry variable geometry turbocharger turbine, *Energy*, Vol.38, PP.176-189, 2012.
- [30] Hajilouy-Benisi A, Shahhosseini M, Flow and performance characteristics of twin-entry radial turbine under full and extreme partial admission conditions, *Archive of Applied Mechanics*, Vol.79, PP.1127-1143, 2009.
- [31] Aghaali H, Effect of Swirl on the intake of Turbocharger, *Iranian Journal of Science & Technology Transaction B - Engineering*, Vol.32, No. B6, PP.571-584, 2008.
- [32] Mohammed H, Miloud A, Sid L, Investigation of the mixed flow turbine performance under inlet pulsating flow conditions, *Comptes Rendus Mecanique*, Vol.340, PP.165-176, 2012.
- [33] Nobuhiro I, Tohru O, Ryuji K, Satoshi A and Takaki M, Development of a 4-Cylinder Gasoline Engine with a Variable Flow Turbo-charger, SAE Paper 2007-01-0263, 2007.
- [34] Hidetsugu M, Kazuya M, Yuichi I, Shinya T, Kazuho A, Fusayoshi N, Superior Charging Technology by Screw Supercharger and High Technology Turbocharger for Automotive Use, SAE Paper 890455, 1989.
- [35] Basil U and Marian K, Optimization Procedure for Matching Exhaust Waste-Gate Turbocharger to Automotive Diesel Engine, SAE Paper 931102, 1993.
- [36] Ralf P, et al., The new 1.0l Supercharger Zetec RoCam Engine, SAE Paper 2002- 01-3438, 2002.
- [37] Loren H, John W, Supercharger versus Turbocharger in Vehicle Applications, SAE Paper 870704, 1987.
- [38] Fernando A, Ramon M, Sérgio M and José E, Automotive Turbocharger Maps Building using a Flux Test Stand, SAE Paper 2002-01-3542, 2002.
- [39] Arora B and Pathak D, Effect of Swirl on the intake of Turbocharger, SAE Paper 2008-28-0069, 2008.

- [40] Vávra J, Macek J, Vítek O, Michal Takáts, Investigation of Radial Turbocharger Turbine Characteristics under Real Conditions, SAE Paper 2009-01-0311, 2009.
- [41] Piscaglia F, Onorati A, Marelli S and Capobianco M, Unsteady Behavior in Turbocharger Turbines: Experimental Analysis and Numerical Simulation, SAE Paper 2007- 24-0081, 2007.
- [42] Moraal P and Kolmanovsky I, Turbocharger Modelling for Automotive Control Application, SAE Paper 1999-01-0908, 1999.
- [43] Shi X, Zhang R, Yu L, and Ma C, Experimental Investigation on the Unsteady Performance of Automotive Turbocharger Turbine, *Experimental Techniques*, Vol.2012, PP.1-9, 2012.
- [44] Abdelmadjid C, Mohamed S, Boussad B, CFD Analysis of the Volute Geometry Effect on the Turbulent Air Flow through the Turbocharger Compressor, *Energy Procedia* Vol.36, PP.746 -755, 2013.
- [45] Galindo J, Fajardo P, Navarro R, García L, Characterization of a radial turbocharger turbine in pulsating flow by means of CFD and its application to engine modelling, *Applied Energy*, Vol.103, PP.116-127, 2013.
- [46] Bozza F and Bellis V, Steady and Unsteady Modeling of Turbocharger Compressors for Automotive Engines, SAE Paper 2010-01-1536, 2010.
- [47] Hellstrom F and Fuchs L, New Approach to Turbocharger Optimization using 1-D Simulation Tools, *Proceedings of ASME*, GT2008-51088, 2008.
- [48] Cavalcanti R and Filho G, Automotive Turbocharger Radial Turbine CFD and Comparison to Gas Stand Data, SAE Paper 2011-36-0081, 2011.
- [49] Hajilouy A and Shahhosseini M, Empirical Assessment of the Performance Characteristics in Turbocharger Turbine and Compressor, *Experimental Techniques*, May/June 2010, PP.54-67, 2010, doi: 10.1111/j.1747-1567.2009.00542.x.
- [50] Mingxu Q, Chaochen M and Ce Y, Numerical Optimization on a Centrifugal Turbocharger Compressor, SAE Paper 2008-01-1697, 2008.
- [51] Spencer C, Elbert H, Sigurjon M and Allan B, Compact and Accurate Turbocharger Modelling for Engine Control, SAE Paper 2005-01-1942, 2005.
- [52] David J, Colin O, Peter K, William P and Eric K, Modelling and Manufacturing of Turbocharger Compressors, SAE Paper 2010-01-1219, 2010.

- [53] Prasad S, Dennis A, Aristotelis B, Philip K, David R and Michael B, Turbocharger Matching for a 4-Cylinder Gasoline HCCI Engine Using a 1D Engine Simulation, SAE Paper 2010-01-2143, 2010.
- [54] Oldrich V, Jan M and Milos P, New Approach to Turbocharger Optimization using 1-D Simulation Tools, SAE Paper 2006-01-0438, 2006.
- [55] Panagiotis G, Emanuel B, Lars B, Andreas B and Marc S, Advanced Turbocharger Model for 1D ICE Simulation - Part I, SAE Paper 2013-01-0581, 2013.
- [56] Bozza F, Gimelli F, Strazzullo L, Torella E, “Steady-state and Transient Operation Simulation of a ‘Downsized’ Turbocharged SI Engine”, SAE Paper no. 2007-01- 0381
- [57] Fontana G, Galloni E, “Knock Resistance in a Small Turbocharged Spark-Ignition Engine”, International Session – The Sustainable Mobility Challenge – of 61st ATI 2006 Congress, SAE n. 2006-01-2995.
- [58] GT-Power, User’s Manual and Tutorial, GT-SUITETM Version 6.0, March 2003, Gamma Technologies.
- [59] Wave, User’s Manual, 2002, Ricardo
- [60] Boost, User’s Manual, 2003, AVL
- [61] Dubitsky, O, Japikse, D, “Vaneless Diffuser Advanced Model”, ASME Transaction, Journal of Turbomachinery, 011020, Vol. 130, 2008.
- [62] Denton, J, Loss Mechanisms in Turbomachines, Journal of Turbomachinery, Vol. 115, Cambridge, pp. 621-656, 1993.
- [63] Mehdi N, Peter P and Berthold M, Physical Modelling of Automotive Turbocharger Compressor: Analytical Approach and Validation, SAE Technical Paper 2011- 01-2214.
- [64] Fabio B and Vincenzo D, 1D Simulation and Experimental Analysis of a Turbocharger Compressor for Automotive Engines under Unsteady Flow Conditions, SAE Technical Paper 2011-01-1147
- [65] Oh H, Yoon E and Chung M, An optimum set of loss models for performance prediction of centrifugal compressors, Proceedings of IMechE Part A, Vol.211, PP.331-337, 1997.
- [66] Barend W and Adriaan M, Determining the Impact of the different Losses on Centrifugal Compressor Design, R&D Journal, Vol. 21(3), PP.23-31, 2005.

- [67] Wei J, Jamil K, Roger A, Dynamic centrifugal compressor model for system simulation, *Journal of Power Sources*, Vol.158, PP. 1333–1343, 2006.
- [68] Bing H, Tan L, Cao S and Lu L, Prediction method of impeller performance and analysis of loss mechanism for mixed-flow pump, *Science China Technological Sciences*, Vol.55 No.7: 1988–1998, 2012.
- [69] Helen M, Development of A 1-D Performance Prediction Technique for Automotive Centrifugal Compressor, PhD Thesis, Loughborough University, 2006.
- [70] Cormerais M, Hetet J, Chesse P and Maiboom A, Heat Transfer Analysis in a Turbocharger Compressor: Modeling and Experiments, SAE Paper 2006-01-0023, 2006.
- [71] Westin F and Burenus R, Measurement of Interstage Losses of a Twostage Turbocharger System in a Turbocharger Test Rig, SAE Paper 2010-01-1221, 2010.
- [72] Mingyang Y, Xinqian Z, Yangjun Z and Zhigang L, Improved Performance Prediction Model for Turbocharger Compressor, SAE Paper 2008-01-1690, 2008.
- [73] Bozza F and Gimelli A, Unsteady 1D Simulation of a Turbocharger Compressor, SAE Paper 2009-01-0308, 2009.
- [74] Gravdahl J, Egeland O, Centrifugal compressor surge and speed control, *IEEE Trans. Control Syst. Technol.* 7 (September (5)), 1999.
- [75] Shadi G, Trevor S, Hongming X, Simon C, Steve R, Mirosław L and Jacek M, Modelling and Experimental Investigations of Supercharged HCCI Engines, SAE Paper 2006-01-0634, 2006.
- [76] Wilson D, The Design of High-Efficiency Turbomachinery and Gas Turbines, The MIT Press, 1984
- [77] Ferguson T, The Centrifugal Compressor Stage, Butterworths, London, UK, 1963.
- [78] Lakshminarayana R, Fluid Dynamics and Heat Transfer of Turbomachinery, John Wiley and Sons, Inc., 1995.
- [79] Whitfield A, Wallace F, Study of incidence loss models in radial and mixed-flow turbomachinery, in: *Proceedings of the Congress of Heat Fluid Flow in Steam and Gas Turbine Plant*, University of Warwick, Coventry, UK, PP. 122–132, 1993.
- [80] Nisenfeld, A, Centrifugal compressors: principles of operation and control. Instrument society of America, 1982.

- [81] Sepulchre R, and Kokotovic P, Shape signifiers for throttle control of a low-order compressor model, 1996
- [82] Wang H and Kristić M, Control of deep hysteresis compressors under limited actuator bandwidth. In: Proceedings of the 1997 International Conference on Control Applications. Hartford, CT. PP657-662, 1997.
- [83] White, F (1986). Fluid mechanics. 2nd edition. McGraw-Hill. New York.
- [84] Strub R, Bonciani L, Borer C, Casey M, Cole S, Cook B, Influence of the Reynolds number on the performance of centrifugal compressors. Journal of turbomachinery, 109, 1987.
- [85] Balj, O, A contribution to the problem of designing radial turbomachines. Transactions of the ASME 74, PP451-472, 1952.
- [86] Cumpsty, N, Compressor Aerodynamics. 1st edition. Essex: Longman Scientific & Technical. 509 p, 1989.
- [87] Jansen, W, A method for calculating the flow in a centrifugal impeller when entropy gradients are present. Institution of Mechanical Engineers, Royal Society Conference on Internal Aerodynamics (Turbomachinery) : 133 - 146, 1967.
- [88] Lee S, Lee K, Song S, Chun K, Low pressure loop EGR system analysis using simulation and experimental investigation in heavy-duty Diesel engine. Int J Automotive Technol, 7(6):659–66, 2006.
- [89] Ugur K, Study on the design of inlet and exhaust system of a stationary internal combustion engine. Energy Convers Manage;46:2258–87, 2005.
- [90] Rakopoulos C, Giakoumis G, Development of cumulative and availability rate balances in a multi-cylinder turbocharged indirect injection diesel engine. Energy Convers Manage, 38(4):341–69, 1997.
- [91] Vincenzo D, Silvia M, Fabio B, Massimo C, 1D simulation and experimental analysis of a turbocharger turbine for automotive engines under steady and unsteady flow conditions, Energy Procedia Vol.45, PP.909-918, 2014.
- [92] Abidat M, Hachemi M, and Baines N, Prediction of the steady and non- steady flow performance of a highly loaded mixed flow turbine, Proceedings of IMechE Part A, Journal of Power and Energy, Vol.212, PP.173-184, 1998.
- [93] Peter L and Arthur J, Computer Code for Off-Design Performance Analysis of Radial-

- Inflow Turbines with Rotor Blade Sweep, NASA Technical Paper 2199, 1983.
- [94] Spence S and Artt D, An experimental assessment of incidence losses in a radial inflow turbine rotor, Proceedings of IMechE Part A, Journal of Power and Energy, Vol.212, PP.43-53, 1998.
- [95] Serrano J, Arnau R, Dolz V, Tiseira A, Cervello C, A model of turbocharger radial turbines appropriate to be used in zero- and one-dimensional gas dynamics codes for internal combustion engines modelling, Energy Conversion and Management, Vol.49, PP.3729-3745, 2008.
- [96] Tancrez M, Galindo J, Guardiola B, Fajardo P, Varnier O, Turbine adapted maps for turbocharger engine matching, Experimental Thermal and Fluid Science, Vol.35, PP.146-153, 2011.
- [97] Chen H, Hakeem I and Martinez R, Modelling of a Turbocharger Turbine under Pulsating inlet conditions, Proceedings of IMechE Part A, Journal of Power and Energy, Vol.210, PP.397-408, 1996.
- [98] Fredrik H and Laszlo F, Effects Of Inlet Conditions On The Turbine Performance Of A Radial Turbine, Proceedings of ASME, GT2008- 51088, 2008.
- [99] Macek J, Vávra R and Vítek O, 1-D Model of Radial Turbocharger Turbine Calibrated by Experiments, SAE Paper 2002-01-0377, 2002
- [100] Kessel J, Schaffnit J, Schmidt M, Modelling and real-time simulation of a turbocharger with variable turbine geometry (VTG). SAE Paper 980770; 1998.
- [101] Aungier R, 1988, "A Performance Analysis for the Vaneless Components of Centrifugal Compressors," Flows in Non-Rotating Turbomachinery Components, ASME, Vol. 69, 35-43.
- [102] Aungier R, 1990, "Aerodynamic Performance Analysis of Vaned Diffusers," Fluid Machinery Components, ASME, Vol. 101, 27-44.
- [103] Aungier R, 1993, "Mean Streamline Aerodynamic Performance Analysis of Centrifugal Compressors," Proceedings Rotating Machinery Conference and Exposition (ROCON'93), Vol. I. (Also in Transactions ASME, Journal of Turbomachinery, July 1995, 360-366.)
- [104] Aungier R, 2000, Centrifugal Compressors a Strategy for Aerodynamic Design and Analysis, ASME Press, New York.
- [105] Baines N, 2005, Fundamentals of Turbocharging, Concepts NREC, Vermont.

- [106] Boyce M, 2003, Centrifugal Compressors a Basic Guide, PennWell Corporation, Oklahoma.
- [107] Heywood J, 1988, Internal Combustion Engine Fundamentals, McGraw-Hill, Inc. New York.
- [108] Japikse D, 1996, Centrifugal Compressor Design and Performance, Concepts ETI, Inc., Vermont.
- [109] Lieblein S, (1959). "Loss and Stall Analysis of Compressor Cascades," ASME Transactions, Journal of Basic Engineering, Sept., 387-400.
- [110] Nunn R, 1989, Intermediate Fluid Mechanics, Hemisphere Publishing Corporation, New York.
- [111] Reneau L, Johnston J, and Kline S, 1967, "Performance and Design of Straight Two-Dimensional Diffusers," Transactions ASME, Journal of Basic Engineering, Mar., 141-150.
- [112] Sengupta J, Erickson C, Chapman, K.S., and Kesavarz, A. (2007). "Turbocharger Component Matching System Development" Proceedings of the Internal Combustion Engine Division Fall Technical Conference Paper No. ICEF2007-1767, South Carolina.
- [113] Weber C, and Koronowski M, 1986, "Meanline Performance Predictions of Volute in Centrifugal Compressors," Paper No. 86-GT-216, ASME, New York.
- [114] Civinkas K, Povinelli L, Application of a Quasi-3D Inviscid Flow and Boundary Layer Analysis to the Hub Shroud Contouring of a Radial Turbine, AIAA/SAE/ASME Joint Propulsion Conference, 1984
- [115] McLallin K, Haas J. – Experimental Performance and Analysis of 15.04 Tip Diameter Radial Inflow Turbine with Work Factor of 1.126 and Thick Blading, NASA Tech., 1980
- [116] Rodgers C, Mainline performance prediction for radial inflow turbines, Lecture Series 1987-07, Von Karman Institute for Fluid Dynamics, 1987
- [117] Rohlik H, Radial inflow turbines, Turbine design and applications, NASA SP 290 vol. 3, 1975.
- [118] Yeo J, Baines N, Pulsating flow behavior in a twin-entry vaneless radial inflow turbine, Turbocharging and Turbochargers, IME, 1990
- [119] Benson R, A review of methods for assessing loss coefficients in radial gas turbines,

Internal Journal of Mechanical Science, 1970, 18: 905-932

[120] Rodgers C, Geiser R, Performance of a high efficiency radial/axial turbine, ASME Journal of Turbomachinery, 1987, 109: 151-154

[121] Jansen W, The design and performance analysis of radial inflow turbines, NREC Report 1067, 1964

[122] Hiatt G, Johnston I, Experiments concerning the aerodynamic performance in inward radial flow turbines, Proceeding of the Institution of Mechanical Engineers, 1963, 178: 28-42

[123] Nemdili A, Hellmann D, Development of an empirical equation to predict the disc friction losses of a centrifugal pump, Proceedings of the 6th International Conference on Hydraulic Machinery and Hydrodynamics, Timisoara, RU, 2004

[124] Spraker W, Contour clearance losses in radial inflow turbines for turbochargers, ASME paper No 87-ICE-52, 1987

[125] Futral S, Wasserbauer C, Off-design performance prediction with experimental verification for a radial-inflow turbine, NASA TN D-2621, 1965

[126] Lazzaretto A, Manente G, A criterion to optimize ORC design performance taking into account real turbine efficiencies, Proceedings of ECOS, Guilin; RC, 2013

[127] Moustapha H, Zelesky M, Baines N, Japikse D, Axial and Radial Turbines, Concepts NREC, 2003

[128] Whitfield A, Baines N, Design of radial turbomachines, Longman Scientific and Technical, New York, USA, 1990 Dixon S.L., Hall C.A., Fluid mechanics and thermodynamics of turbomachinery, Butterworth Heinemann, sixth edition, 2010

[129] Chen H, Baines N, The aerodynamic loading of radial and mixed flow turbines, International Journal of Mechanic Science, 1994, 36: 63-79

[130] Pešić R, Experimental Determination of Double Vibe Function Thermal Science: Year 2010, Vol. 14, Suppl., pp. S197-S208

[131] AVL Boost User Guide. 03/2001 Edition. Document Number 01.0104.2010.1 AVL List